Experimental study and numerical simulation of defect formation during compression moulding of discontinuous long fibre carbon/PEEK composites

Benoit Landry

Department of Mechanical Engineering

McGill University

A thesis submitted to McGill University

in partial fulfillment of the requirements for the degree of

Doctor of Philosophy

Abstract

Composite materials continue to replace metal in a growing number of applications due to their recognized performance, tailorability, life-cycle, and manufacturing advantages. While continuous fibre composites are the primary materials employed to replace metallic components in aerospace applications, their current use is generally limited to large shell-like structures. There is thus an emerging interest in the aerospace industry to use composite materials at a smaller scale to replace complex-shaped metallic components. This presents some unique challenges, mainly because traditional continuous fibre composite materials are practically unusable for this type of application, while short-fibre injection moulded parts have limited mechanical properties, although being highly versatile geometrically. Lying between these two extremes are discontinuous long fibre (DLF) composites, a bulk moulding compound type of material that can be compression moulded into complex-shaped parts. This technique has been shown to be very effective for moulding net-shaped components having features such as varying wall thickness, tight radii, reinforcing ribs, flanges, mould-in holes, etc. However, the increase in part complexity introduces manufacturing problems. One problem in particular arises during processing of thermoplastic composites, where inconsistent part quality may occur if the consolidation pressure is lost before solidification of the matrix during cooling. Such a phenomenon can be difficult to predict due to the complex nature of DLF composite parts. Given that understanding and predicting defect formation is crucial to achieving success in manufacturing of complex-shaped composite parts, a threefold approach was used in this thesis to study the phenomena that influence this behaviour.

First, crystallization kinetics, thermal and crystallization shrinkage, and modulus development of carbon/Polyetheretherketone (PEEK) composites were characterized during cooling down from the melt temperature using thermal analyses. The results showed very rapid changes in thermomechanical properties during crystallization. The mechanisms responsible for the loss of pressure during cooling and subsequent defect formation were identified.

Second, an experimental investigation of the moulding defects formed during cooling of DLF composite was conducted. Loss of contact between the material and the tooling surfaces due to thermal shrinkage was observed experimentally. Moulding defects were reproduced on simple flat panels using an instrumented test fixture and the critical temperature range of defect formation was identified. The effect on mechanical properties was quantified by comparing the strength of specimens having different levels of moulding induced defects. The sensitivity to void content observed was much higher than what is commonly reported for continuous fibre composites. The importance of a proper cooling strategy was demonstrated by successfully moulding a defect-free L-bracket with a rib feature.

Finally, a finite element model was developed to predict defect formation during compression moulding of DLF carbon/PEEK composites. Analytical equations based on the thermal characterization results were developed to evaluate thermomechanical properties as a function of temperature, cooling rate, and degree of crystallinity. The process model showed that the maximum temperature at which the pressure is lost during cooling is very sensitive to the temperature variation of the part and the applied moulding pressure. It was also demonstrated that the order in which components are cooled is key to ensure a good consolidation of complex-shaped features.

Material characterization and processes modelling developed from simple experiments allowed for successful understanding of the nature of the mechanisms responsible for defect formation during moulding of DLF composites. The approach presented in this work could be used to identify problematic regions of a part before manufacturing, considerably reducing the trial and error often required to successfully manufacture defect-free DLF composite parts.

Sommaire

Les matériaux composites sont utilisés pour remplacer des pièces métalliques dans un nombre grandissant d'applications. La popularité de ceux-ci est principalement due à leur haute performance, leur excellente adaptabilité et leurs avantages au niveau de la fabrication. Bien que les composites à fibres continues sont les matériaux principalement utilisés pour la conception de pièces à haute performance en aérospatiale, leur utilisation actuelle est généralement limitée à de grandes structures à paroi mince. Il y a donc un intérêt émergeant dans l'industrie aérospatiale pour faire l'usage des matériaux composites à plus petite échelle, afin de remplacer des pièces métalliques complexes. Cela présente des défis uniques, car les composites à fibres continues traditionnels sont pratiquement inutilisables pour ce type d'application. D'autre part, les pièces fabriquées par injection de plastique avec fibres courtes ont des propriétés mécaniques inférieures, bien qu'étant très polyvalentes géométriquement. Entre ces deux extrêmes, les composites à fibres longues discontinues (FLD) offrent la possibilité de fabriquer des pièces à géométrie complexe par l'entremise du moulage par compression. Cette technique s'est avérée très efficace pour le moulage de pièces à finition immédiate ayant des caractéristiques telles que des variations d'épaisseur, des rayons serrés, des nervures de renfort, etc. Cependant, l'augmentation de la complexité des pièces peut introduite des problèmes de fabrication. Un problème en particulier se pose lors de la fabrication des composites thermoplastiques, où une variation de la qualité des pièces peut survenir si la pression de consolidation est perdue avant la solidification de la matrice durant le refroidissement. Ce phénomène peut être difficile à prédire en raison de la nature complexe des pièces composites FLD. Étant donné que la

compréhension et la prédiction de la formation de défauts sont cruciales dans la fabrication de pièces composites à géométrie complexe, une approche en trois volets a été utilisée dans cette thèse pour étudier les phénomènes qui influencent ce comportement.

Tout d'abord, la cinétique de cristallisation, le retrait thermique et de cristallisation, ainsi que le développement du module d'élasticité du composite carbone/polyétheréthercétone (PEEK) ont été caractérisés au cours du refroidissement à partir de la température de fusion en utilisant des analyses thermiques. Les résultats ont démontré des changements très rapides dans les propriétés thermomécaniques au cours de la cristallisation. Les mécanismes responsables de la perte de pression durant le refroidissement et la formation subséquente de défauts ont été identifiés.

Ensuite, une étude expérimentale sur les défauts de moulage formés au cours du refroidissement des composites FLD a été effectuée. La perte de contact entre les surfaces du moule et le matériel causée par le retrait thermique a été observée expérimentalement. Les défauts de moulage ont été reproduits sur des panneaux plats à l'aide d'un montage instrumenté. La plage de température critique de la formation de défauts a été identifiée. L'effet sur les propriétés mécaniques a été quantifié en comparant la résistance d'échantillons ayant différents niveaux de défauts de moulage. La sensibilité à la porosité observée était beaucoup plus élevée que celle communément rapportée pour les composites à fibres continues. L'importance d'une stratégie de refroidissement adéquate a été démontrée en fabriquant avec succès une pièce en L avec une fonction de nervure sans défauts.

Finalement, un modèle d'éléments finis a été développé pour prédire la formation de défauts pendant le moulage par compression des composites FLD. Des équations analytiques basées sur les résultats de caractérisations thermiques

ont été développées afin d'évaluer les propriétés thermomécaniques du matériau en fonction de la température, de la vitesse de refroidissement, et du degré de cristallinité. Le modèle a démontré que la température maximale à laquelle la pression est perdue au cours du refroidissement est très sensible à la variation de température dans la pièce ainsi qu'à la pression de moulage appliquée. Il a également été démontré que l'ordre dans lequel les composants sont refroidis est très important afin d'assurer une bonne consolidation sur les caractéristiques de la pièce ayant des formes complexes.

La caractérisation des matériaux et la modélisation des processus développées à partir d'expériences simples à petite échelle ont permis de comprendre avec succès la nature des mécanismes responsables de la formation de défauts lors du moulage de composites FLD. L'approche présentée dans ce travail pourrait être utilisée pour identifier les régions problématiques d'une pièce avant de la fabrication, réduisant considérablement les essais et erreurs souvent nécessaires au succès de la fabrication de pièces composites FLD sans défaut.

Acknowledgements

First, I would like to thank my supervisor, Prof. Pascal Hubert, for all of his support and guidance that he has given me over the past four years.

This work was carried out as part of a Consortium de recherche et d'innovation en aérospatiale au Québec (CRIAQ) academic–industry collaborative research project (COMP–412). Industry partners and research centre partners, Bell Helicopter Textron Canada, Bombardier Aerospace, Pratt and Whitney Canada, Hutchinson Aerospace & Industry, Delastek, Avior Integrated Products, the National Research Council Canada – Automotive and Surface Transportation, and the National Research Council Canada – Institute for Aerospace Research provided financial support and access to equipment. Financial assistance from the Natural Sciences and Engineering Research Council of Canada (NSERC) and McGill University was also greatly appreciated.

I would like to thank Dominic LeBlanc, Arthur Levy, Gilles-Philippe Picher-Martel, and Marina Selezneva for years of collaboration on the COMP–412 project. Many thanks go to Marc Palardy-Sim for his generous help with the Micro-CT scans. Cheers to the present and past members of the Structures and Composite Material Laboratory. This is a wonderful research group.

Last but not least, I would like to thank my friends and family for all their support through my graduate studies.

Table of Content

List of Figures

List of Tables

Chapter 1

Introduction

In recent years, the fast growing development of composite materials has resulted in significant progress in the replacement of metallic components in modern aircraft. The Boeing 787 is a great example, comprising nearly half carbon fibre reinforced plastic and other composites, resulting in a lower overall airplane weight, reduced fuel consumption, reduced scheduled maintenance, and improved service life [1]. The material of choice for those metallic replacements is high fibre volume fraction continuous fibre reinforced composite prepreg, offering high-performance, and well developed processing methods for manufacturing large primary aircraft structures [2].

The current use of continuous fibre composite material for aerospace applications is generally limited to shell-like structures with minimal curvature and thickness variations, such as the fuselage, wings, and tail sections. This implies that a high number of load bearing components in current aircraft structures still remain metallic. Complex-shape metallic components are generally machined from aluminum, steel or titanium — a time costly operation from which a lot of waste can be generated. Complex machined parts can have a "buy-to-fly" ratio as high as 20:1, i.e. 20 times the volume of the final part must be purchased as raw material [3]. This shows that to further increase the performance of new aircraft, there is a need to replace geometrically complex metallic parts

such as brackets, clips, or other components with composite equivalents. This can be very challenging, mainly because traditional continuous fibre composite materials are practically unusable for this type of application. On the other hand, short-fibre injection moulded parts are highly versatile geometrically, but have limited mechanical properties. There is thus an interest to develop material systems capable of bridging the gap between injection moulded parts (high complexity – limited performance) and continuous fibre unidirectional tape or fabric composites (high performance – limited complexity), as shown schematically in Fig. 1.1. A literature survey revealed the existence of a type of material system potentially capable of bridging this gap: discontinuous long fibre composites.

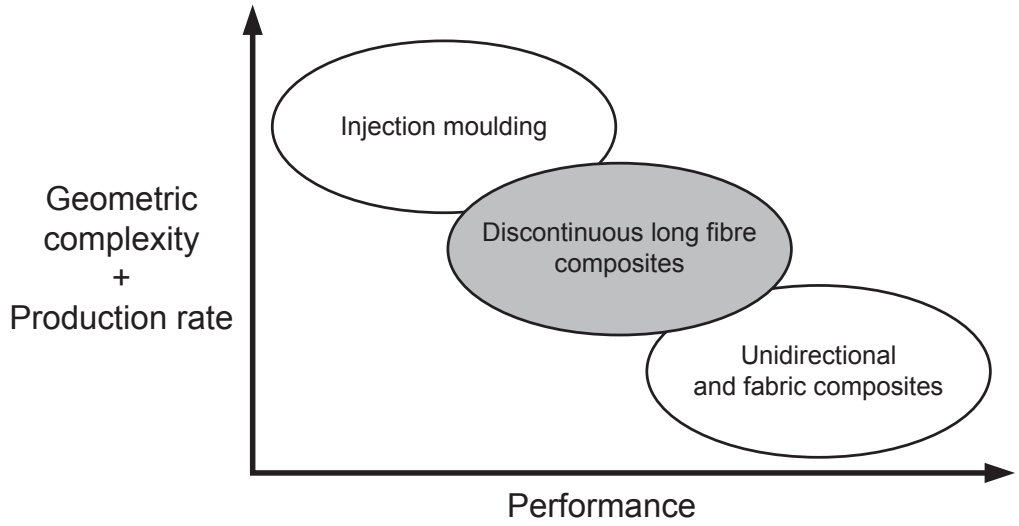

Figure 1.1 – Metal replacement chart. Adapted from [3].

1.1 Discontinuous fibre composites

Although the interest in discontinuous fibre reinforced plastics dates back to the 1960s [4,5], their application in aerospace structures has been very limited, mainly due to their low mechanical properties. In recent years, the fast growing development of composites has resulted in major improvement in raw material mechanical properties and manufacturing techniques. Several types of discontinuous fibre materials have thus been developed and studied. Those material systems range from aligned discontinuous fibres or strips, to randomly distributed discontinuous fibres or strips. Of those material systems, compression moulding of Discontinuous Long Fibre (DLF) composites is new processing technique that has seen a growing interest since its introduction in the late 2000s. Discontinuous long fibre composites consist of unidirectional pre-impregnated thermoset or thermoplastic tape chopped into small strands (or chips) of predefined dimensions (Fig. 1.2). The material is used in bulk form or as a mat (similar to sheet moulding compound) and compression moulded into net-shaped components. From a manufacturing standpoint, DLF composites are less labour intensive than continuous fibre tapes, since cutting and preforming is not required. This process is a very attractive candidate for the replacement of metallic parts, as it offers the possibility to produce net-shaped components having features such as varying wall thickness, tight radii, reinforcing ribs, flanges, mould-in holes, etc. In addition, secondary metallic components such as threaded bushings, inserts, and nutplates can be incorporated during the molding process. By producing net or near-net shape parts, material waste is considerably reduced, while the need for traditional post-moulding operations such as cutting, trimming and/or drilling is practically eliminated.

Carbon-based DLF material systems can have fibre volume fractions over 60%, i.e. roughly twice that of traditional short-fibre composites. They exhibit

Figure 1.2 – Chopped thermoplastic tape (bulk form).

highly desirable mechanical behaviour, such as in-plane isotropy, and stiffness comparable to that of continuous fibre quasi-isotropic laminates [6]. Moreover, typical densities of DLF composites materials are ∼43–80% lower than metals such as titanium, aluminum, and steel. Practical real world weight savings for metal replacement parts were shown to range between 30–35% vs. aluminum and 40–50% vs. titanium or steel [3]. Overall, DLF composites were proven to be a very good candidate to bridge the metal replacement gap, as shown in Fig. 1.1. This breakthrough in composite manufacturing technology has thus motivated the development of processing techniques for moulding of defect-free, complex, and net-shaped composite parts.

The excellent formability of compression moulded DLF composites has been demonstrated by Greene, Tweed & Co. [3], TenCate [7], Feraboli *et al.* [8], LeBlanc *et al.* [9], and Cross Composite AG [10]. Two examples of metallic parts converted to net-shape DLF composite components are shown in Fig. 1.3. First, a three-piece aluminum component assembled with fasteners was replaced with a one-piece carbon/PEEK DLF composite part, Fig. 1.3a. The substitution to a single component eliminated the costs associated with secondary assembly operations, as well as multiple inspections, work orders, and drawings that were required for the original metal assembly. The DLF part demonstrated a 43%

weight savings vs. the original aluminum assembly. Second, the aluminum front lower control arm in Fig. 1.3b was converted to a net-shape carbon/vinyl ester DLF composite part. A 27% weight reduction was obtained, as well as a cost and cycle time reduction with respect to the forged aluminum construction [8].

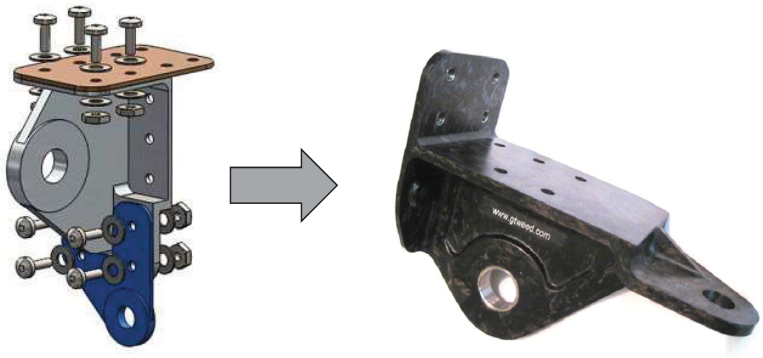

(a)

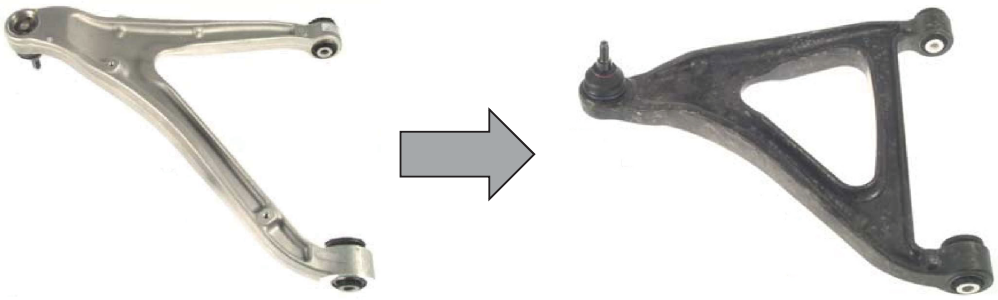

(b)

Figure 1.3 – Examples of metallic parts converted to net-shape DLF composite components. (a) Conversion of a multi-piece metallic component to a single-piece carbon/PEEK DLF composite part produced by Green, Tweed & Co. [3]. (b) An aluminum front lower control arm of the Lamborghini *Sesto Elemento* converted to a carbon/vinylester DLF composite component [8].

1.2 Processing of thermoplastic DLF composites

While several manufacturing methods have been developed to produce complex-shape composites parts, compression moulding (i.e. matched-die moulding) used in conjunction with DLF composite materials is the most appealing process, as it offers short cycle time, high-volume production, complex-shape moulding capabilities, and is one of the few methods capable of achieving the high pressures required by the process. The compression moulding process of thermoplastic DLF composites includes the following steps:

1. The required weight of material is measured and put in the mould cavity.
2. The mould assembly is brought to the processing temperature under low pressure, melting the thermoplastic matrix.
3. High pressure is applied to induce flow of the material and fill the mould cavity. The material is then consolidated under the same pressure, removing entrapped air and/or voids.
4. The mould assembly is cooled under high pressure until the matrix has solidified. The part is subsequently ejected from the mould.

Similarly to injection moulding of short-fibre reinforced composites, compression moulding of DLF thermoplastic composites is carried out at high pressure [7,9–11]. This favours the filling of the mould cavity at the melt temperature, and also helps compensate the thermal and crystallization shrinkage (for a semi-crystalline matrix) of the material during cooling. The latter is important in order to prevent localized loss of contact between the material and the mould, which could compromise the compaction quality of the material and lead to defect formation. This phenomenon, shown schematically in Fig. 1.4, can occur due to non-uniform shrinkage caused by an in-plane temperature variation, or in a complex feature where compaction is applied indirectly, such as a T-shaped

part [9,11]. Furthermore, the high out-of-plane modulus of DLF composites owing to its high fibre volume fraction substantially reduces the ability to compensate for shrinkage, making it challenging to manufacture defect-free complex shaped parts.

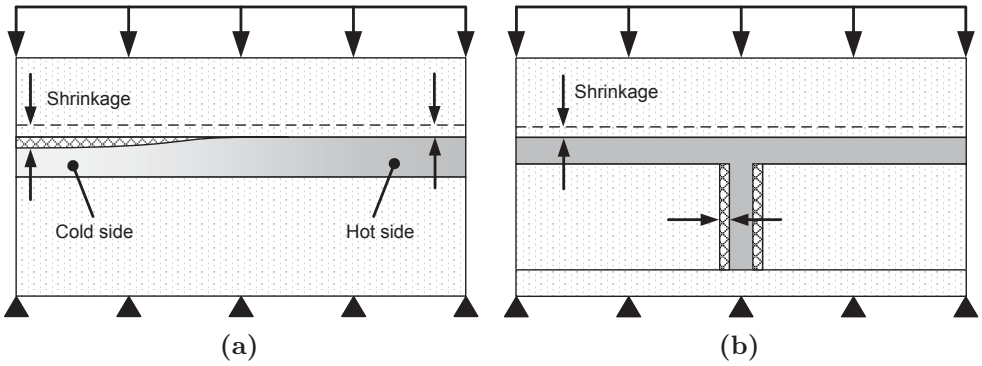

Figure 1.4 – Schematic of two circumstances where the loss of contact (shown in cross-hatched regions) between the material and the mould can occur during cooling of a compression moulded DLF composite part. (a) Non-uniform shrinkage due to an in-plane temperature variation. (b) Indirect compaction in a complex feature.

1.3 Research objectives

While the literature addresses the general behaviour, mechanical properties, failure characteristics, and feasibility of moulding complex shaped DLF composites, the processing aspects of these materials for both thermoset and thermoplastic-based material systems have not received much attention. This is important since the uniqueness and complexity of DLF composite parts can make it very challenging to predict defect formation during processing. As a result, most tooling designs are developed at a great expense by trial and error, because no process models exist for DLF composites part manufacturing.

The main goal of this thesis is to identify the leading causes of defect formation during processing and demonstrate how process modelling can be used to tailor the moulding process in order to optimize the manufacturing of discontinuous long fibre thermoplastic composites. The specific research objectives are as follows:

1. Characterize the influence of crystallization on the development of the mechanical properties of carbon/PEEK tape,
2. Determine the fundamental causes of defect formation during processing of DLF composites,
3. Identify the type of process-induced defects caused by localized loss of pressure during cooling and quantify their effect on mechanical performance,
4. Develop a process model to predict part pressure distribution and defect formation during cooling of DLF composites,
5. Propose practical guidelines to minimize the risk of defect formation during fabrication of complex-shaped DLF composite parts.

1.3.1 Thesis outline

The work presented in this thesis is organized as shown in Fig 1.5 as follows:

- Chapter 2 reviews the current state of knowledge on the topic of DLF composites.
- Chapter 3 presents the materials, experimental setups and procedures for moulding of continuous fibre and DLF composites parts.
- Chapter 4 presents the thermal characterization of carbon/PEEK tape. Crystallization kinetics, shrinkage and modulus development during cooling from melt are measured.

- Chapter 5 presents an investigation of the moulding defects formed during cooling of DLF carbon/PEEK composites. An experimental setup is employed to reproduce the moulding defects and identify the temperature range during cooling at which they are formed. The effect on mechanical properties is quantified by comparing the compressive and flexural strength of specimens having different levels of moulding induced defects.
- Chapter 6 presents two case studies. First, the processing conditions required to obtain a void-free complex-shaped DLF part are investigated. Second, the influence of moulding defects on the impact properties of DLF composites is studied.
- Chapter 7 presents the model development for part pressure distribution during cooling, which can identify regions susceptible of having moulding defects. The properties measured in Chapter 4 are linked together to form a thermomechanical model suitable for DLF composites. The model was validated on simple flat DLF composite panels moulded at different moulding pressures. The model is then employed in two parametric studies, where the influence of the process parameters are investigated.
- Chapter 8 draws conclusions from this work, identifies the original contributions, and discusses the future outlook for research on DLF composites.

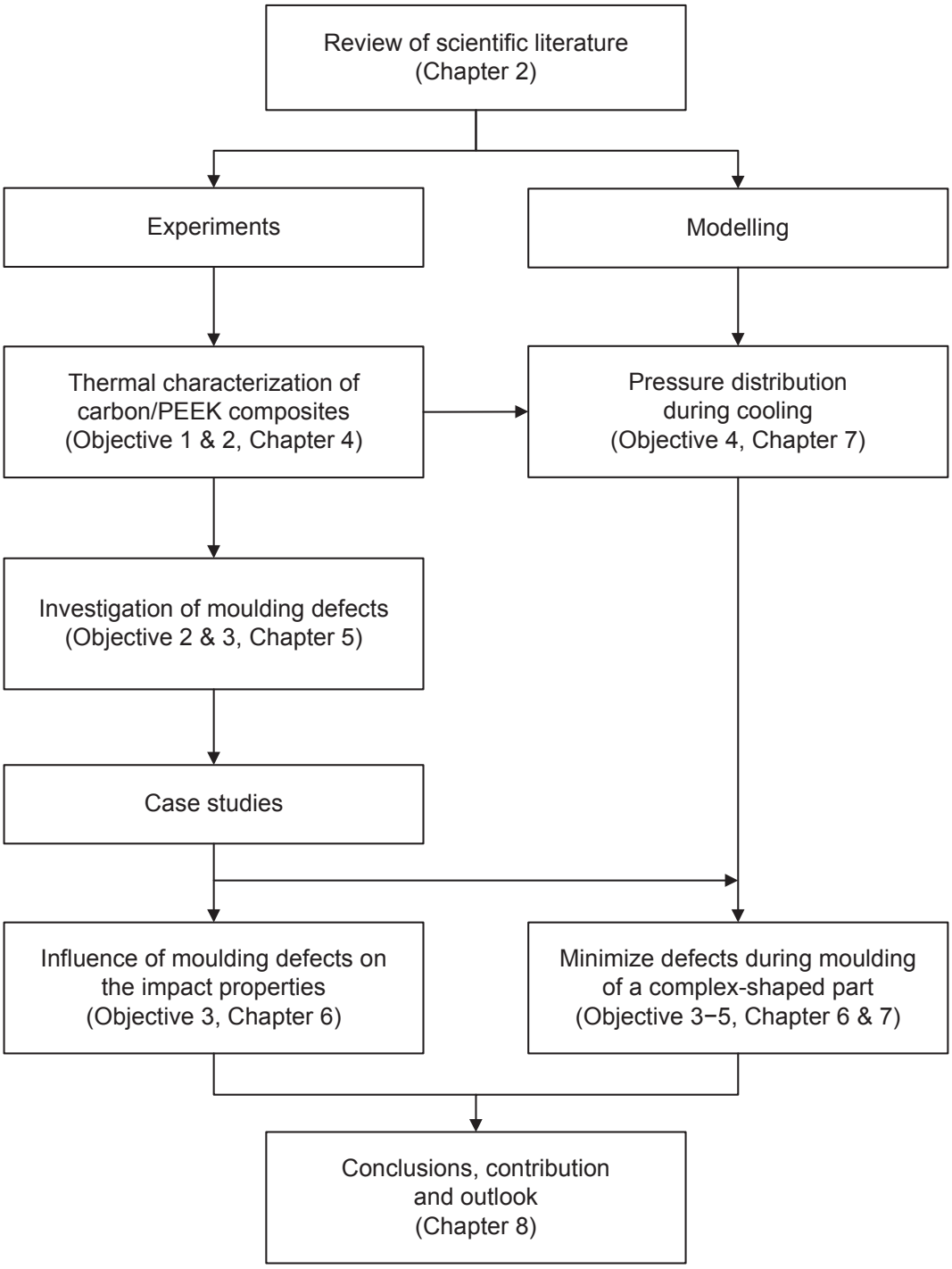

Figure 1.5 – Flowchart of thesis organization with objectives.

Chapter 2

Review of Scientific Literature

Although an extensive literature body of literature exists on the general topic of discontinuous fibre composites, a very limited number of studies touch the topic of processing, material behaviour, and mechanical properties of discontinuous long fibre (DLF) composites. Therefore, the main objective of this chapter is to review the pertinent scientific literature on the topic of high fibre volume fraction ($V_f \geq 40\%$) thermoset or thermoplastic discontinuous fibre composites that are compression moulded from randomly-oriented strands of tape.

This chapter first presents an overview of the different thermoset and thermoplastic DLF material systems that have been proposed in the literature. Processing, flow behaviour, moulding capabilities, and mechanical behaviour of those materials will be discussed. The second part of this chapter reviews two topics that are relevant with the objectives of this thesis: the effect of porosity on the mechanical properties of composites, and experimental studies of thermomechanical properties of carbon/PEEK (PolyEtherEtherKetone) composites.

2.1 Thermoplastic vs. thermoset matrices

Aerospace grade composite materials can be grouped in two main categories: thermoplastic and thermoset resin systems. Thermoset resin systems are typically cured between 80 °C and 177 °C. During processing, the resin undergoes cross-linking — the formation of irreversible chemical bonds [2]. Thermoset resins do not melt; they decompose and do not reform upon cooling. On the other hand, the polymer chains in thermoplastic resins systems associate through intermolecular forces, which weaken rapidly with increased temperature. This permits the flow and forming of the material during processing. Thermoplastic materials can thus be re-melted and re-processed several times. This is very advantageous from a manufacturing standpoint, since it opens the possibility to welding [12], overmoulding [13], and recycling [14]. Other advantages of thermoplastics over thermosets include unlimited shelf life of raw materials, enhanced fracture toughness, superior impact resistance, and enhanced environmental, moisture, and corrosion resistance [15]. Moulding cycles as short as a few seconds can also be achieved with thermoplastics. A comparison between high-performance thermoplastic and thermoset matrices with regards to the processing of DLF composites are shown in Table 2.1.

2.2 Overview of discontinuous fibre material systems

The different types of DLF composite preforms can be categorized based on the form of their reinforcement (individual fibres vs. strips) and their orientation (aligned vs. random), as shown in Fig. 2.1. Aligned long discontinuous fibre preforms (Fig. 2.1a) are similar to unidirectional prepreg plies, and can be layered to form a laminate. Chang and Pratte [17] and Sun *et al.* [18] studied tensile, compressive, flexural, shear and thermal properties of autoclave-processed

Table 2.1 – Comparison between high-performance thermoplastic and thermoset matrices with regards to the compression moulding of DLF composites.

	Thermoplastic [7]	Thermoset [16]
Typical materials	PPS[a], PEKK[b], PEEK[c]	Vinyl ester
Shelf life	∞	2 months
Processing temperature (°C)	330 – 400	127 – 177
Typical cycle time (min)	12 – 48[d]	5 – 10
Recyclable	Yes	No

[a]Polyphenylene sulfide, [b]Polyetherketoneketone, [c]Polyetheretherketone

[d]Based on recommended dwelling time, cooling rate, and demoulding temperature.

carbon/PEKK panels and showed that aligned DLF composites can achieve performance close to that of continuous fibre materials. Schuster and Friedrich [19, 20] evaluated the tensile and fatigue properties of unidirectional and cross-ply thermoformed aligned DLF composites and showed that the static properties were comparable to continuous fibre laminates, while the fatigue life was shorter.

Similar mechanical behaviour was observed with carbon/epoxy Directed Carbon Fibre Preform (DCFP) composites [21–23]. The material consist of long (3–115 mm) randomly-oriented fibre bundles with a fibre volume fraction of around 30%, as depicted in Fig. 2.1b. Results showed that elastic properties of composites reinforced by fibre bundles are comparable to those of quasi-isotropic (QI) continuous fibre laminates. However, strength is lower and was shown to be strongly affected by the size of the fibre bundles and the homogeneity of the coverage. Shorter and smaller bundles had better tensile properties than longer fibre bundles, mainly because they achieved better coverage and were less likely to curl.

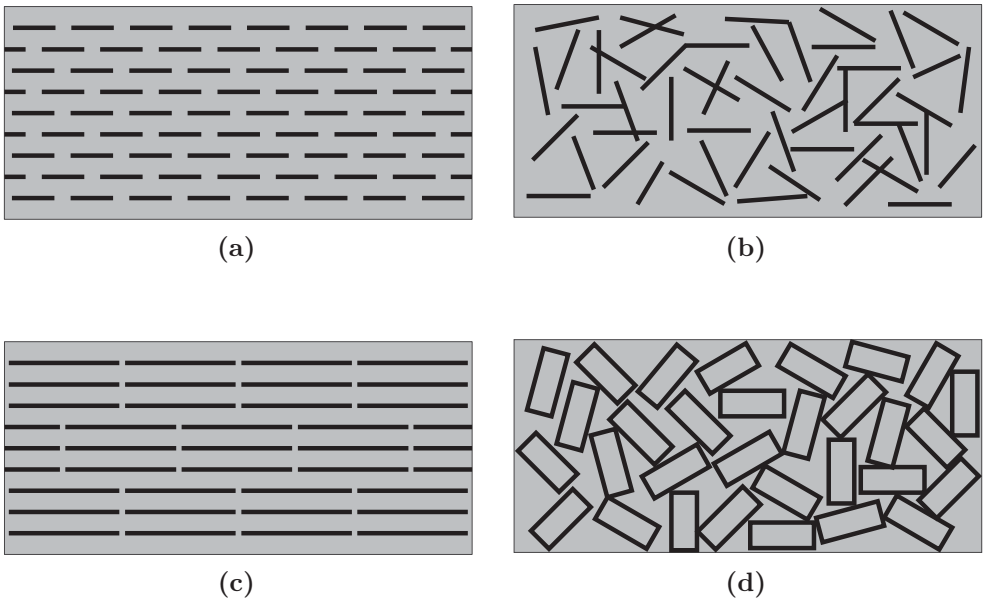

Figure 2.1 – Different types of DLF material preforms: a) aligned fibres, b) randomly oriented fibres or fibre bundles, c) aligned strips, and d) randomly-oriented strips of unidirectional tape.

Taketa *et al.* [24–27] introduced the concept of Unidirectionally Arrayed Chopped Strands (UACS), shown in Fig. 2.1c. They are prepared by introducing slits into a carbon/epoxy prepreg using an automated cutting machine. This procedure results in a sheet-like molding material constructed with regularly and unidirectionally arrayed discontinuous fibre strands. In contrast with sheet moulding compound (SMC), the interlayer slip in UACS prevents direct contact between the chopped strands, which allows parts to be moulded at high fibre volume faction (60%+ compared to 40% for SMC). The effect of different slit parameters (e.g. width, frequency, and angle) on the mechanical properties of UACS was evaluated [24,26]. The material was shown to exhibit a modulus comparable to that of continuous fibre QI laminates, while strength was significantly lower. Flowability of UACS composites was demonstrated by compression molding a 15 mm deep rib structure [27].

More recently, Feraboli *et al.* [6,28–31] proposed a prepreg-based discontinuous material system that sits between traditional SMC and prepreg, Fig. 2.1d. Unidirectional carbon/epoxy prepreg are slit and chopped into chips of predefined dimensions. The chips are then scattered and shuffled in a mould cavity and press moulded into the desired geometry. The chip dimensions varied from 13 mm to 76 mm in length and 4 mm to 9 mm in width. This type of material has already found commercial applications and is available from manufacturers such as Hexcel (carbon/epoxy HexMC™), Quantum Composite (carbon/vinylester, AMC® 8593), and TenCate (carbon/PEEK Cetex® MC1200 BMC). Similarly to UACS composites, interlayer slip between individual chips of prepreg permits the use of high fibre volume fraction prepreg (∼60%). It was shown that the strength of composites moulded from prepreg chips is significantly lower than that of QI continuous fibre composites, while stiffness is comparable [6].

The general consensus is that unlike stiffness, the strength of discontinuous fibre composites cannot attain the strength of continuous fibre composites. Harper *et al.* [21] have attributed this behaviour to stress concentrations introduced at the fibre ends. This implies that the fibre length at which a plateau in strength occurs may be up to 5–10 times longer than the corresponding critical length for stiffness.

2.3 Discontinuous long fibre composites

This sections reviews experimental investigations performed specifically on composites compression moulded from randomly-oriented strands (or chips) of prepreg tape. For the remainder of the thesis work, this material will be referred to as “DLF composites”.

2.3.1 Processing, flow behaviour, and moulding capabilities

Carbon/vinyl ester DLF composites were employed to manufacture the front and rear control arms of the Lamborghini *Sesto Elemento* — a composite technology demonstrator vehicle [8]. The parts were moulded with selective localized unidirectional reinforcements, which were placed within the DLF charge. It was shown that this technique not only improve strength, but also reduced its variability. By employed a low-flow moulding strategy, i.e. ensuring an initial mould coverage area of over 90%, fibre alignment due to material flow was reduced, leading to less variability in the mechanical properties of the moulded parts. With a total cycle time from raw material to complete part (with bushings and ball joint) under one hour, the final part cost was shown to be highly competitive with the forged aluminum construction. A similar type of material, Hexcel HexMC$^{\text{TM}}$, was employed to manufacture the window frames of the Boeing 787, offering a weight saving of almost 50% and superior damage tolerance when compared to a traditional aluminium frame [32].

Tuttle *et al.* [33] studied the effect of high-flow moulding on tensile properties of panels manufactured from Hexcel HexMC$^{\text{TM}}$ DLF composites. Although material flow had no impact on the local fibre volume fraction, a substantial amount of fibre alignment was observed near the mould edges. This lead to an increase in the modulus of the specimen taken near the mould boundaries. An adverse effect was observed for the ultimate tensile stress and strain; both properties were lower near the mould edges.

The formability of compression moulded thermoplastic DLF composites has been demonstrated in several studies. van Wijngaarden *et al.* [34] compression moulded a deep flange out of carbon/PEEK DLF composites at processing pressures ranging from 30 bar to 120 bar. It was observed that the flow of

the material at the processing temperature is greatly influenced by the applied pressure. Moulding defects were observed in all processing trials. LeBlanc [9,11] investigated the influence of the processing pressure and strand geometry on the filling of a 25 mm deep rib cavity moulded from carbon/PEEK DLF composites. The filling pressure was found to increase with the strand size of the DLF composite (restricted flow) and decrease at higher processing temperature (lower viscosity). Surface defects were observed on the rib section processed at the filling pressure (10 bar to 30 bar). Void content analysis conducted using X-ray microtomography (micro-CT) showed porosity of up to 1.2% in the rib section. A feasibility study on the manufacturing of a carbon/PEEK rotorcraft door hinge featuring net-shaped holes was presented by Eguémann *et al.* [10]. Bearing tests showed that the door hinge moulded from 10–20 mm long strands exhibited similar strength to that of a CNC-machined steel counterpart, with a weight reduction of 84%.

In his work, Picher-Martel [35,36] investigated of the flow and deformation mechanisms of carbon/PEEK DLF composites using micro-CT. A novel technique using marker strands coated with conductive silver paint was developed to track the evolution of the material during squeeze flow. A 2–D finite element model to predict the squeeze flow behaviour of the material was implemented using an Eulerian-Lagrangian approach. The model was validated with experimental data and provides guidelines to predict the pressure required to fill a part feature for a given strand size.

2.3.2 Material behaviour and mechanical properties

2.3.2.1 Thermoset-based DLF composites

Feraboli *al.* [6,28–31] conducted an extensive study on the tensile, compressive and flexural properties of carbon/epoxy laminates produced by compression molding of chopped unidirectional prepreg. Flat plates were molded using manually prepared prepreg charges. It was shown that the material exhibits in-plane isotropic behaviour [6]. In general, the ultimate strength was noticeably lower than that of the QI continuous fibre baseline, tensile strength being the weakest, followed by compression and flexure. Strength and modulus of all three properties studied increased with longer strand length. Tensile strength and modulus were also found to be strongly dependent on panel thickness — the average ultimate tensile strength doubled between the 2 mm and 6 mm panel thickness. Similarly, the average modulus increased by 50% between those two thicknesses. As opposed to continuous fibre composites, the compressive strength of the DLF composite panels was higher than its tensile strength. The same trend was reported by other authors [34,37] and material data sheet [38] for carbon/PEEK DLF composites. Failure was found to be matrix-dominated, dominated by transverse chip cracking, longitudinal chip splitting, and chip delamination/debonding, with little or no fibre breakage.

Feraboli *et al.* [29] reported that although the average elastic modulus of DLF composites is nearly equivalent to that of a continuous fibre QI benchmark, its variability can be as high as 19% when measured by means of strain gauge or extensometer. To investigate this behaviour, a series of tensile tests were conducted while varying strain gauge length and location. The results were compared with multiple extensometer readings and full-field surface strain obtained via Digital Image Correlation (DIC) [39]. Experiments showed that

the surface strain variation of the specimens measured by DIC can vary by as much as 50%, with a coefficient of variation as high as 17% [29,31]. Digital image correlation was shown to be the most repeatable technique. It was concluded that due to their inability to capture the variability of the material, strain gauges or extensometer should not be employed for strain measurement of DLF composites.

In an attempt to identify some of the specific characteristics that can influence the quality and performance of DLF composites, a detailed analysis of their meso-structure was conducted [30]. Regions of high attenuation obtained via ultrasonic C-scan were cut and analyzed with the help of optical microscopy. The hot spots located with ultrasonic C-scan corresponded to real defects such as macro-voids, fibre swirls/kinks resulting from high flow, or resin-rich regions. The fibre volume content in the defects regions was found to be on average 9% lower than that of the nominal material, 59%. It was also reported that ultimate tensile failure only occurred near hot spots in 50% of the cases. It was thus concluded that conventional ultrasonic inspection may not be acceptable for DLF composites, as it could result in high rejection rate, without necessarily providing confidence in part quality and performance.

Feraboli *et al.* [28] investigated the notched behaviour of the material under tensile and compressive load. A notch-insensitive behaviour was observed, where the reduction in load-carrying capability was almost directly proportional to the reduction in available cross-section area due to the hole. The open-hole tensile strength of the material was found to be virtually insensitive to the presence of a 3 mm hole, where most samples failed in the gross section, away from the hole. The results for the notched tensile and compressive strength are summarized in Fig. 2.2. The figure depicts the notch-sensitive ($1/K_t$ curve) and notch-insensitive (1:1 solid line) behaviours, and shows data from [28] for

carbon/epoxy DLF composites and [40] for typical continuous fibre composite laminates. The notched-sensitive behaviour was attributed to internal stress concentrations arising from the discontinuous, thus heterogeneous nature of the material. This result suggests that the stress concentrations due to the material's discontinuous nature can be larger than the stress concentrations due to the geometry of the component. Finally, it was recommended that common analysis methods used for continuous fibre composites materials should not be employed to predict the notched strength and location of failure of DLF composites.

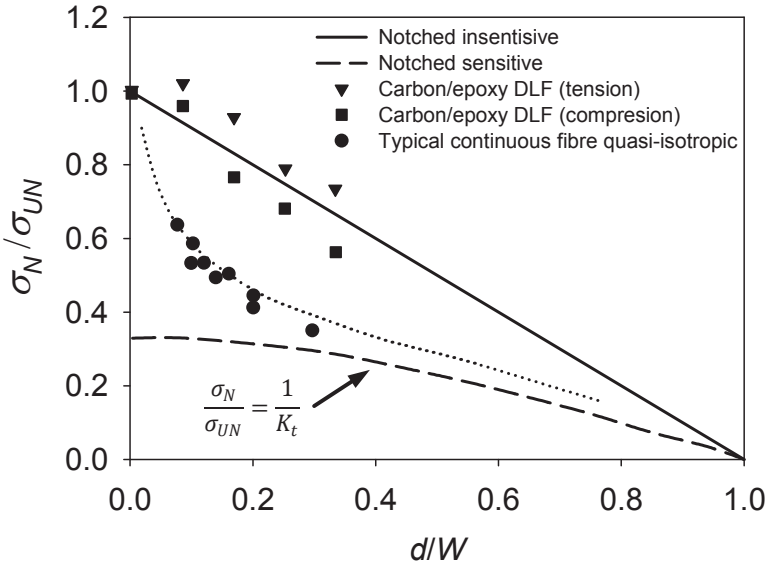

Figure 2.2 – Open-hole tensile strength vs. d/W showing notch-sensitive and notch-insensitive behaviours. The results are normalized with their respective un-notched tensile strength. Experimental data from [28] for carbon/epoxy DLF composites and [40] for typical continuous fibre composite laminates are shown on the figure.

A comprehensive study to identify the source of failure initiation in Hexcel HexMC™ DLF composites was conducted by Boursier and Lopez [41]. It was observed that under tensile loading, first cracks generally occur at the surface

of the specimen, in strands oriented off-axis to the loading direction, and in the resin-rich boundary around each individual strand. It was also reported that most cracks inspected were at the located near the edges of the specimen. Cross-sectional micrographs revealed that cracks were initiated in resin rich areas and surface defects such as voids. Overall, the crack initiation was attributed to pin holes, resin pockets or other molding defect located at the surface of the specimens. Moreover, a large number of first cracks were observed near the edges of the tensile specimens. This was attributed to the shorter cut strands located at the edges of the specimens and possible damage induced from the machining operation. Despite those observations, no correlation was found between the stress at the first audible crack and the ultimate tensile strength of the material.

2.3.2.2 Thermoplastic-based DLF composites

Table 2.3 shows the specific tensile properties of carbon/PEEK DLF composites compared to steel, aluminum and titanium [7,38]. While specific modulus is similar for all materials, the specific strength of thermoplastic-based DLF composites is much higher than that of aluminum and steel. Eguémann *et al.* [42] investigated the effect of strand length on the tensile properties of this material and compared the results with those obtained by Feraboli *et al.* [6] on carbon/epoxy DLF. The results showed that the two material systems have similar moduli, and similarly to epoxy-based DLF composites, the modulus of carbon/PEEK DLF composites was not influenced by the strand length. In contrast, the tensile strength of PEEK-based DLF composites was shown to be much higher than its epoxy-based counterpart. For strand lengths ranging from 10 mm to 40 mm, the tensile strength was on average 74% higher. Since the typical failure modes of DLF composites are matrix failure and strand debonding [6,42], the superior mechanical performance of carbon/PEEK DLF

composites was attributed to the superior shear strength and fracture toughness of PEEK matrix.

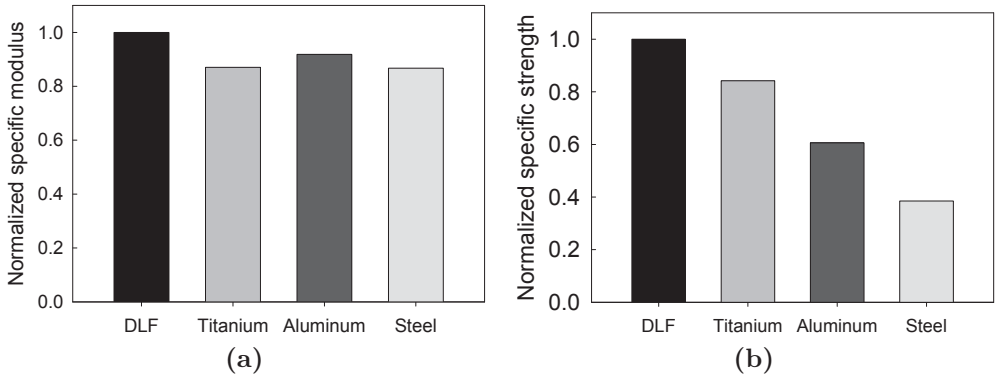

Figure 2.3 – Comparison of the normalized specific tensile properties of DLF vs. typical metals [7]. a) Tensile modulus. b) Tensile strength.

Han *et al.* [37] investigated the effect of hybridization — the combination of continuous and discontinuous fibres in the same part. Tensile, compressive, in-plane shear, and bearing strength of flat panels carbon/PEEK DLF composites co-moulded with woven fabric prepreg layers were evaluated. Experimental results showed an improvement in tensile and compressive strength with the addition of fabric content in the DLF laminates. The bearing strength was 30% higher in 100% DLF panels in comparison with 100% continuous fibre fabric. Interestingly, the highest bearing strength was achieved by moulding the DLF chips with fabric reinforcement in the core of the panel.

Han *et al.* [43] studied the impact behaviors of carbon/PEEK DLF composites and compared the results with a continuous fibre composite baseline. The impact response of the DLF composite coupons was found to be similar to that of the continuous fibre panel. Micro-CT was employed to characterize the impact damage, where it was observed that although the maximum damage diameter

was significantly larger in the DLF laminates, the total volume of damage was similar to that of continuous fibre panels. The difference in damage distribution was attributed to the different fibre architectures of the two laminates. The DLF laminates also had superior normalized residual compressive strength after impact. Overall, it was concluded that DLF composites are more suitable than continuous fibre composites for structural applications where impact damage tolerance and post-impact efficiency are required.

In her work, Selezneva [44–46] investigated the mechanical properties of carbon/PEEK DLF composites. It was found that the tensile, compressive and shear properties of DLF composites are highly influenced by the strand geometry, where longer strands generally leads to an increase in strength. Although the panel thickness (3 mm vs. 6 mm) did not influence the modulus of the three mechanical properties studied, slightly higher tensile and shear strength were measured with thicker panels.

Two major practical recommendations were made with regards to the use of DLF composite materials. First, it was recommended that smaller strand size and thicker panels should be employed in order to obtain more statistically homogeneous properties. This is based on the fact that the use of longer strands, although leading to better mechanical properties, will result in higher material heterogeneity, lower design allowables, and inferior dimensional stabilities. For the same reasons, manufacturing of thin components (< 2 mm) is not recommended. Second, the use of tough thermoplastic matrices was recommended over more brittle thermoset-based counterpart. This result is driven by the fact that the failure modes of DLF composites, observed experimentally and numerically, are mainly interlaminar. Similar findings were reported by Eguémann *et al.* [42].

The work by Tuttle *et al.* [33] on carbon/epoxy high-flow moulded DLF composites showed a significant increase tensile strength with panel thickness. In the region where the initial stack of material was placed, the tensile strength was on average 89% higher in 5.8 mm thick panels, when compared to that of 2.3 mm thick panels. This is in contrast with Selezneva's results, which were obtained by low-flow moulding (initial mould coverage of 100%). The large discrepancy between the two studies demonstrates how processing and the choice of material, i.e. thermoset vs. thermoplastic, can influence the mechanical behaviour of DLF composites.

2.3.3 Recycling

Roux *et al.* [47,48] and Eguémann *et al.* [10,42,49] demonstrated a cradle-to-cradle recycling process for carbon/PEEK DLF composites, referred to as electro-dynamical fragmentation. The operation was performed by putting the material to be recycled in a closed vessel containing water and subjecting it to 150–200 pulsed electric discharges, typically between 100 kV to 200 kV. The fragments were then separated from the residues and classified by size. Large fragments were re-submitted to the process. It was noted that the geometry of the fragments was much different than the original bulk material — they were smaller than the original strand size, and typically composed of several through-the-thickness layers. Fragments obtained from a door hinges moulded with 20 mm long strands [10] were between 0.5 mm to 4 mm long. The process can also partially remove the polymer at the surface of the fragments, exposing bare fibres. The strength of the recycled door hinges was 15% lower than that of the original hinges. The lower properties of the recycled part was attributed to the size of the recycled fragments and the removal of the polymer at their surface. Nonetheless, the recycled hinges showed better strength than a counterpart produced from injection moulding granules (fibre length < 1 mm).

Leblanc *et al.* [50] investigated two recycling approaches for carbon/PEEK composites. First, small 19 mm × 6 mm specimens cut from a 3 mm thick flat DLF part were mixed with various amounts of 13 mm long virgin strands and remoulded into a 100 mm × 100 mm panel. The recycled material was used as is, without any shredding/fragmentation operation. The flexural strength measured on coupons moulded with 20% of recycled material by weight was similar than that of the baseline moulded with virgin strands. However, a significant drop in flexural strength was observed above 30% of recycled material. The reduction was attributed to the reduced fibre length compared to virgin strands, and potential knit lines formed between adjacent recycled specimens. In the second approach, the dimensions of the recycled material was 50 mm × 50 mm. Four recycled specimens were stacked in the center of the mould cavity, and press moulded into a 100 mm × 100 mm panel. This strategy was employed to minimize the formation of knit lines. The flexural strength of the recycled panel was 25% when compared to the baseline. It was found that the improved properties were the result of a change in overall microstructure of the recycled laminate. The extended amount of flow experienced by the pre-consolidated charges allowed for a reduction of resin-rich regions, improvement in strand alignment, and better in-plane strand orientation distribution, which resulted in superior mechanical performance.

2.4 Effect of porosity

Porosity is one of the most detrimental defects formed during manufacturing of composites [2]. Although no data has been reported in the literature for thermoset or thermoplastic DLF composites, the effect is well documented for continuous fibre reinforced polymers (CFRP). Porosity is known to have a significant effect on matrix-dependent properties of CFRP, mainly because it is

the source of stress concentration and can act as failure initiation points [51]. The most significantly affected properties include interlaminar shear [52–55], transverse tensile [54,56], flexural [52,57], and compressive strength [52]. It is also widely accepted that the longitudinal tensile properties of CFRP are not affected by voids [54,56].

2.5 Thermomechanical properties

Thermomechanical properties of composites are primarily employed in the study of residual stresses. During cooling from melt, a semi-crystalline thermoplastic matrix will experience thermal contraction and crystallization shrinkage. The linear coefficient of thermal expansion (CTE) of neat and carbon fibre reinforced PEEK were measured via Thermomechanical Analysis (TMA) [58,59], using strain gauges embedded in the material [60] or bonded to its surface [61]. Thermal strain was measured during heating from 25 °C to 300 °C for neat PEEK [59], semi-crystalline carbon/PEEK [58,61], and amorphous carbon/PEEK [60]. The CTE parallel to the fibre direction was shown to be very low and is assumed to be zero [58,60].

Modulus as a function of temperature was measured by means of Dynamic Mechanical Analysis (DMA) [58,61–63]. Transverse modulus was reported during heating from 25 °C to 300 °C for amorphous [63] and semi-crystalline carbon/PEEK [58,61,63]. For the latter, data shows a gradual decline in modulus as the temperature is increased from room temperature. Toward T_g, the modulus drops significantly, followed by an almost linear decline from 175 °C to 300 °C. A similar behaviour was observed for the axial modulus of carbon/PEEK composites [58]. It should be pointed that all data reported for thermal/crystallization shrinkage and modulus of carbon/PEEK were obtained during heating. The effect of cooling rate and degree of crystallinity was thus

not considered. A comprehensive review on experimental techniques developed to measure thermomechanical properties of thermoplastic can be found in [64].

Chapman *et al.* [65] proposed a model to predict the in-plane residual stresses of carbon/PEEK laminates induced during cooling. Micromechanics were employed to evaluate the variation of mechanical properties as a function of temperature and degree of crystallinity. The transverse thermal shrinkage was modeled using CTE values reported in the literature for temperatures below and above T_g. Crystallization shrinkage of PEEK was estimated based on a volume shrinkage of 25% for a volume fraction crystallinity of 30% reported in [66]. The isotropic modulus of neat PEEK was modeled by coupling the temperature independent properties of the crystalline phase with temperature dependant properties of the amorphous phase. Continuous fibre micromechanics were then employed to predict the temperature dependant properties of carbon/PEEK laminate. None of the two models were validated against experiments.

2.6 Summary

The work carried out on DLF composites has demonstrated their fast, low-cost, and excellent forming capabilities, as well as their superior mechanical properties compared to short discontinuous fibre material systems. They are thus an excellent candidate for the manufacturing of complex-shaped and high-performance composite parts. The mechanical properties and heterogenous behaviour of thermoset and thermoplastic DLF composites has been well described in the literature. However, most of the analyses were performed on coupons obtained from flat panels, which were usually reported to be free of porosity. Since this material is intended to be employed to mould complex geometries, the quality of real parts may differ substantially from that obtained from simple geometries. For thermoplastic composites, it is expected that the

part quality will be influenced by processing effects such as thermal and crystallization shrinkage, non-isothermal heating and/or cooling, uneven pressure distribution, air entrapment, etc. A link is thus needed between processing and mechanical performance. In this work, this will be established by pinpointing the main causes of defect formation and identifying the circumstances under which they occur during the moulding process. This will be achieved with the help of material characterization, focused experiments, and process modelling.

Chapter 3

Materials and Moulding Processes

This chapter details the materials and moulding procedure used in this thesis. The three different forms of carbon/PEEK employed are presented, followed by the recommended processing cycle for each material form/manufacturing technique. Finally, tooling, procedures, and moulding cycles employed to manufacture DLF and continuous fibre composite parts are described.

3.1 Materials

Carbon/PEEK unidirectional tape was used throughout this thesis. It has a fibre volume fraction of 59%, an areal weight of 218 g/m^2, and a consolidated ply thickness of 0.132 mm. The glass transition temperature (T_g) of the PEEK matrix is 143 °C and its melting temperature (T_m) is 343 °C. Three different forms of the material were utilized: 156 mm wide continuous fibre roll, 6.4 mm wide unidirectional slit tape, and pre-chopped discontinuous form. The slit tape was cut into 25 mm long strands using a Kingsing Machinery Co. Limited (Shanghai, China) automated tape cutter, model KS-915. The various forms of material are shown in Fig. 3.1.

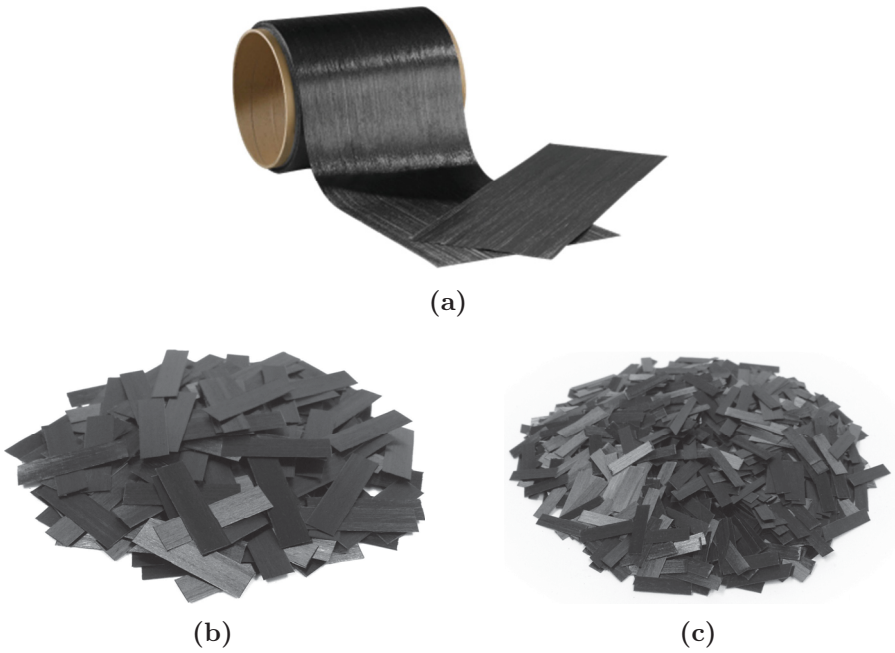

(a)

(b) (c)

Figure 3.1 – Carbon/PEEK tape in various forms. (a) Unidirectional tape. (b) 25 mm × 6.4 mm strands. (c) 13 mm × 3.2 mm strands.

3.2 Processing cycle

The recommended processing cycles for unidirectional and chopped carbon/PEEK tape are presented in Table 3.1. It was pointed in [7] that pressure higher than 69 bar might be required for more complex DLF composite parts.

3.3 Moulding procedures

3.3.1 Small DLF composite panel

Small flat DLF composite panels were moulded in an instrumented hot press, shown in Fig. 3.2a. The setup was inserted in an MTS (Eden Prairie, MN) 250 kN load frame. Each H13 steel platen is 100 mm × 100 mm. A picture

Table 3.1 – Material supplier's recommended processing cycle for carbon/PEEK unidirectional and chopped tape.

Process	Press lamination	Autoclave lamination	Compression moulding
Material form	Unidirectional tape	Unidirectional tape	Chopped tape
Temperature (°C)	370 – 400	370 – 400	370 – 400
Dwell pressure (bar)	7 – 21	7 – 21	34 – 69
Dwell time (min)	15 – 30	5 – 30	0 – 2
Cooling rate (°C/min)	5 – 20	5 – 20	5 – 20

frame was inserted around the bottom platen to create a mould cavity. The platens were heated using a total of eight 500 W FIREROD® heating cartridges from Watlow (St. Louis, MO). The temperature of each platen was controlled independently by an SD Series PID controller from Watlow. The fixture was cooled using compressed air, while the cooling rate was maintained using the ramp function of the PID controllers.

The moulding procedure was the following: two layers of Frekote 700-NC release agent were applied to the platen surfaces and the picture frame before moulding. The strands, 25 mm long and 6.4 mm wide, were manually placed inside the mould cavity in small batches and shuffled in order achieve a random in-plane distribution and minimize out-of-plane orientation. The material in the mould cavity before processing is shown in Fig. 3.2b. Fifty-four grams of carbon/PEEK DLF material was used to obtain a nominal panel thickness of 3.2 mm. After the material placement, the mould was closed, a pressure of 10 bar was applied, and the press platens were heated to 380 °C. Once the target processing temperature was reached, the desired dwell pressure was applied.

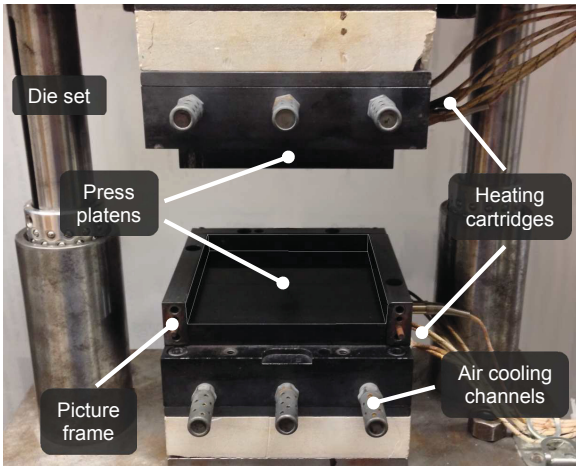

(a)

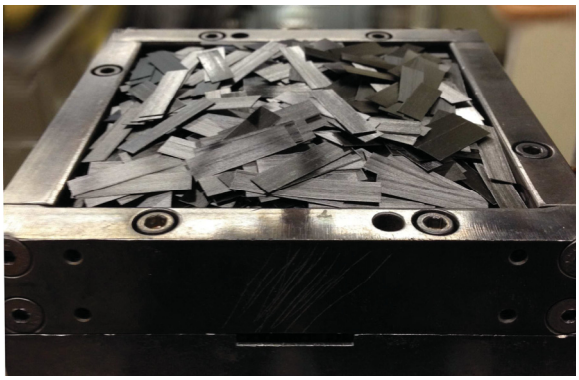

(b)

Figure 3.2 – Small flat DLF composite panel moulding setup. (a) Instrumented hot press. (b) Carbon/PEEK prepreg strands placed in the mould cavity before processing.

The material was then held at 380 °C for 15 min to ensure isothermal conditions. After the dwell, the desired cooling pressure was applied and the setup was cooled to room temperature at a rate of 10 °C/min, followed by the panel ejection. The nominal moulding cycle was just above 80 min, as presented in Fig. 3.3.

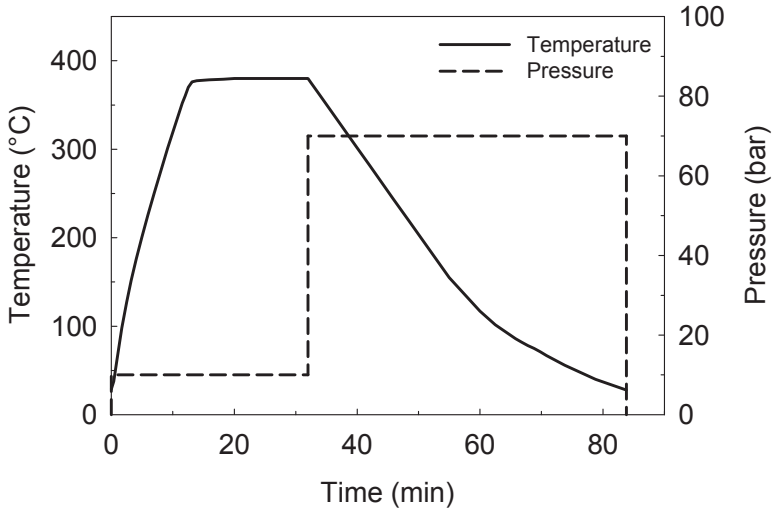

Figure 3.3 – Nominal moulding cycle for a flat plate using the instrumented hot press.

3.3.2 Large DLF composite panel

Large flat DLF composite panels were manufactured using a compression moulding tool that consists of an invar picture frame and two H13 steel flat plates. The mould cavity is 356 mm × 305 mm. The moulding procedure was the following: two layers of Frekote 700-NC release agent were applied to the platen surfaces and the picture frame before moulding. Following the strand placement procedure discussed in the previous section, 776 g of 25 mm × 6.4 mm carbon/PEEK DLF material was used to obtain a nominal panel thickness of 4.5 mm. Three thermocouples were inserted in the material at approximately 13 mm from the picture frame (Fig. 3.4). They were used to monitor the material's temperature during the moulding cycle. The setup is shown in Fig. 3.5. After the material placement, the mould was closed and placed in a 150 ton Wabash (Wabash, IN) hydraulic press. A pressure of 8.2 bar was applied, and the target temperature of the press platens was set to 400 °C. Once the material reached 380 °C, the desired moulding pressure was applied

and kept constant for the rest of the cycle. The material was held at the processing temperature for 15 min. After the dwell, the press platens were brought to room temperature following cooling cycle recommended by Wabash: with air from the processing temperature to 343 °C, a mixture of air and water from 343 °C to 177 °C, followed by water from 177 °C to room temperature. The nominal cooling rate during the last stage of cooling was 19 °C/min. The nominal moulding cycle for a panel processed at 35 bar is presented in Fig. 3.6.

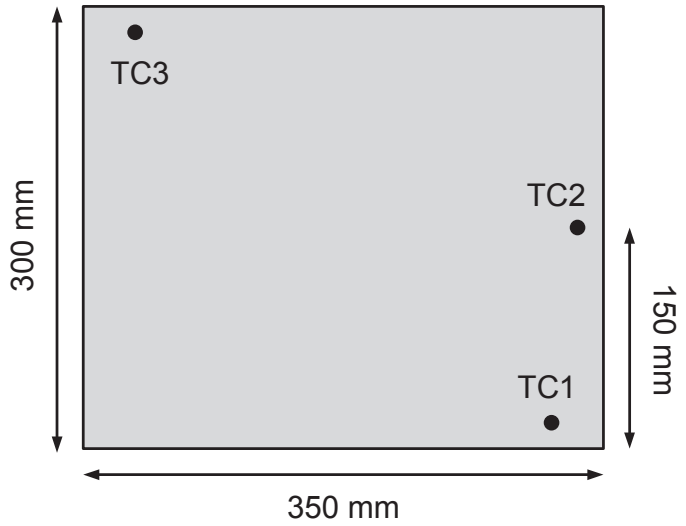

Figure 3.4 – Position of the three thermocouples inserted in the material before moulding. TC1 and TC3 were 13 mm from the edges and 38 mm away from the corners.

3.3.3 DLF composite L-bracket

Net-shape DLF composite L-brackets were manufactured using the compression moulding tool shown in Fig. 3.7. The setup was placed in a 50 ton Savage (Cleveland, OH) hydraulic press. The tool was heated using a total of eight FIREROD® heating cartridges from Watlow: four 1000 W cartridges

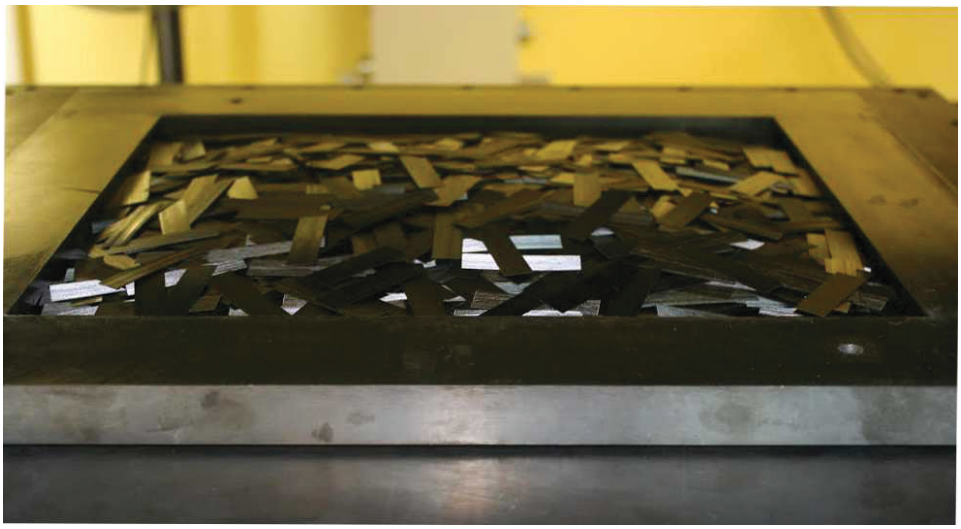

Figure 3.5 – Large flat panel moulding setup showing the DLF strands placed in the mould cavity before processing.

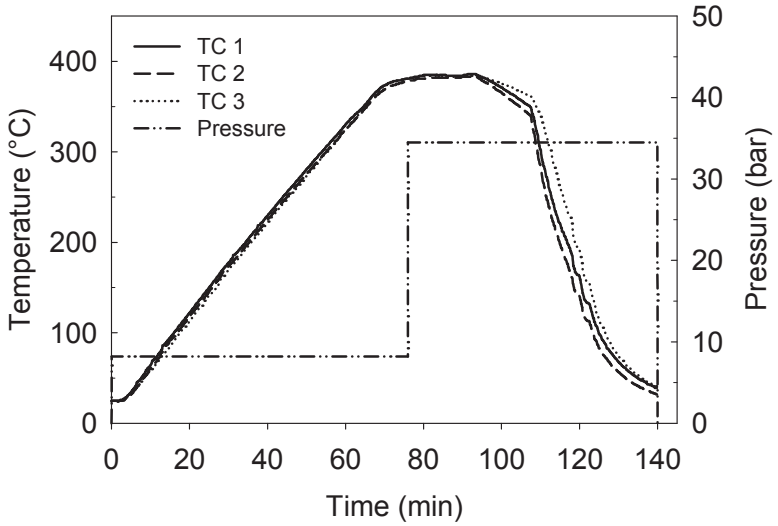

Figure 3.6 – Nominal moulding cycle for a large 356 mm × 305 mm DLF composite panel.

were located in the bottom frame, while four 500 W cartridges were vertically positioned in the punch. The temperature of each component was independently controlled by an Omega (Stamford, CT) PID controller, model CN7800. A thermocouple probe inserted in each component was used for temperature control, while another pair was employed for temperature measurement using a data acquisition system. The position of each probe is shown schematically in Fig. 3.8. The fixture was cooled using compressed air, with six channels in the bottom frame and four channels in the top of the punch. The L-bracket geometry is presented in Fig. 3.9. Details on the tool design can be found in [11].

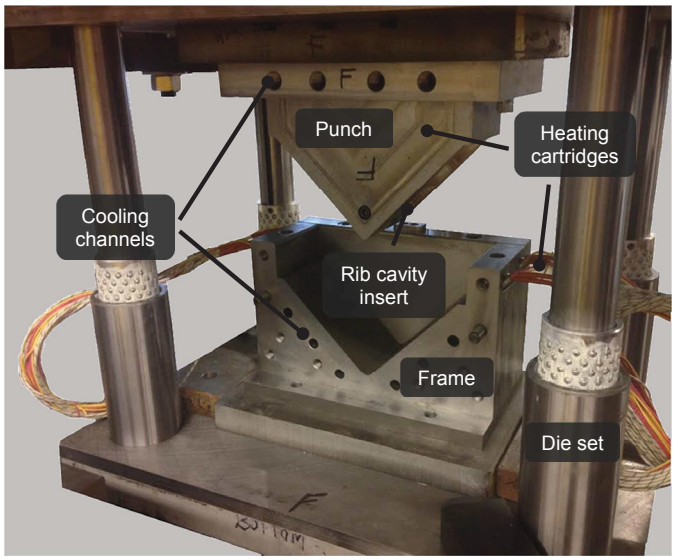

Figure 3.7 – L-bracket mould. Four vertical heating cartridges are embedded in the punch.

The moulding procedure was the following: two layers of Frekote 700-NC release agent were applied to the mould surfaces before moulding. One hundred and five grams of 13 mm × 3.2 mm carbon/PEEK DLF material was used to obtain a nominal bracket flange thickness of 3.2 mm. Since material placement is impractical due to the mould geometry, the latter was simply deposited at

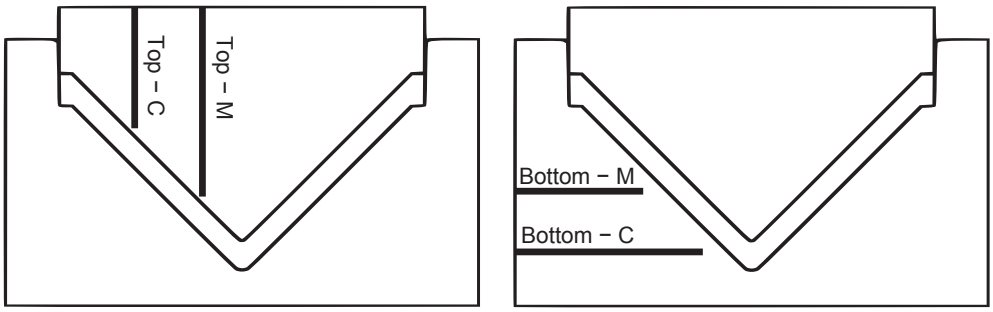

(a) Side view – Plane A. **(b) Side view – Plane B.**

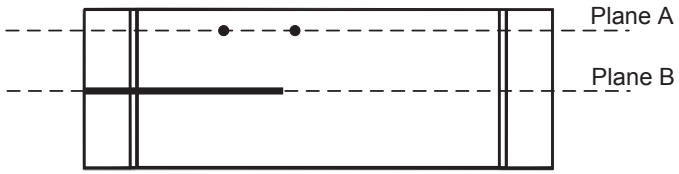

(c) Top view.

Figure 3.8 – Position of the temperature control "C" and temperature measurement "M" thermocouples inserted in the L-bracket tool. The top view in (c) is showing the position of planes A and B. The temperature was measured at the tip of each probe.

the bottom of the cavity in two separate batches. After the material placement, the mould was closed, a contact pressure was applied and the tool was heated to 385 °C. Once the target processing temperature was reached, three debulk cycles were performed by applying and releasing the desired moulding pressure. This helped evacuating the air trapped in the rib section of the part. The moulding pressure was held for 5 min after the debulk cycle. After the dwell, the setup was cooled to 250 °C at a nominal rate of 6 °C/min, followed by the part ejection. The nominal moulding cycle was just below 80 min.

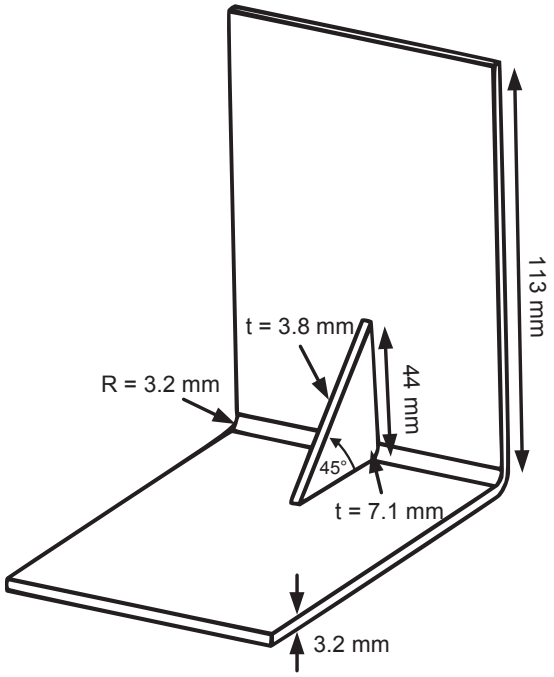

Figure 3.9 – L-bracket geometry. The rib has a 3° draft on each side.

3.3.4 Continuous fibre panel

Flat continuous fibre panels were manufactured in a Baron (Santa Fe Springs, CA) BAC-23 autoclave. Prior to autoclave processing, the 19 mm thick flat aluminum tool was coated with two layers of Frekote 700-NC release agent. Unidirectional carbon/PEEK tape plies were then laid directly on the tool. A fibreglass peel ply and breather material were placed above the laminate. A combination of high- and low-temperature sealing tapes were positioned on the mould perimeter and high temperature bagging material was used to finalize the vacuum bag. Three thermocouples were placed on the composite surface, along the length of the part. The autoclave was controlled based on the average temperature of the three thermocouples. The part was heated to a processing temperature of 380 °C at a rate 2 °C/min and maintained for 60 min. The consolidation pressure was applied once the part reached its glass transition

temperature, while vacuum was maintained during the entire cycle. The part was cooled to room temperature at a rate of 15 °C/min. The nominal moulding cycle of a panel processed under a consolidation pressure of 5 bar is presented in Fig. 3.10.

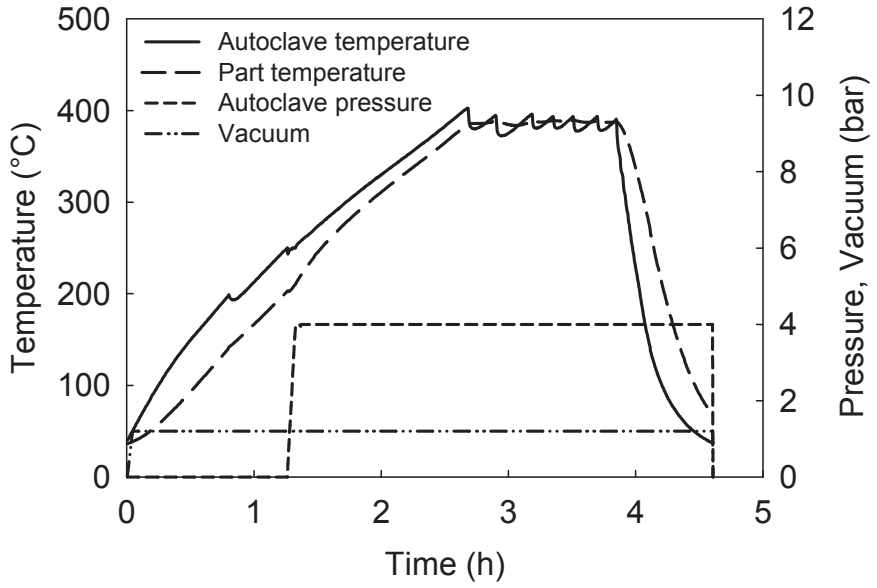

Figure 3.10 – Nominal moulding cycle for an autoclave processed panel.

3.4 Summary

A summary of the different composite parts manufactured in this study is presented in Table 3.2. It should be pointed out that the cooling rate of the large panel was governed by the cooling of the press platens, which could not be modified. Similarly, the cooling rate of 6 °C/min for the L-bracket was the maximum that could be obtained using only air as a cooling medium. Finally, the table shows the moulding pressure range tested for each part, where

the highest number in the range indicates the pressure required to obtain a defect-free part.

Table 3.2 – Summary of the different parts and manufacturing parameters used in this study.

Part	Material/Layup	Moulding pressure (bar)	Cooling rate (°C/min)
Small panel	DLF	10 – 110	10
Large panel	DLF $[45/–45/0/90]_{4S}$	10 – 35	19
L-bracket	DLF	50 – 200	6
Continuous fibre panel	$[0°]_{15}$ and $[0°]_{26}$	1.3 – 5.0	15

Chapter 4

Thermomechanical Properties of Carbon/PEEK composites

In this chapter, thermomechanical properties of carbon/PEEK composites are measured during crystallization from the melt temperature using thermal analyses. First, the crystallization kinetics are characterized by differential scanning calorimetry. Typical cooling rates for DLF composites are tested, i.e. 1 °C/min to 20 °C/min. Second, thermal and crystallization shrinkage is measured using thermomechanical analysis. Third, the evolution of the modulus from the melt temperature was characterized with dynamic mechanical analysis.

4.1 Crystallization kinetics

Crystallization kinetics of unprocessed carbon/PEEK was characterized via Differential Scanning Calorimetry (DSC). All tests were performed on a TA Instruments (New Castle, DE) Q100 differential scanning calorimeter. A stack of small flakes of material, approximately 2 mm × 2 mm, were inserted in each DSC pan. The specimens were heated to 380 °C and held for 10 min to erase the crystallization history of the material [67]. They were then cooled to room temperature at various cooling rates: 1, 5, 10, and 20 °C/min. Each dynamic test was repeated with three different specimens.

To extract the evolution of crystallization during cooling for each dynamic test, the DSC heat flow signal was plotted as a function of time, and a linear integration of the area under the crystallization peak was used to calculate the heat generated. Since the cooling rate is constant, the weight fraction crystallinity can be expressed as a function of temperature during cooling [67]:

$$X_{mc}(T) = \frac{H_c(T)}{(1 - M_f)H_f} \tag{4.1}$$

where X_{mc} is the weight fraction crystallinity, H_c is the enthalpy of crystallization measured as a function of temperature, M_f is the mass fraction of fibres, and H_f is the enthalpy of fusion of the fully crystalline matrix. The mass fraction crystallinity was then converted to volume fraction crystallinity using [68]:

$$X_{vc} = \frac{X_{mc}\rho_a}{\rho_c - X_{mc}(\rho_c - \rho_a)} \tag{4.2}$$

where ρ_a and ρ_c are the densities of amorphous and crystalline material, respectively. Typical phase densities and heat of fusion of PEEK are listed in Table 4.1.

Table 4.1 – Typical properties of PEEK polymer [68].

Property	Value
Heat of Fusion, H_f (J/g)	130.1
Amorphous phase density, ρ_a (g/cm^3)	1.26
Crystalline phase density, ρ_c (g/cm^3)	1.40

A typical DSC thermogram showing the measured heat flow vs. temperature during heating and cooling is presented in Fig. 4.1. The crystallization kinetics

of carbon/PEEK prepreg obtained with Eqs. 4.1 and 4.2 for cooling rates between 1 °C/min and 20 °C/min are presented in Fig. 4.2. Each curve is the average of three specimens. As expected, the cooling rate clearly affected the temperature range of crystallization, shifting it from ∼297–326 °C at 1 °C/min to ∼250–307 °C at 20 °C/min. Nonetheless, the final X_{vc} was unaffected by the cooling rate, except at 1 °C/min where it was found to be 6% lower than the average measured value of 33.2%. The average degree of crystallinity as a function of cooling rate measured in this work are directly in the range reported in the literature for carbon/PEEK and neat PEEK, as shown in Fig. 4.3. The temperature range of crystallization of carbon/PEEK prepreg as a function of cooling rate is shown in Fig. 4.4. The results are presented for four relative degree of crystallinity, where 0% indicates the start of crystallization.

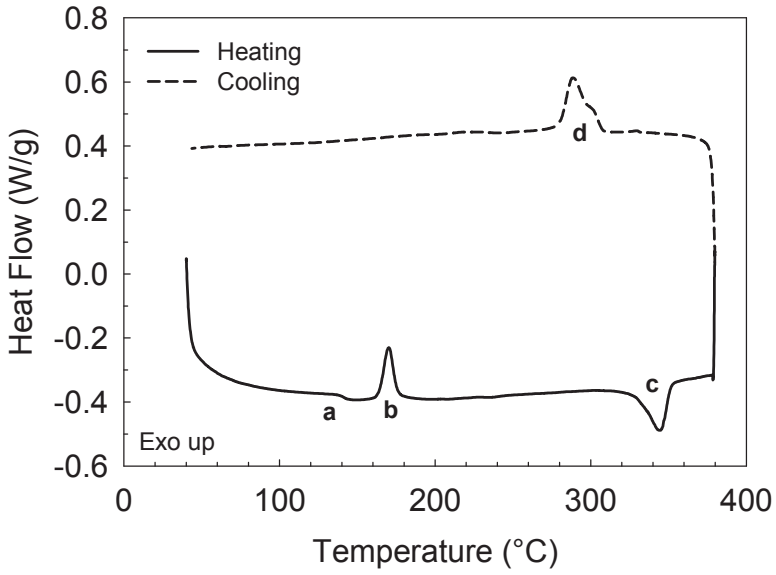

Figure 4.1 – Typical DSC thermogram of unprocessed carbon/PEEK. (a) Glass transition temperature, T_g. (b) Recrystallization after T_g. (c) Melting at T_m. (d) Crystallization during cooling. Heating and cooling rates were 10 °C/min.

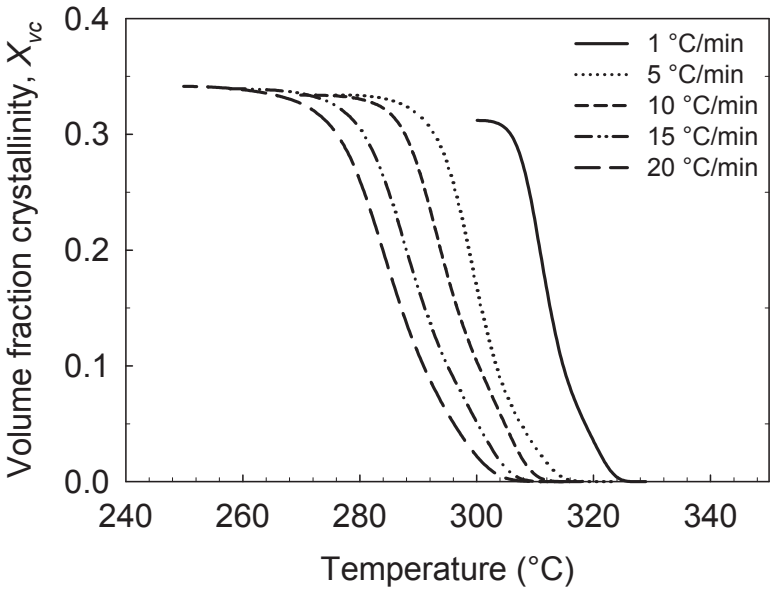

Figure 4.2 – Evolution of the volume fraction crystallinity of carbon/PEEK prepreg for different cooling rates.

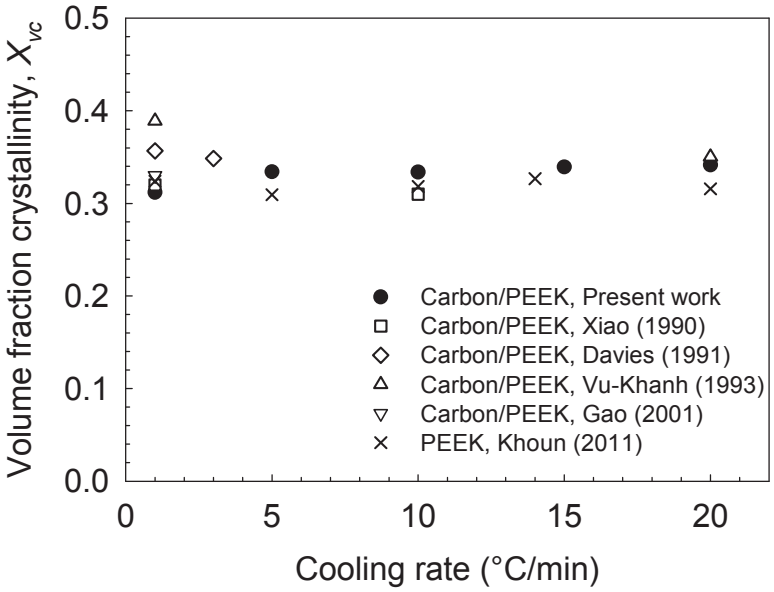

Figure 4.3 – Degree of crystallinity of neat PEEK and carbon/PEEK as a function of cooling rate.

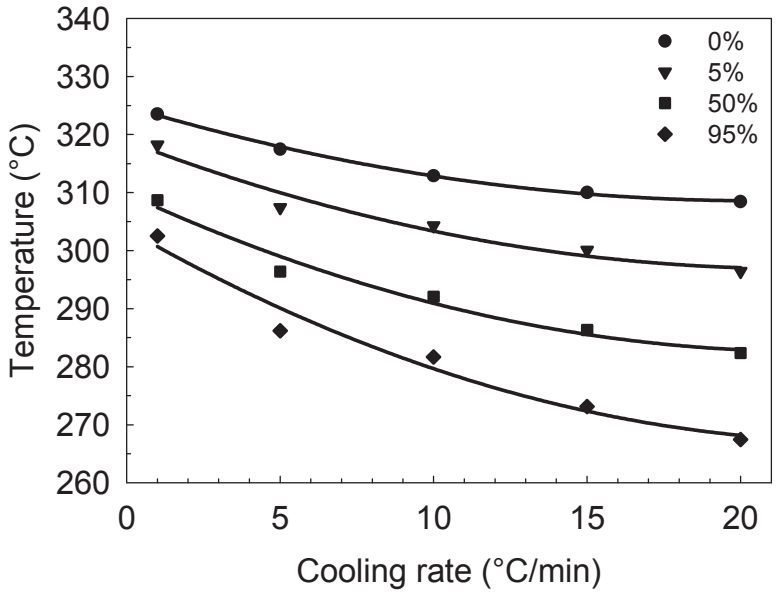

Figure 4.4 – Crystallization temperature range vs. cooling rate of carbon/PEEK prepreg for four relative degree of crystallinity, where 0% indicates the start of crystallization.

4.2 Thermomechanical analysis

The thermal and crystallization shrinkage of carbon/PEEK composites were measured via TMA. The experiments were performed on a TA Instruments Q400 thermomechanical analyzer equipped with a MCA70 cooling accessory and a macro-expansion probe. Several 6.3 mm square specimens were cut from a 4.3 mm thick defect-free continuous fibre carbon/PEEK panel with a stacking sequence of $[45/–45/0/90]_{4S}$. The panel was manufactured with continuous fibre tape under a moulding pressure of 30 bar, using the procedure described in Section 3.3.2. The thermal expansion of the specimens was measured from 25 °C to 380 °C in the fibre direction (in-plane, $\varepsilon_{11} = \varepsilon_{22}$) and perpendicular to the fibres (out-of-plane, ε_{33}). The test setup is shown in Fig. 4.5. Before the experiment, the thickness of the specimen was measured with a preload of 0.05 N. It was then sandwiched between two quartz discs coated with Frekote

700-NC release agent. Quartz has a linear coefficient of thermal expansion of 0.33 με/°C [72], which is negligible compared to that of carbon/PEEK laminates. The setup was heated to 380 °C at a rate of 1 °C/min, under a constant load of 0.1 N. A 10 min temperature hold was performed in order to completely erase the crystallization history of the material. The setup was then brought to room temperature at the same rate. The slow cooling rate was selected to minimize thermal gradient in the specimen, since the heat transfer mechanism of the TMA is convection. Two specimens were tested in the direction perpendicular to the fibres and one specimen was tested in the fibre direction.

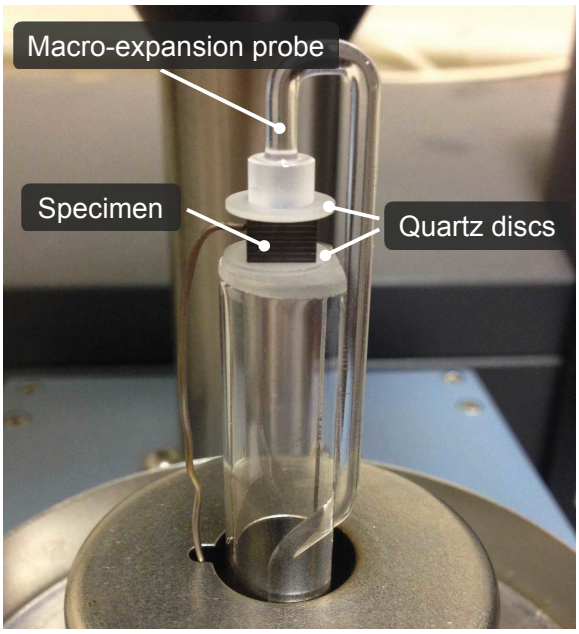

Figure 4.5 – Thermomechanical analysis test setup.

Thermomechanical analysis results for the first specimen tested in the out-of-plane direction are shown in Fig. 4.6. The rapid shrinkage during crystallization (point c) can be observed. The peak out-of-plane CTE measured during crystallization was 1247 με/°C, which is almost five times higher than before

crystallization. The latter, in conjunction with the narrow temperature range of crystallization, show the importance of minimizing part temperature variation during cooling. For example, a temperature variation of only 25 °C can lead to a shrinkage difference of over 2.6%. All CTEs measured at different stages during the cooling process are listed in Table 4.2. The reproductivity of the test is demonstrated by comparing the thermal strain of two specimens measured during cooling (Fig. 4.7). The difference between the two curves is simply due to variability in the crystallization kinetics of the material.

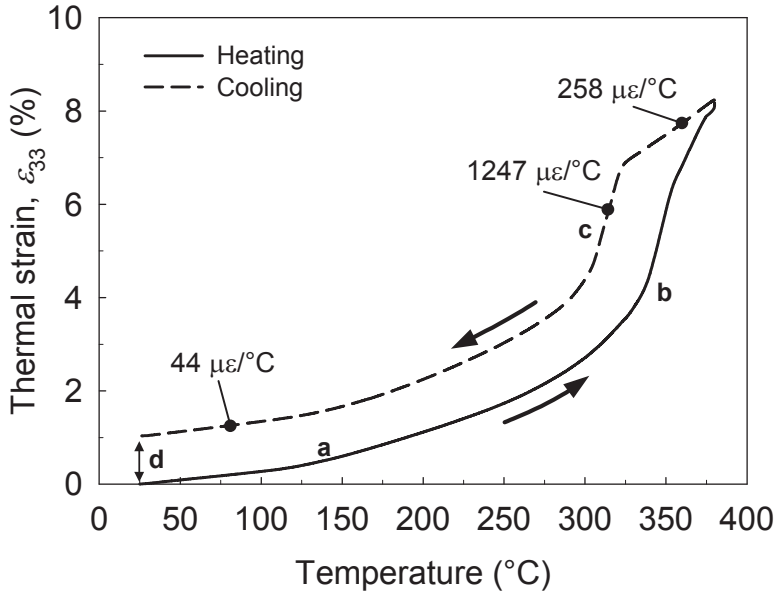

Figure 4.6 – Thermal and crystallization shrinkage of carbon/PEEK composites (out-of-plane, ε_{33}). (a) Amorphous phase softening at T_g. (b) Melting of the crystalline phase and deconsolidation at T_m. (c) Crystallization shrinkage. (d) Final specimen deconsolidation. Heating and cooling rates were 1 °C/min.

The results for the specimen tested in the fibre direction are shown in Fig. 4.8. An unusual behaviour was observed during crystallization (300–320 °C), where a rapid increase in the thermal strain was followed by a drop of the same magnitude. This is believe to be due to the rapid shrinking occurring in the

Table 4.2 – Out-of-plane linear coefficient of thermal expansion of carbon/PEEK composites measured at different stages during the cooling process.

Stage	Temperature range (°C)	CTE (με/°C)
Before crystallization	330–380	258
During crystallization	310–320	1247
Under T_g	25–120	44

out-of-plane direction of the specimen, which was 81 times higher than the magnitude of the spike. Moreover, the signal measured in Fig. 4.8 was not as smooth as the one measured in the out-of-plane direction. This behaviour is due to a combination of three factors. First, the amplitude of the displacement measured was very low (∼6 μm compared to ∼320 μm for ε_{33}). Second, the transverse deformation of the specimen is much larger than the one measured in the fibre direction, potentially leading to instabilities during the test. Finally, the two faces of the specimen might not be perfectly parallel, as they were cut with a diamond saw. In the out-of-plane direction, the two moulded faces are utilized, which can be assumed to be parallel. Nonetheless, the total strain measured during cooling from 380 °C to 25 °C was only 0.09%. It is thus a fair assumption to neglect the deformation in the fibre direction, since the strain is much larger in the out-of-plane direction (7.3%, Fig. 4.7).

4.3 Dynamic mechanical analysis

Thermoelastic properties of carbon/PEEK composites were characterized using DMA. The experiments were performed on a TA Instruments Q800 dynamic mechanical analyzer equipped with a three-point bend fixture. The 55 mm × 10 mm specimens were cut from a 2.2 mm thick defect-free continuous fibre car-

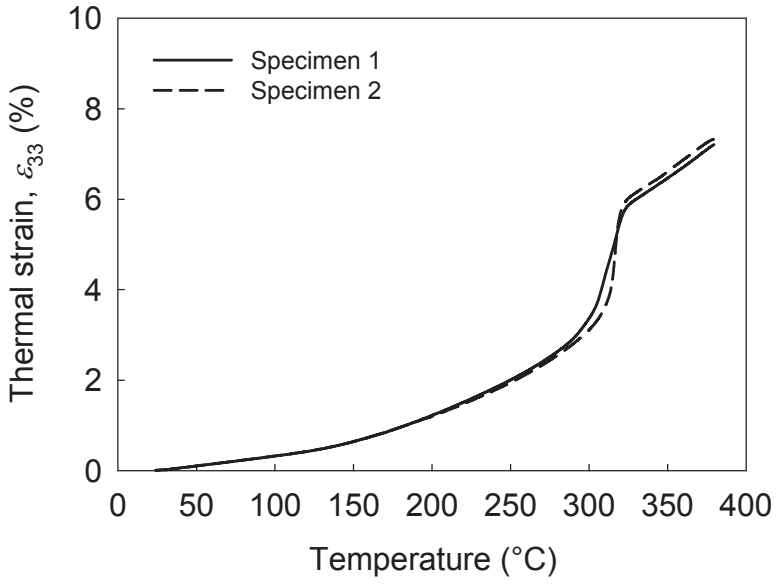

Figure 4.7 – Comparison between the out-of-plane thermal and crystallization shrinkage of two carbon/PEEK composites specimens measured during cooling. Both curves were offset to zero at 25 °C.

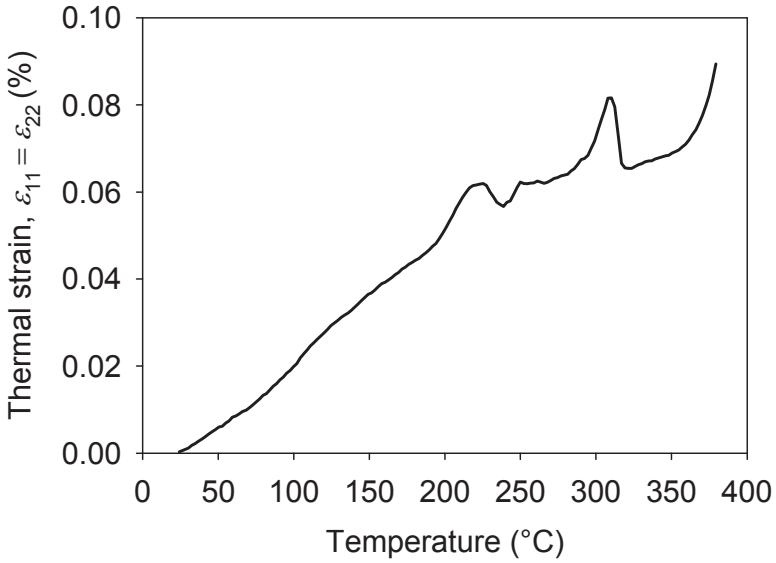

Figure 4.8 – Thermal and crystallization shrinkage of carbon/PEEK composites (in-plane, $\varepsilon_{11} = \varepsilon_{22}$). The curve was offset to zero at 25 °C.

bon/PEEK panel with a stacking sequence of $[0]_{24}$. The panel was manufactured under a moulding pressure of 70 bar and a cooling rate of 10 °C/min using the procedure described in Section 3.3.1. The fibres were oriented transversely to the longitudinal direction of the specimen. The storage modulus was measured during heating and cooling from 25 °C to 380 °C in the direction perpendicular to the fibres, at a rate of 1 °C/min. To minimize specimen deformation over the melt temperature, the latter was wrapped in 0.05 mm thick kapton tape. The test was performed at a frequency of 1 Hz and a constant strain of 0.1%. A total of two specimens were tested.

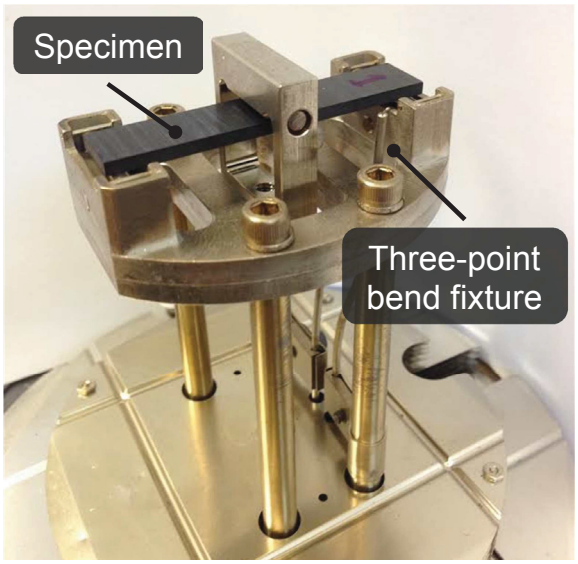

Figure 4.9 – Dynamic mechanical analysis test setup. The unidirectional fibres were oriented perpendicular to the length of the specimen.

The transverse modulus results of the first specimen tested are presented in Fig. 4.10. The specimen shows a linear decline in modulus from room temperature to T_g, followed by a sharp drop from T_g to 175 °C. At 200 °C, the modulus was 40% of its room temperature value. An almost linear decrease in

modulus was then observed until the melting point of the matrix at ∼350 °C. This is similar to the results reported by Unger and Hansen [63] during heating from 25 °C to 300 °C. The modulus development during cooling coincided with the crystallization of the matrix, between 300 °C and 325 °C at 1 °C/min (see Fig. 4.2). During cooling below 300 °C, the modulus is very close to that measured during heating. This is expected since the degree of crystallinity of the specimen is similar in both cases. After the test, a flexural deformation of 2 mm was measured on the specimen. This is due to the cycling load applied on the specimen over the melt temperature, where the modulus is very close to zero.

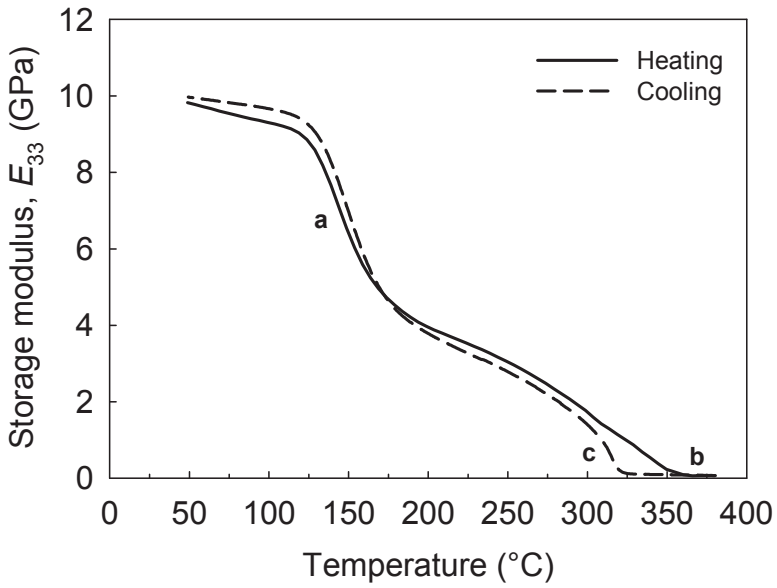

Figure 4.10 – Out-of-plane modulus of carbon/PEEK composites. (a) Amorphous phase softening at T_g. (b) Melting of the crystalline phase at T_m. (c) Crystallization. Heating and cooling rates were 1 °C/min.

The reproductivity of the test is demonstrated by comparing the storage modulus and Tan Delta of two specimens measured during cooling (Fig. 4.11). The low values of Tan Delta ($\ll 1$) observed in both tests suggest that the

material behaviour is mainly elastic in the range of temperatures tested. This is believe to be due to the high fibre volume fraction and high viscosity of the material before crystallization.

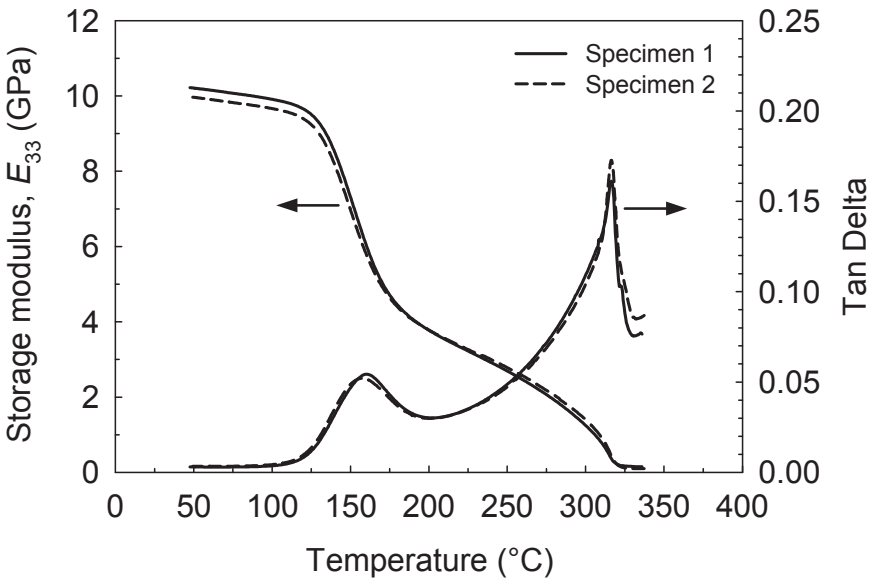

Figure 4.11 – Comparison between the storage modulus and Tan Delta of two specimens measured during cooling.

4.4 Summary

The evolution of three thermomechanical properties of carbon/PEEK composites during cooling was measured. First, the crystallization kinetics were characterized by differential scanning calorimetry. Typical cooling rates for DLF composites were tested, i.e. 1–20 °C/min. Second, thermomechanical analysis was utilized to measure the in-plane and out-of-plane shrinkage during cooling from the melt. It was found that the deformation mainly occurs in the out-of-plane direction, and that one third of the total strain from 25 °C to 380 °C occurs during the short crystallization temperature range (300–320 °C

at 1 °C/min). Finally, out-of-plane modulus development during solidification from melt was characterized via dynamic mechanical analysis. The modulus measured during cooling was very close to zero from the melt temperature until the start of crystallization, where it increased rapidly to ∼1.5 GPa. These thermomechanical properties will be employed in the next chapter to explain the mechanism responsible for defect formation during cooling. They will also be employed in Chapter 7 to develop and validate a pressure distribution model for DLF composites.

Chapter 5

Defect Formation during Processing

Moulding pressure during processing is needed not only to fill the mould cavity and compact the prepreg layers, but also to prevent the air entrapped in the part from growing into voids. During processing of thermoplastic composites, inconsistent part quality may arise if the consolidation pressure is lost before the complete solidification of the matrix during cooling. The objective of this chapter is to investigate defect formation during processing of carbon/PEEK composites. The chapter is divided in two main sections. First, the effect of moulding pressure on the quality of continuous fibre panels is studied. The quality of the panels is assessed by measuring their void content via optical microscopy. The effect of pressure is measured on four different mechanical properties. Second, an investigation of the moulding defects formed during compression moulding of DLF composites is presented. Thermal analyses are employed to understand the nature of the mechanisms responsible for their formation. An experimental method is developed to reproduce moulding defects and identify the temperature range during cooling at which they are formed. Finally, the effect of moulding defects on mechanical properties is quantified by comparing the compressive and flexural strength of specimens having different levels of moulding induced defects.

5.1 Effect of pressure on autoclave-processed panel quality

The objective of this section is to evaluate the effect of moulding pressure on the quality and mechanical properties of carbon/PEEK composites. Since compression moulding is performed using non-deformable tooling, non-uniform shrinkage during cooling can result in uneven pressure distribution applied to the part. This phenomenon makes it challenging to isolate the effect of compaction pressure on laminate quality. To get around this problem, autoclave manufacturing was selected. The use of a deformable bag in autoclave processing ensures that shrinkage does not affect the applied pressure. It can thus be assumed that at any time during the moulding process, the compaction pressure anywhere on an autoclave-processed panel is equal to the autoclave pressure. In the following sections, the effect of moulding pressure will be evaluated on the most simple composite part: flat unidirectional continuous fibre panels.

5.1.1 Autoclave panel manufacturing

Continuous fibre laminates were manufactured in an autoclave following the procedure described in Section 3.3.4. The panels were moulded using carbon/PEEK tape. Three different autoclave pressures were employed: 1.3, 3.0 and 5.0 bar (absolute). It should be pointed out that the three pressures tested are intentionally lower that the minimum of 7 bar recommended by the material supplier. Two thicknesses per pressure were moulded: 2.0 mm and 3.5 mm. The 2.0 mm thick panels were 305 mm × 165 mm, while the 3.5 mm thick panels were 406 mm × 165 mm. During layup of the 3.5 mm thick panel, a 60 mm long, 16 μm thick aluminum foil insert coated with Frekote 700-NC

release agent was place at the midplane to create a starter crack. This portion of the panel was used to perform mode I delamination tests.

5.1.2 Micrographs and void content

Void content analysis was performed on the 2 mm thick panels. Four 38 mm long cross-sectional samples were taken from each panel in order to measure their void content. The samples were taken 18 mm away from the 305 mm long edge of the panel. They were mounted with Buehler (Lake Bluff, IL) EpoThin 2 epoxy resin system and polished on a Metlab (Niagara Falls, ON) Forcipol 1V variable speed grinder/polisher equipped with a Forcimat automatic head. A five-step process polishing process was employed: 220 and 600 grit (piano diamond discs), followed by 1.2 wt% 12.5 μm, 0.75 wt% 5.0 μm, and 0.5 wt% 0.3 μm deagglomerated alumina suspension on a napless silk cloth.

A representative cross-sectional micrograph of each panel is presented in Fig. 5.1. In these figures, the PEEK matrix appears as dark gray, while carbon fibres are white. As depicted in Fig. 5.1a, a small number of voids were observed in the panel processed at 1.3 bar. They were agglomerated and appeared to be randomly distributed through the laminate. Nonetheless, the average void content was less than 0.05%. No porosity was observed in the panels moulded at 3 bar and 5 bar. Furthermore, all 1.3 bar and 3 bar samples had relatively smooth tool-side and bag-side surfaces, while a very rugged bag-side surface was observed on all samples taken from the panel moulded at 5 bar (Fig. 5.1c). The regular pattern at the surface indicates that this is fact the imprint of the fibreglass peel ply that was pressed onto the surface of the composite laminate under 5 bar of consolidation pressure.

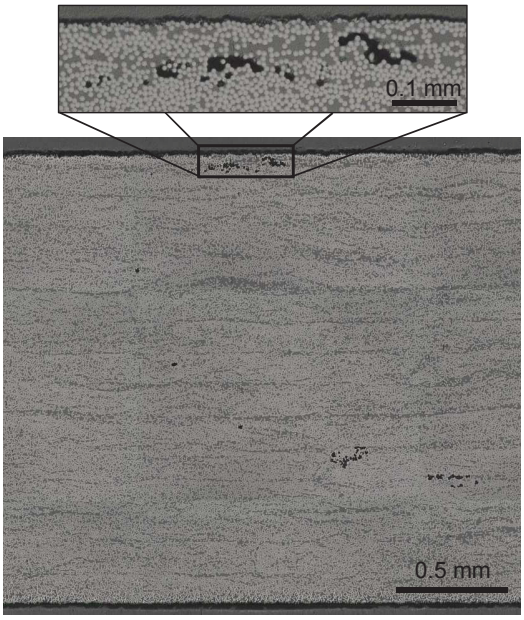

(a) **1.3 bar.**

(b) **3.0 bar.**

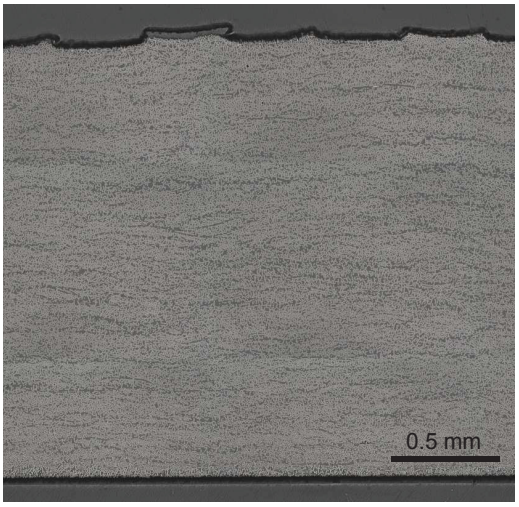

(c) **5.0 bar.**

Figure 5.1 – Cross-sectional micrograph of sample taken from unidirectional carbon/PEEK panels processed at three different pressures. The bag side of the panels is at the top of the micrographs.

From those results, it can be concluded that for the unidirectional tape studied, 1.3 bar of absolute pressure under vacuum conditions is sufficient to obtain a void-free laminate. This is due to the fact that the PEEK thermoplastic matrix is not tacky at room temperature, which allows the majority of the air between the layers to be evacuated by applying vacuum before processing. This is contrary to typical autoclave or out-of-autoclave processing of thermoset matrix based prepreg, where entrapped air needs to be removed prior to processing through a technique called debulking — applying vacuum for a certain period of time after new plies are added to the layup [73].

5.1.3 Mechanical testing

To assess the effect of pressure on the autoclave-processed panels, four mechanical properties commonly measured on unidirectional composite laminates were investigated. The tests and corresponding ASTM standards are listed in Table 5.1. Specimen dimensions and specifications are presented in Table 5.2.

Table 5.1 – Summary of the mechanical testing performed.

Layup	Thickness	Test	Standard
$[0°]_{15}$	2.0 mm	Tensile [0°]	ASTM D3039 [74]
$[0°]_{26}$	3.5 mm	Compression [0°]	ASTM D3410 [75]
		Interlaminar shear strength	ASTM D2344 [76]
		Mode I fracture toughness	ASTM D5528 [77]

The tensile strain was measured with an extensometer (gauge length of 50 mm), while Micro-measurements (Raleigh, NC) CEA-06-375UW-350 strain gauges were employed for compressive tests. In accordance with the ASTM

Table 5.2 – Specimen dimensions and specifications used for each mechanical test.

Test	Specimen dimensions
Tensile [0°]	250 mm × 12.7 mm × 2.0 mm 50 mm extensometer gauge length
Compression [0°]	150 mm × 12.7 mm × 3.5 mm 25 mm gauge length
Short-beam strength	25 mm × 7.0 mm × 3.5 mm
Mode I fracture toughness	150 mm × 20 mm × 3.5 mm 60 mm long, 16 μm thick aluminum foil insert

D3410 standard, all compressive tests were performed using the IITRI test fixture. The position of the delamination front during mode I delamination tests was monitored with a Dino-Lite (New Taipei City, Taiwan) AD7013MT portable travelling microscope. A thin layer of water-based typewriter correction fluid applied to the side of the specimen facilitated the monitoring. The crack length was measured using thin lines drawn on the side of the specimen at 5 mm intervals. Fig. 5.2 shows a sample image and the method employed to measure the crack length during the test.

The results for the stiffness of unidirectional carbon/PEEK laminates are summarized in Fig. 5.3. They were normalized with respect to the values obtained from the manufacturer's data sheet. The results show that the pressure had minimal effect on the tensile and compressive moduli. Moreover, all average values are very close to that reported in the material's data sheet. Tensile and compressive strength results are presented in Fig. 5.4. Although the tensile strength was on average 11% lower than the data sheet value, no improvement was observed with increasing pressure. This is an indication that optimal tensile

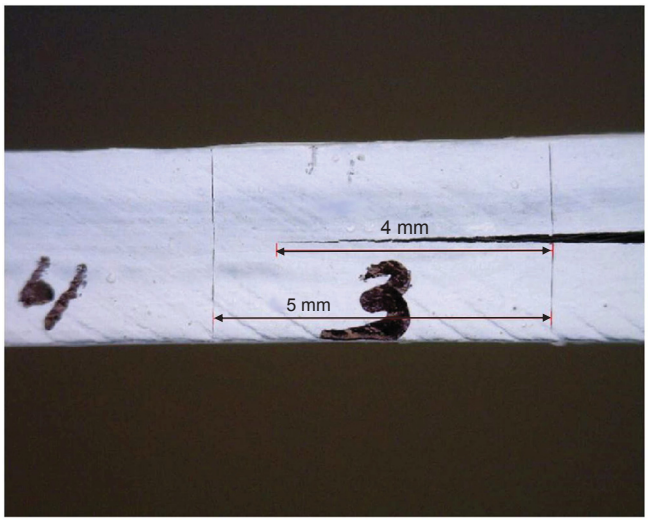

Figure 5.2 – Mode I fracture toughness crack length measurement.

properties can be obtained with a processing pressure as low as 1.3 bar. Khoun *et al.* [71] also reported similar tensile strength values for autoclave-processed panels manufactured with the same material at moulding pressures ranging from 6 bar to 10 bar. While similar compressive strength values (Fig. 5.4b) were obtained at 1.3 bar and 3 bar, an inconsistent result was obtained at 5 bar. Since it is probable that the strength reduction is not due porosity or fibre misalignment (visual inspection of the specimen), the premature failure was associated with the surface roughness located the bag side of the panel, as shown in Fig. 5.1c. The interlaminar shear strength (Fig. 5.5) was also not influenced by the moulding pressure. Moreover, all measured values were above the data sheet value, which was attributed to the fact that the interlaminar shear strength reported by the manufacturer is for a [0°/90°] layup.

The most interesting results were obtained from the mode I fracture toughness tests, Fig. 5.6. The histogram is showing three normalized mode I fracture toughness values: G_{Ic} measured directly from the aluminum insert, G_{Ic} obtained

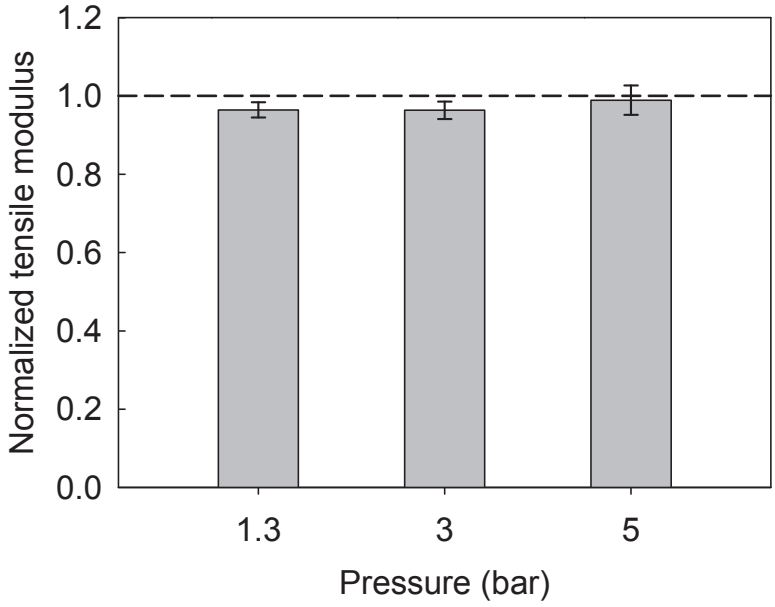

(a)

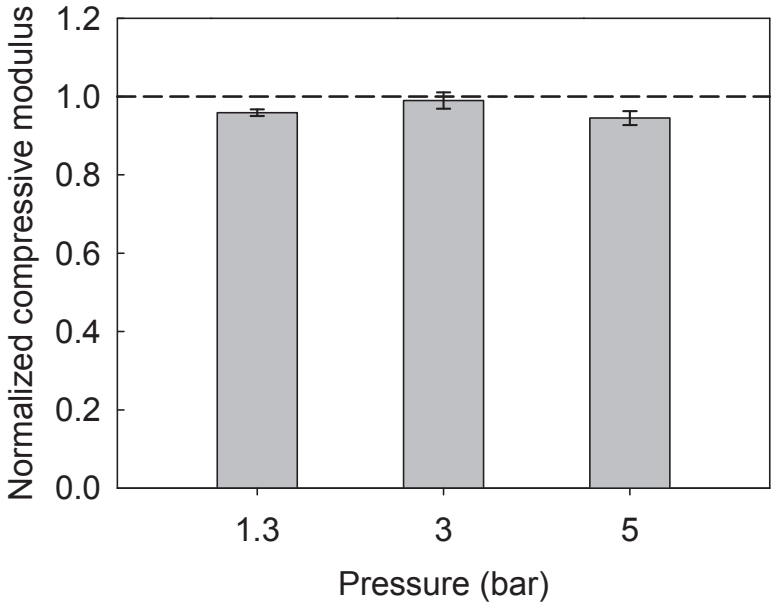

(b)

Figure 5.3 – Normalized stiffness of unidirectional carbon/PEEK laminates as a function of the applied moulding pressure. (a) Tensile modulus. (b) Compressive modulus. Error bars show one standard deviation. The data was normalized with respect to the values obtained from the manufacturer's data sheet.

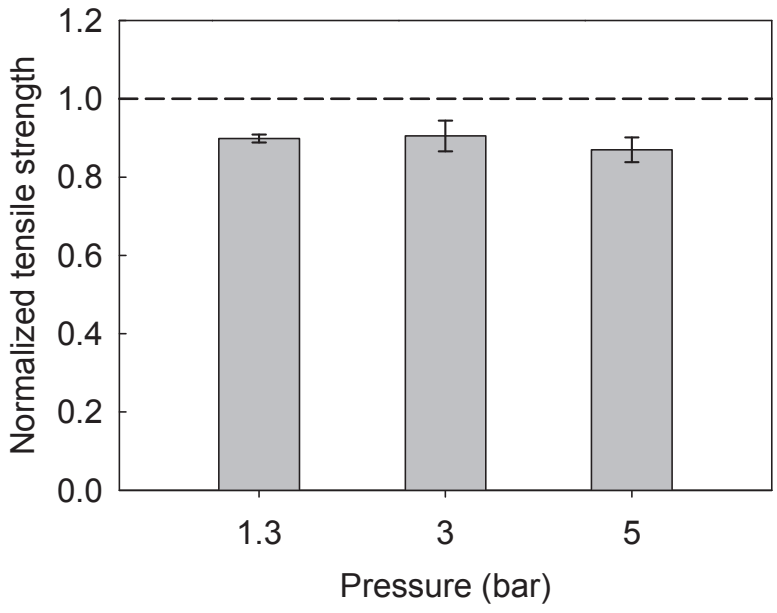

(a)

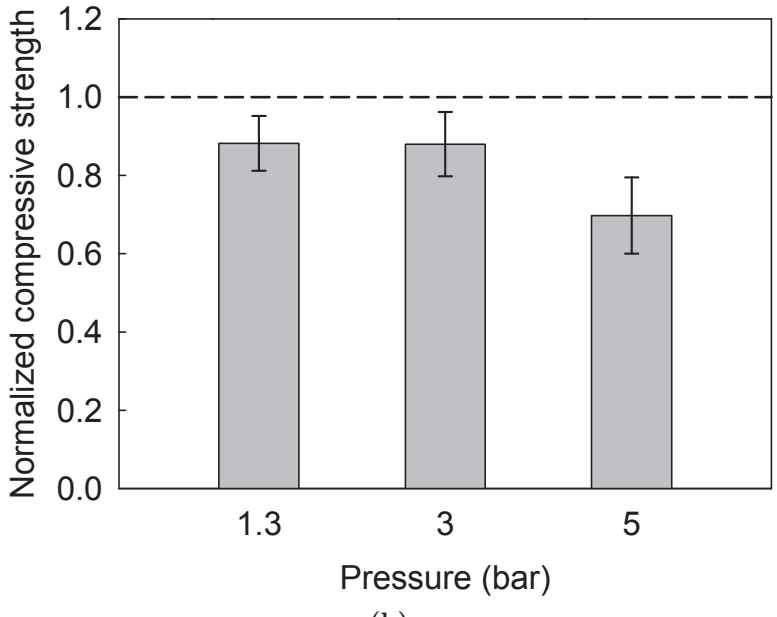

(b)

Figure 5.4 – Normalized strength of unidirectional carbon/PEEK laminates as a function of the applied moulding pressure. (a) Tensile strength. (b) Compressive strength. Error bars show one standard deviation. The data was normalized with respect to the values obtained from the manufacturer's data sheet.

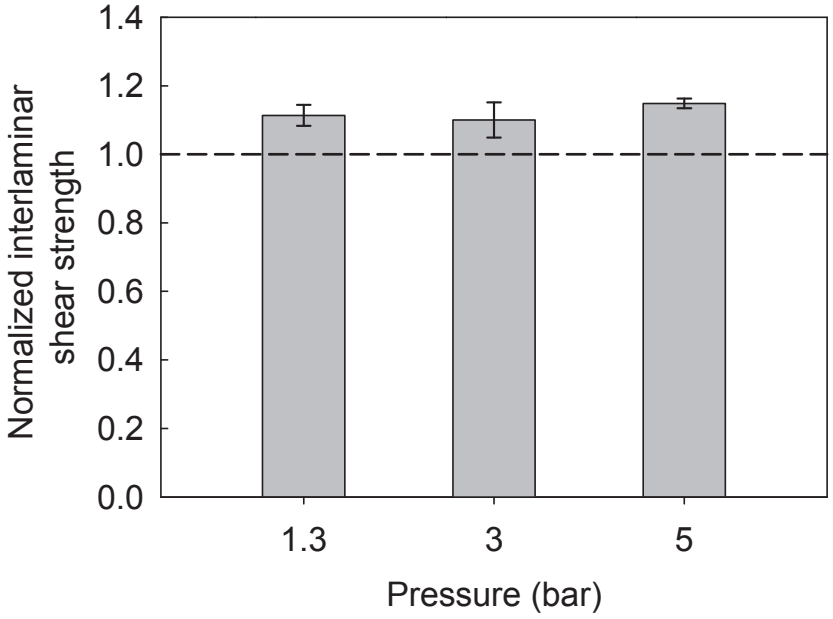

Figure 5.5 – Normalized interlaminar shear strength of unidirectional carbon/PEEK laminates as a function of the applied moulding pressure. The data was normalized with respect to the values obtained from the manufacturer's data sheet.

after performing a 3 mm to 5 mm precrack, and G_{IR}, the average fracture toughness measured during crack propagation. The data was normalized with respect to the highest average value. The mode I fracture toughness measured from a precrack was in the range of values reported in the literature for same combination of fibre and matrix materials [70,78–82]. While similar toughness properties were obtained between the 3 bar and 5 bar panels, those obtain with the 1.3 bar were much lower. In fact, all five 1.3 bar specimens experienced unstable delamination, as depicted in Fig. 5.7. Fibre bridging and double delamination paths, as shown in Fig. 5.8, were observed in most of the 1.3 bar specimens. This phenomenon is generally attributed to nesting of the fibres, weak fiber/matrix interfaces [83], or poor bonding of the prepreg layers [84]. These results show that the interlaminar properties of carbon/PEEK are more

sensitive to the applied moulding pressure than in-plane tensile and compressive properties, which are fibre-dominated.

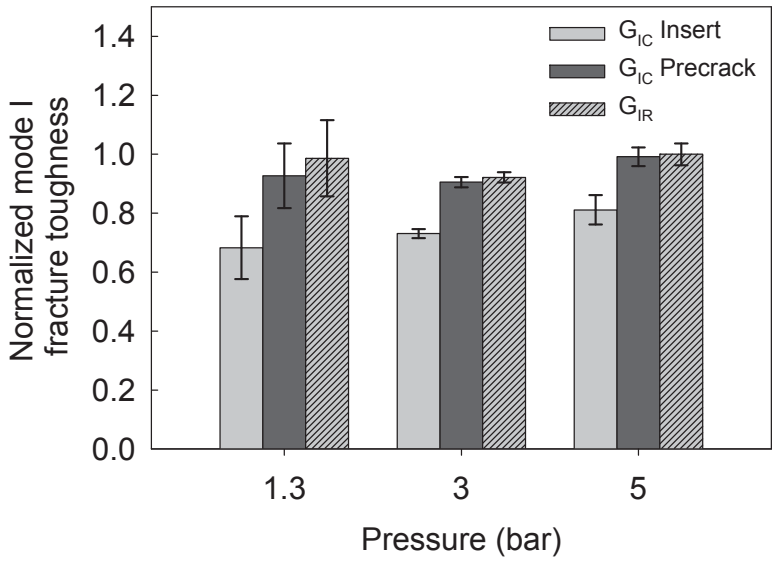

Figure 5.6 – Normalized mode I fracture toughness of unidirectional carbon/PEEK laminates as a function of the applied moulding pressure. The data was normalized with respect to the highest average value.

5.1.4 Summary

The effect of moulding pressure on the quality of autoclave-processed continuous fibre panels was assessed. All panels, including the one moulded under a pressure close to vacuum pressure, had very low porosity. Tensile, compressive, interlaminar, and fracture toughness properties were measured. The effect of pressure was negligible for all mechanical properties except the mode I fracture toughness, where the panel processed at 1.3 bar exhibited fibre bridging and double delamination paths. Based on these results, it was concluded that under the condition that air is properly evacuated during processing, a minimum moulding pressure of only 3 bar is required to obtain optimal mechanical prop-

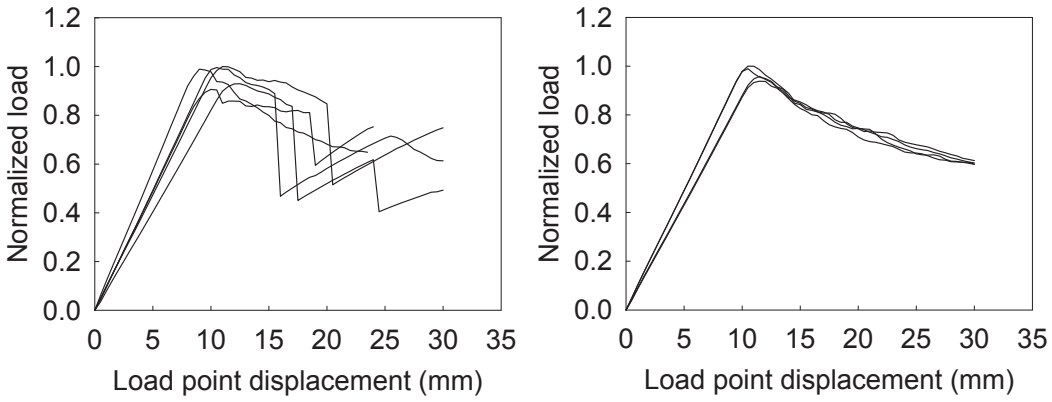

Figure 5.7 – Normalized load vs. load point displacement curves of unidirectional carbon/PEEK laminates measured during mode I delamination tests. (a) 1.3 bar specimens. (b) 5.0 bar specimens. The data was normalized with respect to the highest measured value.

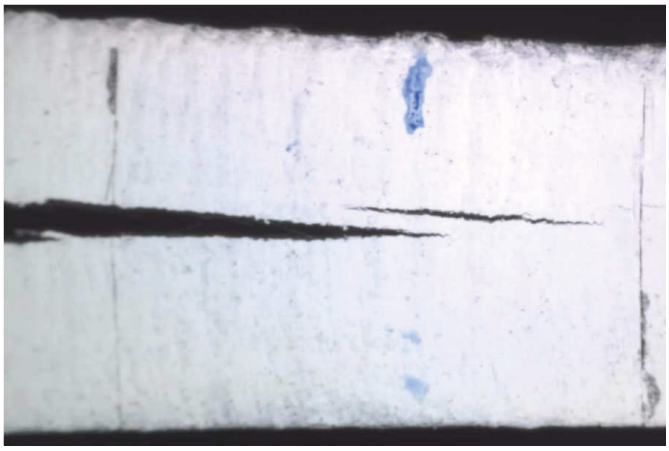

Figure 5.8 – Double delamination path observed in a mode I delamination specimen processed at 1.3 bar.

erties of carbon/PEEK laminates. In the next section, the consequences of failing to maintain the moulding pressure during compression moulding of DLF composites are investigated.

5.2 Defect formation during processing of DLF composites

The bulk factor of DLF thermoplastic composites reported by the manufacturer's data sheet is approximately 4–8 to 1. Since these materials are compression moulded, entrapped air is not removed by a vacuum operation, but is rather evacuated via the shear edges of the part, or crushed under pressure. This implies that voids might arise during compression moulding of DLF composites if entrapped air is not completely evacuated or maintained under pressure until complete solidification of the part. In this section, a link between thermal shrinkage, localized loss of pressure and void formation during processing of DLF composites is established.

5.2.1 Dynamic mechanical analysis

The TMA results obtained in the previous chapter showed the magnitude of the shrinkage rapidly occurring during crystallization. During processing, uneven shrinkage due to non-isothermal cooling is likely to cause localized loss of pressure, as depicted in Fig. 1.4. Since matrix tearing is commonly observed in regions where pressure was lost during cooling, a custom test was performed using DMA to investigate if a non-permanent bond between the mould platens and the material during processing could be responsible for this phenomenon. The experiments were performed on a TA Instruments Q800 Dynamic Mechanical Analyzer, equipped with a compression clamp 15 mm in diameter. The specimen (material and geometry) was the same as that used for the TMA tests (Section 4.2). The setup is shown in Fig. 5.9. Before each experiment, the surfaces of the compression clamp were coated with Frekote 700-NC release agent. The setup was heated to 380 °C at a rate of 10 °C/min

under a constant load of 0.1 N, followed by a 10 min temperature hold to ensure isothermal conditions. Afterwards, a compressive load of 0.3 bar was applied. This load was high enough to ensure a good contact between the specimen and the clamp, without inducing any flow of material at 380 °C. The setup was then brought to room temperature at a rate of 1 °C/min. This cooling rate was selected for the same reason stated in Section 4.2. During cooling, the distance between the two clamp surfaces was kept constant, while the load was recorded. A total of two specimens were tested in the out-of-plane direction.

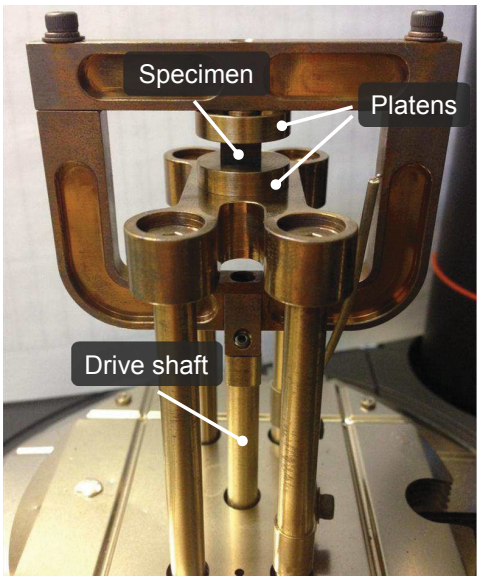

Figure 5.9 – Dynamic mechanical analysis test setup.

The dynamic mechanical analysis results are shown in Fig. 5.10. Although the applied pressure is not a direct representation of the real moulding process, the mechanism occurring during cooling and crystallization is clearly depicted in the results. From 380 °C to 355 °C, with a fixed distance between the clamp surfaces, the compressive load was reduced to zero due to the out-of-plane shrinkage in the material. Below 355 °C, a tensile load was developed in the

specimen, which is an indication that the material was sticking to the surface of the platens. Shortly after the start of crystallization at 326 °C, the rapid shrinkage resulted in a sharp increase in tensile load, until debonding occurred, at which point the load was quickly reduced to zero. The load reduction occurred at 318 °C and 316 °C for specimen 1 and specimen 2, respectively. This temperature corresponds to a relative crystallinity just above 5% for a cooling rate of 1 °C/min (see Fig. 4.4). Variability in the maximum pulling force recorded was also apparent from the test results, ranging from 1.2 to 2.1 bar for the two specimens tested. These results will be further discussed in Section 5.2.5.

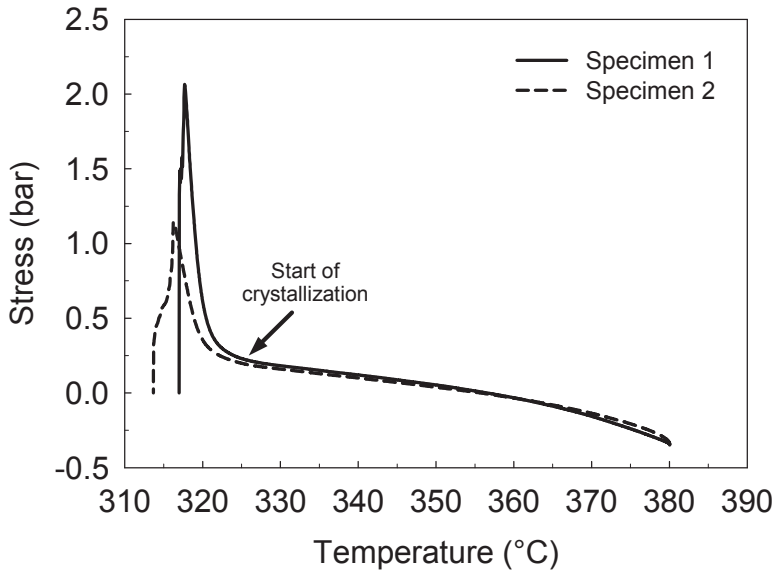

Figure 5.10 – Dynamic mechanical analysis results obtained on carbon/PEEK specimens. The initial compressive load was 0.3 bar and the cooling rate was 1 °C/min. The load drop occurred at 318 °C and 316 °C for specimen 1 and 2, respectively.

5.2.2 DLF composite panel manufacturing

Flat 100 mm × 100 mm DLF composite panels were moulded in an instrumented hot press using the procedure described in Section 3.3.1. A total of eight moulding conditions were tested, as summarized in Table 5.3. First, a void-free DLF composite panel was moulded under 10 bar of dwell pressure and 70 bar of cooling pressure (case A). A panel that had suffered localized loss of contact (as depicted in Fig. 1.4a) was moulded using dwell and cooling pressures of 70 bar and 10 bar, respectively (case B). The high dwell pressure was chosen to achieve a void-free condition before cooling, which ensured that all the moulding defects were the result of the loss of pressure during cooling. For comparison purposes, two continuous fibre panels with a stacking sequence of $[0/90]_{4S}$ were moulded using the above mentioned processing conditions, cases C and D. All panels were approximately 3.2 mm thick.

Table 5.3 – Summary of the processing conditions for each of the eight cases studied. All panels were heated to 380 °C at 10 bar and cooled at a rate of 10 °C/min.

Case	Material	Dwell pressure (bar)	Cooling pressure (bar)	Pressure release temperature (°C)
A	DLF	10	70	–
B	DLF	70	10	–
C	$[0/90]_{4S}$	10	70	–
D	$[0/90]_{4S}$	70	10	–
E	DLF	10	70	300 °C
F	DLF	10	70	310 °C
G	DLF	10	70	315 °C
H	DLF	10	70	320 °C

Another set of DLF composite panels was manufactured using a specific method that was developed to recreate the defects found in the panel moulded with case B. The results obtained with this method will help understand how and at which temperature during the cooling process the defects are formed. The same moulding conditions as the defect-free panel, case A, were utilized. However, in this method, the pressure was quickly released to 1 bar at a preselected temperature during the cooling stage. Four pressure release temperatures (PRT) were tested: 300, 310, 315, and 320 °C (cases E–H). They were selected based on the crystallization temperature range of carbon/PEEK measured by differential scanning calorimetry, as presented in Fig. 4.4. For a cooling rate of 10 °C/min, the temperature range tested corresponds to 0% relative crystallinity before the start of crystallization at 320 °C, to just over 20% relative crystallinity at 300 °C.

5.2.3 Temperature profile during cooling

The through-thickness temperature profile of the composite panel during cooling was approximated analytically. This was done to support whether or not a through-thickness temperature gradient is present, which might have an effect on the defect formation and distribution in the part. The through-thickness temperature distribution in a panel during cooling was solved using the equation of heat conduction in 1–D:

$$\frac{\partial^2 T}{\partial z^2} = \frac{1}{\alpha}\frac{\partial T}{\partial t}, \tag{5.1}$$

where

$$\alpha = \frac{k}{\rho c}. \tag{5.2}$$

The constant α is the thermal diffusivity of the material. For carbon/PEEK composite [85]:

$$\begin{aligned} k &= 0.72\,\mathrm{Wm^{-1}K^{-1}} \\ \rho c &= 2.2 \times 10^6\,\mathrm{Jm^{-3}K^{-1}}. \end{aligned} \tag{5.3}$$

The analytical solution of Eq. (5.1), for a panel of thickness $2h$, with an initial temperature T_i and both surface temperatures (at $z = \pm h$) following a cooling ramp r for $t > 0$, the temperature profile for $-h < z < h$, can be described by [86]:

$$\begin{aligned} T(z,t) = T_i + rt + \frac{r(z^2 - h^2)}{2\alpha} + \ldots \\ \frac{16rh^2}{\alpha\pi^3} \sum_{n=0}^{\infty} \frac{(-1)^n}{(2n+1)^3} \cos\frac{(2n+1)\pi z}{2h}\, e^{\left(\frac{-\alpha(2n+1)^2\pi^2 t}{4h^2}\right)}. \end{aligned} \tag{5.4}$$

When the Fourier number $\alpha t/h^2$ is greater than 1, the summation term can be neglected and Eq. (5.4) simply becomes

$$T(z,t) = T_i + rt + \frac{r(z^2 - h^2)}{2\alpha}. \tag{5.5}$$

The solution of Eq. (5.4) for the moulding parameters employed in Section 5.2.2, i.e. $T_i = 380$ °C and equal cooling rate of 10 °C/min ($r = -10$ °C/min) at both boundaries, is presented in Fig. 5.11 for three panel thicknesses. For a 3.2 mm thick panel, the temperature difference through-the-thickness is only 0.7 °C. However, the temperature difference becomes apparent for thicker panels. It should thus be pointed out that the results presented in the next sections could differ if the panels were much thicker than 3.2 mm.

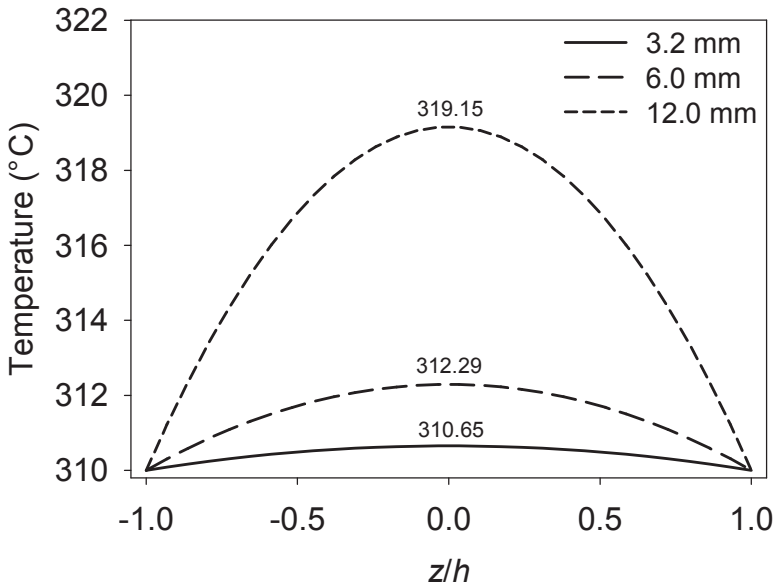

Figure 5.11 – Temperature distribution in a panel with T_i = 380 °C and equal cooling rate of 10 °C/min at both boundaries. Plots are for thicknesses $2h$ = 3.2 mm, 6 mm, and 12 mm. The temperature at the center of the panel is identified on each curve.

5.2.4 Analysis of moulding defects via optical microscopy

Defects formed during cooling were characterized using optical microscopy. Four 25 mm long cross-sectional samples were taken from each panel in order to identify the types of defects present and their location through-the-thickness. The samples were polished using the procedure described in Section 5.1.2. The total void content in each sample was measured with the help of image processing software by comparing the total area of the voids to the total area of the sample. Since a large number defects were observed near the surface of the samples, the surface porosity was defined as:

$$V_s = \frac{A_{\text{Void}}^{\text{Top}} + A_{\text{Void}}^{\text{Bottom}}}{L \cdot h} \tag{5.6}$$

where $A_{\text{Void}}^{\text{Top}}$ and $A_{\text{Void}}^{\text{Bottom}}$ are the void area in the top and bottom two layers, L is the sample length, and h is the sample thickness. Since the boundary between the second and third layer can be difficult to define due to the random placement of the strands and the possible change of thickness due to flow effects, a fixed distance from each surface equivalent to the nominal thickness of two prepreg layers was employed to measure the surface void content. Finally, the internal void content was defined as the difference between the total and surface void content.

Photos depicting the surface quality of DLF composite panels cooled at different pressures are presented in Fig. 5.12. The surface of the defect-free baseline panel cooled under 70 bar of pressure (Fig. 5.12a) was smooth, shiny, and black. Reducing the cooling pressure to 10 bar drastically influenced the surface quality of the panel (Fig. 5.12b), where surface defects caused by the loss of pressure during cooling were apparent. The affected regions were matte and rough to the touch. A closer inspection revealed evidence of matrix tearing at the surface. This observation and the DMA results (Section 5.2.1) show clear evidence of a separation between the material and the mould during cooling.

Cross-sectional micrographs of the two above mentioned panels are presented in Fig. 5.13. The baseline panel had minimal porosity (i.e. 0.05%) and a defect-free surface, as depicted in Fig. 5.13a. In contrast, the panel that has suffered loss of pressure during cooling had surface and internal porosity of 0.55% and 0.13%, respectively. The different types of defects observed in the latter are described in Fig. 5.14. In some instances, the voids located near the surface of the laminate were filled with mounting resin. For better visibility and void content measurements, these voids were colored black with the help of image processing software. Two types of surface defects were observed: surface roughness (Fig. 5.14a) and large voids concentrated at the surface (Fig. 5.14b).

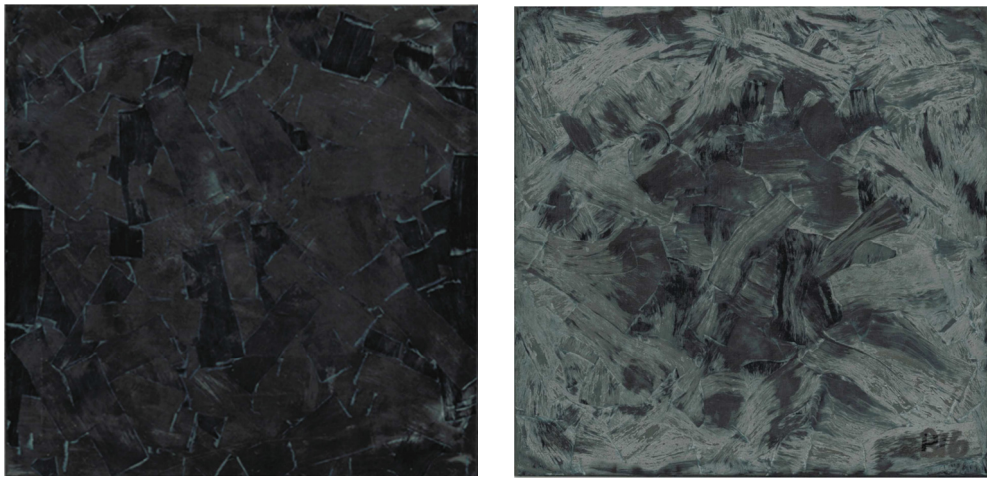

(a) (b)

Figure 5.12 – Surface quality of two DLF composite panels cooled at different pressures. (a) Defect-free panel cooled at 70 bar, case A. (b) Defect-induced panel cooled at 10 bar, case B.

The former is the result of the surface tearing during debonding between the material and the mould. Internal voids were most frequently located between strands (Fig. 5.14c), and in resin-rich areas formed at the intersection of multiple strands (Fig. 5.14d).

For comparison purposes, Fig. 5.15 shows micrographs of continuous fibre cross-ply laminates cooled at 70 bar and 10 bar, respectively (cases C and D). The samples were cut diagonally with respect to the longitudinal direction of the panel, exposing the fibers at $\pm 45°$. Similarly to DLF composite panels, the high pressure cooled laminate was defect-free, while defects similar to those shown in Figs. 5.14a,b,c were observed in the low pressure cooled continuous fibre laminate.

Table 5.4 summarizes the void content measurements for all DLF composite panels. From these results, it is apparent that visible surface defects (Fig. 5.12b)

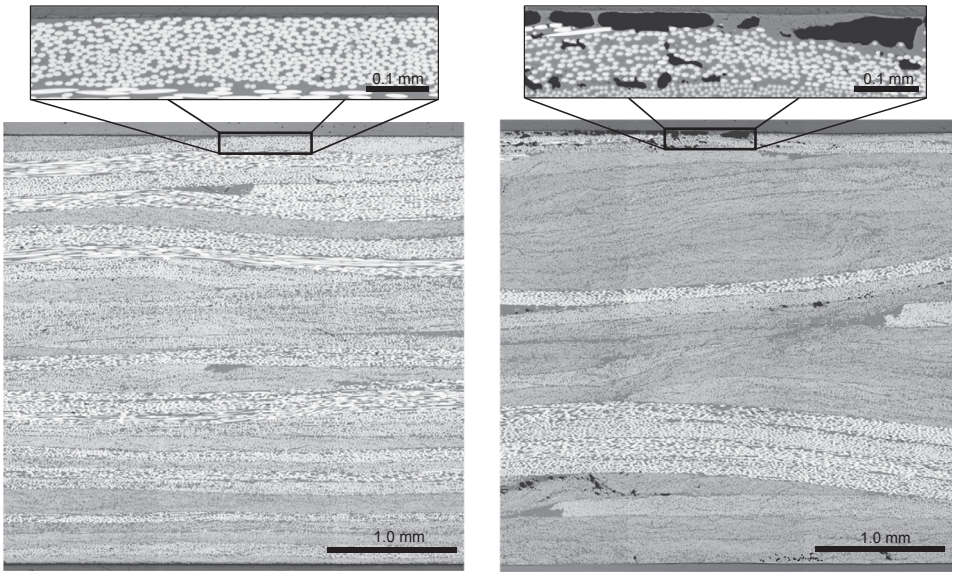

(a) (b)

Figure 5.13 – Representative cross-sectional micrographs of DLF composites cooled at different pressures. (a) 70 bar – Case A. (b) 10 bar – Case B.

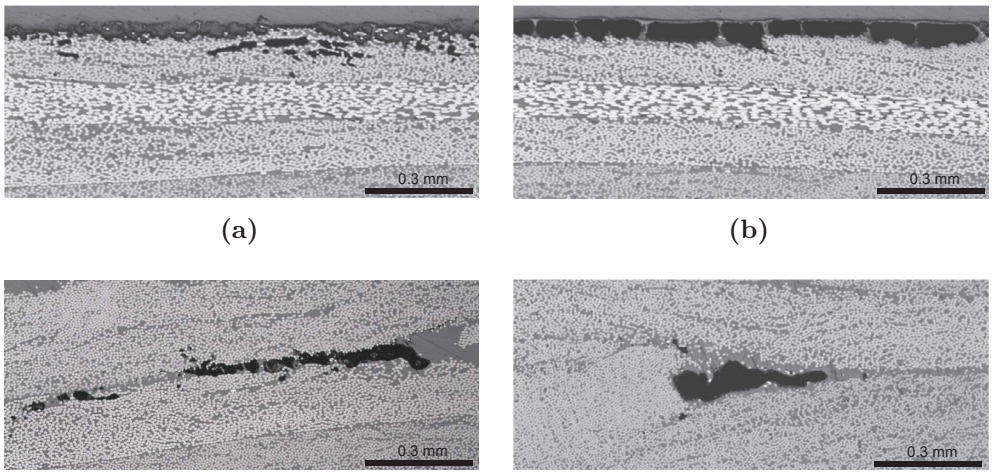

(a) (b)

(c) (d)

Figure 5.14 – Cross-sectional micrographs of DLF composites obtained at 50× depicting the different types of defects caused by the loss of pressure during cooling. (a) Surface roughness. (b) Voids agglomeration at the surface. (c) Interply voids. (d) Large void in resin-rich area. All micrographs were taken from the panel processed with case B.

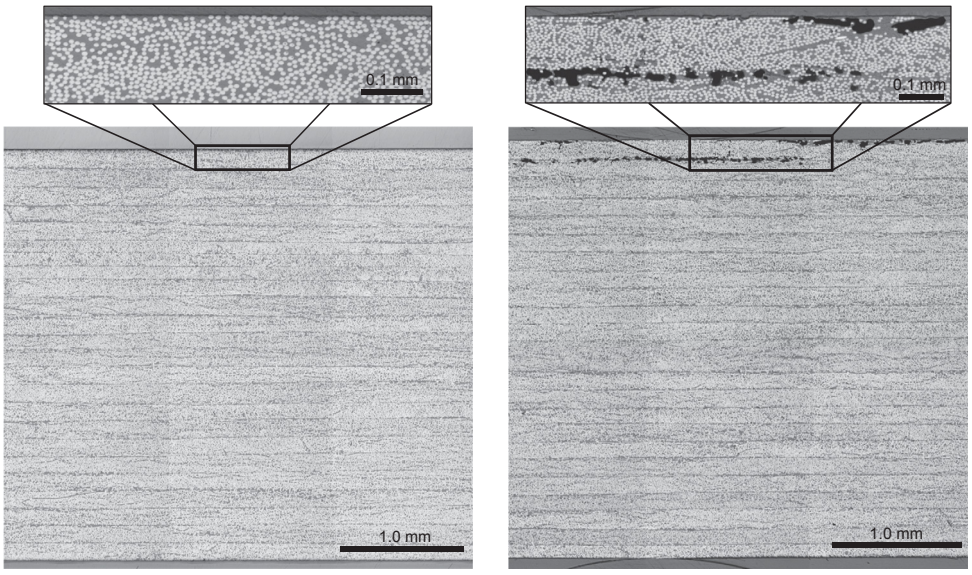

Figure 5.15 – Representative cross-sectional micrographs of continuous fibre laminates cooled at different pressures. (a) 70 bar – Case C. (b) 10 bar – Case D.

are an indication that surface and internal porosity are present in the material. A trend can also be observed with the types of defects formed as the PRT is increased. At 300 °C (case E), the panel is identical to the baseline (case A). With a 10 °C increase of the PRT, defects became visible at the surface of the panel and the average surface and internal porosity were 0.32% and 0.31%, respectively. With further increase of the PRT (case G), more surface defects were observed (0.42%), while the internal porosity was slightly lower than the previous case (0.24%). These porosity levels were the closest to those measured in the low pressure cooled panel (case B). Finally, case H resulted in the highest total void content of all DLF composite panels manufactured, 1.29%.

Table 5.4 – Summary of the void content measured on DLF composite panels moulded under different processing conditions. Values shown are mean ± one standard deviation. The mean value is the average of four samples.

Case	Visible surface defect?	Surface void content (%)	Internal void content (%)	Total void content (%)
A	No	0.00 ± 0.00	0.05 ± 0.01	0.05 ± 0.01
B	Yes	0.55 ± 0.15	0.13 ± 0.08	0.68 ± 0.12
E	No	0.00 ± 0.00	0.05 ± 0.02	0.05 ± 0.02
F	Yes	0.32 ± 0.04	0.31 ± 0.15	0.63 ± 0.12
G	Yes	0.42 ± 0.13	0.24 ± 0.09	0.65 ± 0.19
H	Yes	0.58 ± 0.11	0.71 ± 0.25	1.29 ± 0.32

5.2.5 Effect of shrinkage on void formation

Given the results presented in Sections 4.2, 5.2.1, and 5.2.4, a plausible explanation for the defect formation in DLF composite parts during cooling is described in the following. When the pressure during cooling is reduced to nearly zero, both surfaces of the material remain in contact with the mould platens and subsequent thermal shrinkage allows the air trapped in the part to form voids through-the-thickness of the part. During this process, the elastic modulus of the matrix will gradually develop due to the undergoing crystallization, until a point where the material will be able to resist the void formation. This hypothesis was validated by comparing the thermal shrinkage data in Fig. 4.6 with the measured void content reported in Table 5.4. For cases E–H, the total void content was plotted vs. the thermal shrinkage experienced by the part from the PRT to 300 °C, where only 0.05% porosity was measured. The results are presented in Fig. 5.16. A good agreement was obtained between the two entities. Moreover, the slope of the linear fit indicates that 57% of the out-of-plane

shrinkage was translated to void content. This behaviour is explained by the fact that the "bond" between the material and the press platens is presumably not perfect, and more importantly, not permanent (see Fig. 5.10).

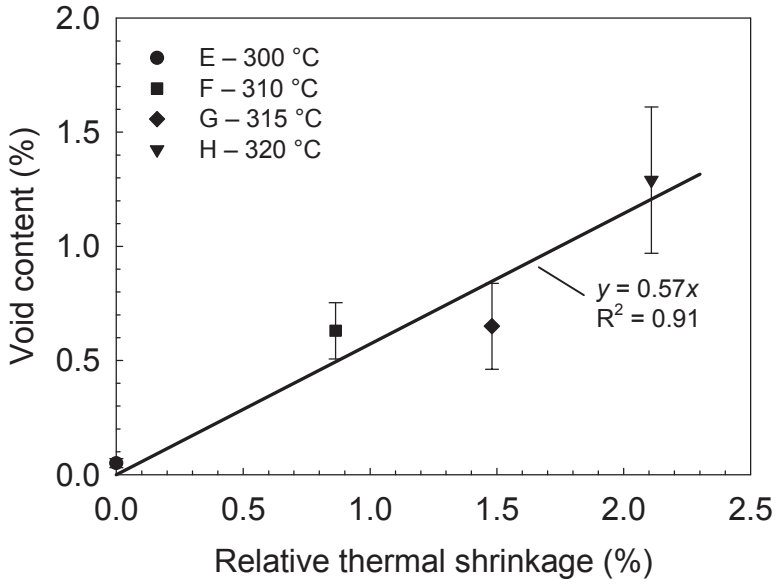

Figure 5.16 – Total void content vs. relative thermal shrinkage of carbon/PEEK panels. The legend refers to the cases and corresponding pressure release temperatures. Error bars show one standard deviation.

5.2.6 Mechanical testing

The effect of moulding defects on the mechanical performance of DLF composites was quantified by comparing the compressive and flexural strength of the panels moulded with the four different PRTs (cases E–H) with the void-free baseline (case A). Those mechanical properties were selected because they are generally known to be sensitive to porosity (see Section 2.4). The compression tests were performed in accordance with the ASTM D3410 standard [75]. Three 100 mm long, 25 mm wide, and 3.2 mm thick specimens were cut

from the center of each 100 mm × 100 mm panel, leaving 12.5 mm on each side to remove the region toward the mould edges where fibre alignment and distortion may occur. E-glass/epoxy end tabs were bonded to the specimens prior to testing using a cyanoacrylate-based adhesive, leaving a gauge length of 12.5 mm. All tests were performed using the IITRI compression test fixture installed on an MTS 250 kN load frame. Two repeats of each case were moulded, resulting in six specimens per case and a total of 30 specimens tested.

Flexural tests were performed in accordance with the ASTM D7264 standard [87]. The specimen geometry was the same as that employed for the compression tests. A four-point bend configuration was chosen, which results in a uniform flexural stress and no resultant vertical shear force between the central loading rollers. A span-to-thickness ratio of 20 was employed, with the distance between the loading noses set to one-half of the support span. The flexural strength of cases E, F, and H were compared with the void-free baseline, case A. All tests were performed on an MTS Insight 5 kN load frame. Two repeats of each case were moulded, resulting in six specimens per case and a total of 24 specimens tested.

The normalized compressive strength vs. total void content is presented in Fig. 5.17. The results were normalized with respect to the average strength obtained with the void-free baseline, case A. Fig. 5.17 shows that the compressive strength of the specimens with moulding defects (cases F–H) was reduced on the order of 15% to 25%. Moreover, the 95% confidence interval of cases F–H do not overlap that of the baseline, which confirms that despite the large scatter in the experimental data, the strength reductions are statistically significant. The results from cases F–H show on average a 26.7% reduction in the compressive strength per percent void. This value is considerably higher than the reduction of 4.5% per percent void reported in the literature for continuous

fibre carbon/epoxy unidirectional laminate [52]. This significant difference in void sensitivity is explained by the disparity in the load transfer mechanism of both materials: in DLF composites, the load is mainly transferred by shear stress at the interface between strands, while in continuous fibre laminates, most of the applied load is carried by the longitudinal fibres [42,44].

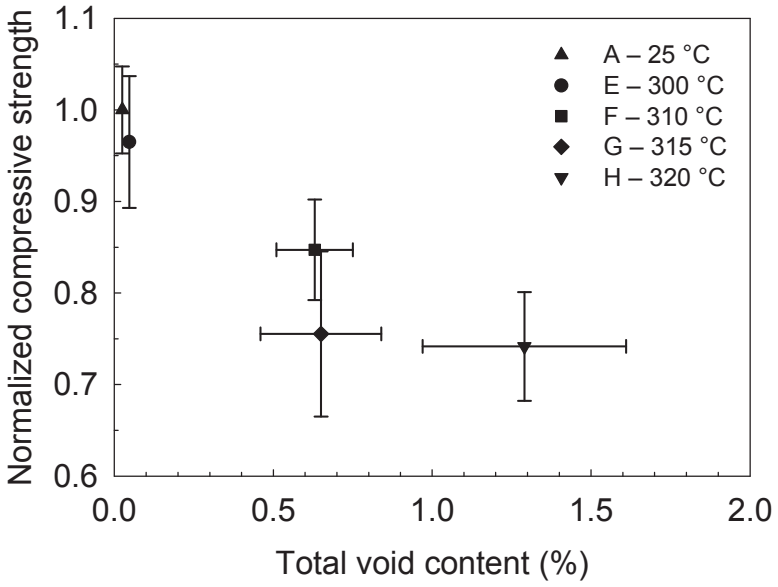

Figure 5.17 – Normalized compressive strength vs. total void content measured on DLF composite panels. The legend refers to the cases and corresponding pressure release temperatures. Error bars show one standard deviation. Data point for case E was offset for clarity.

The results shown in Fig. 5.17 also suggest that surface porosity is more detrimental to the compressive strength than internal porosity. First, case G has a similar total void content that case F, but has higher surface porosity and lower internal porosity that the latter, which lead to an additional decrease of 9.2% in compressive strength. In addition, case G and H have similar compressive strength, although case H has three times the internal void content of the former. This argument is further supported in Fig. 5.18, where good agreement

was found between the normalized compressive strength and the surface void content. These results suggest that failure was initiated at the surface of the specimen, and that internal porosity did not play a big role in reducing the compressive strength of the material. This is in agreement with the behaviour of HexMC^{TM} DLF composites reported by Boursier and Lopez [41], where under tensile loading, first cracks mainly occurred at the surface of the specimens. It it thus concluded that premature failure due to localized stress concentrations associated with very high porosity and defects agglomeration at the surface of the specimens (see Fig. 5.14a,b) is the cause of this behaviour [88]. However, no definitive change in the failure modes with strength reduction was observed, as most specimens failed in a brush-like manner, with longitudinal splitting between strands, as shown in Fig. 5.19. Fibre failure and strand debonding at the surface were also commonly observed, but could not be specifically associated with any particular case. It should also be pointed that nearly all compressive specimens failed abruptly shortly after an acute crack sound was heard.

Lastly, the result from case E demonstrated that the release of pressure below 300 °C during cooling ($X_{vc} \sim 20\%$) has no effect on the compressive strength of DLF composites. A Student's t-test ($\alpha = 0.05$) confirmed that the value obtained for case E is not statistically different than the baseline ($P = 0.477$). This finding suggests the possibility of demoulding parts at high temperature, which would greatly reduce moulding time, although potentially inducing dimensional instability such as warpage or springback.

The failure behaviour of flexural specimens was very different than that of compressive specimens, as nearly all specimens experienced a load drop occurring generally between 70% to 90% of the ultimate strength. The load drop was accompanied by an audible sound and visual damage on the surface

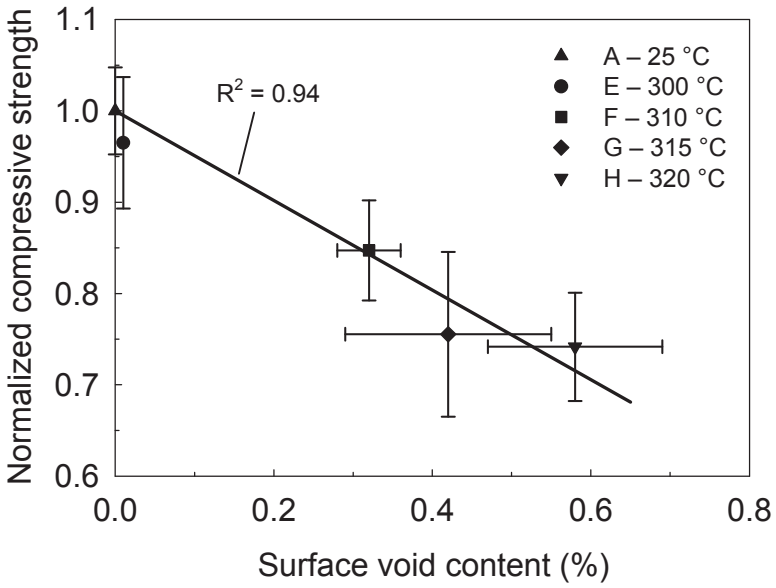

Figure 5.18 – Normalized compressive strength vs. surface void content measured on DLF composite panels. The legend refers to the cases and corresponding pressure release temperatures. Error bars show one standard deviation. Data point for case E was offset for clarity.

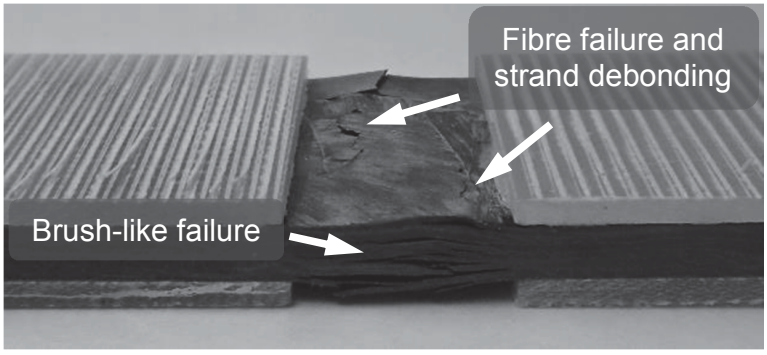

Figure 5.19 – Compression test specimen showing through-the-thickness brush-like failure, as well as fibre failure and strand debonding at the surface.

of the specimen. Visual observation of first cracks showed that they always occur at the surface, which is in accordance with the fact that the maximum flexural stress is located outer surfaces of the specimen. The first cracks were observed 72% of the time on the compressive side of the specimen, 22% on the tensile side and 6% on both. A representative photograph of a failed specimen is presented in Fig. 5.20. Failure on the compressive side were most often oriented perpendicular to the length of the specimen. On the tensile side, they were mainly located in the resin-rich interface between surface strands. It should also be pointed that in 56% of the specimens tested, the first cracks occurred at or very near the edge of the specimen.

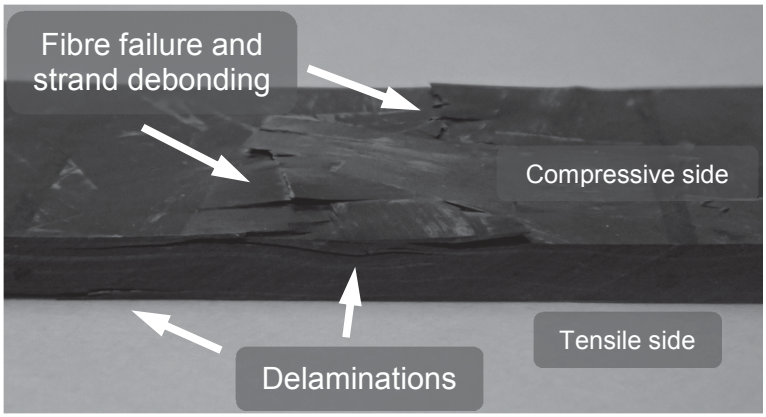

Figure 5.20 – Flexural test specimen showing delamination on the edges, as well as fibre failure and strand debonding at the surface.

A representative flexural stress–strain curve of each case showing abrupt load drop associated with premature failure is presented in Fig. 5.21. The four curves show clear evidence of a stiffness reduction after the first failure. Therefore, in addition to the ultimate flexural strength, a second parameter taking into account this first failure was introduced. This parameter was defined as the 5% offset/maximum stress (5%/Max), calculated by finding the intersection of the

stress–strain curve with a line drawn from the origin and offset by a 5% increase in compliance from the original linear region of the curve. If the intersection occurs after the ultimate flexural strength, the latter was used to calculate this value. The method is shown graphically in Fig. 5.22.

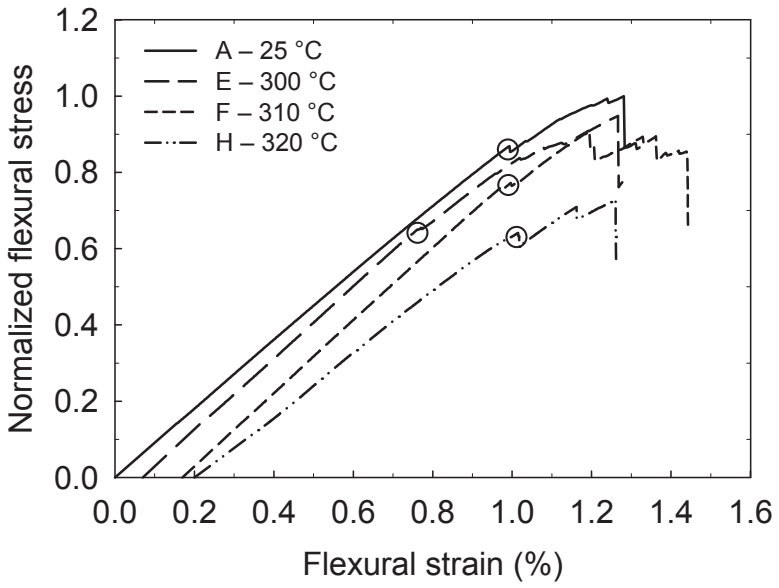

Figure 5.21 – Representative flexural stress–strain curves of DLF composites showing the abrupt load drop associated with premature failure before reaching the ultimate strength.

Both normalized flexural strength and 5%/Max stress vs. total void content are presented in Fig. 5.23. The results were normalized with respect to the average strength obtained with the void-free baseline, case A. The ultimate flexural strength (Fig. 5.23a) of cases F and H was reduced by 12% and 15%, respectively. The strength reductions are also statistically significant (95% confidence intervals). The average reduction in ultimate flexural strength of 14.9% per percent void is much larger than the 1.5% for each 1% of voids reported for unidirectional glass fibre composites [57]. A similar trend was observed with 5%/Max stress values, where it was 10% and 26% lower than

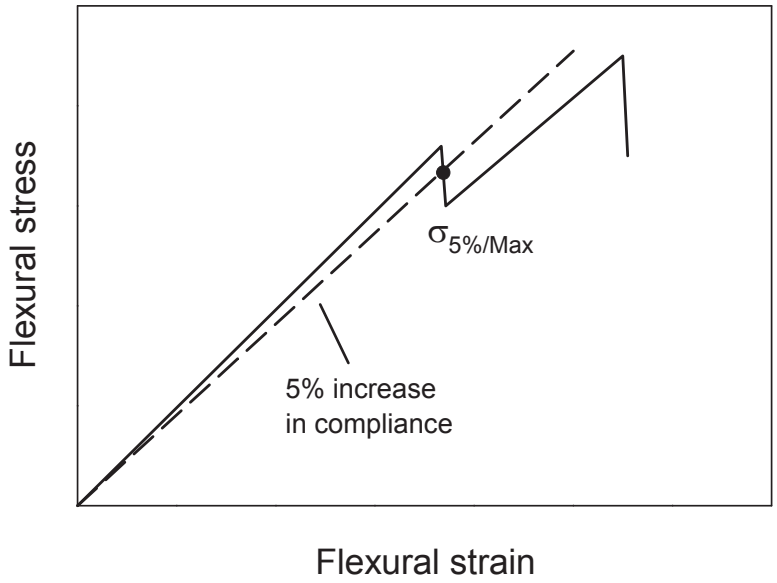

Figure 5.22 – Schematic showing the 5%/Max method employed to estimate the flexural strength.

the baseline for cases F and H, respectively. The reduction was statistically significant for case H (95% confidence intervals), but not for case F, due to the high variability in the data set.

Unexpectedly, both the ultimate flexural strength and 5%/Max stress values for case E (PRT = 300 °C) were higher than the baseline (4% and 8%), although a Student's t-test ($\alpha = 0.05$) revealed the differences were not statistically significant ($P = 0.111$ and $P = 0.418$). This adds further confidence that the release of pressure below 300 °C during cooling has no significant effect on the mechanical properties of DLF composites. For sake of completeness, the flexural test results are plotted vs. the surface void content in Fig. 5.24. Overall, very good correlations were found between flexural properties, surface void content, and void content, with coefficients of determination ranging between 0.89 and 0.95 (Figs 5.23 and 5.24).

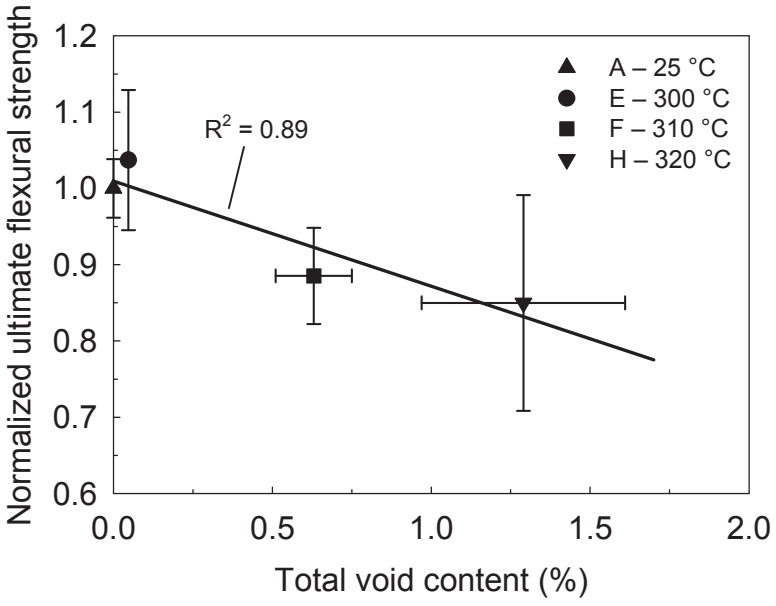

(a)

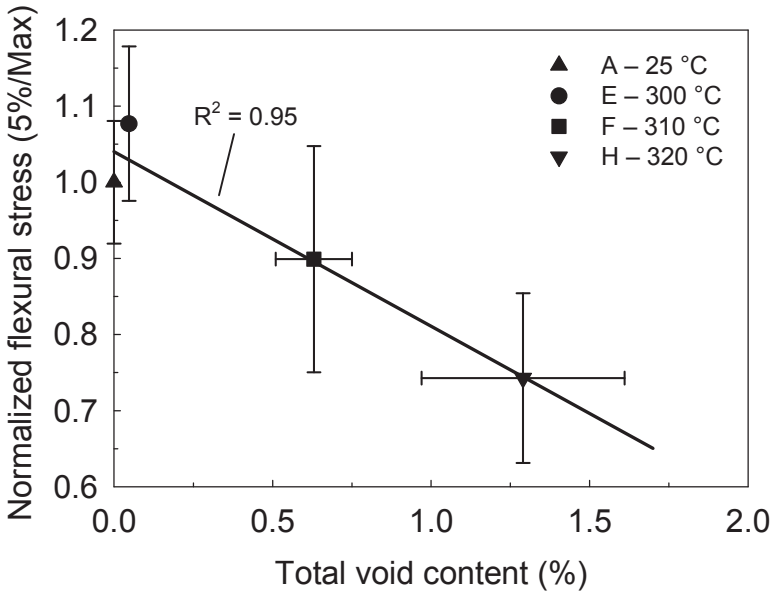

(b)

Figure 5.23 – Normalized (a) ultimate flexural strength and (b) 5%/Max flexural stress vs. total void content measured on DLF composite panels. The legend refers to the cases and corresponding pressure release temperatures. Error bars show one standard deviation. Data point for case E was offset for clarity.

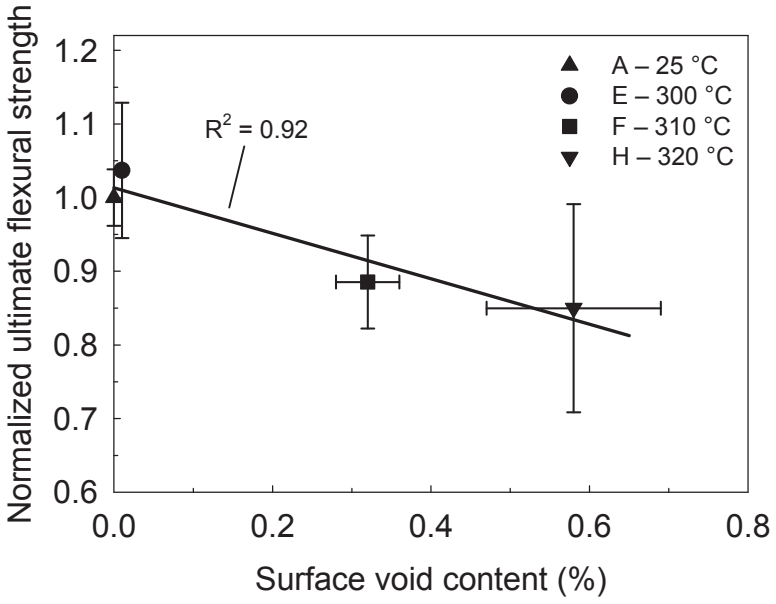

(a)

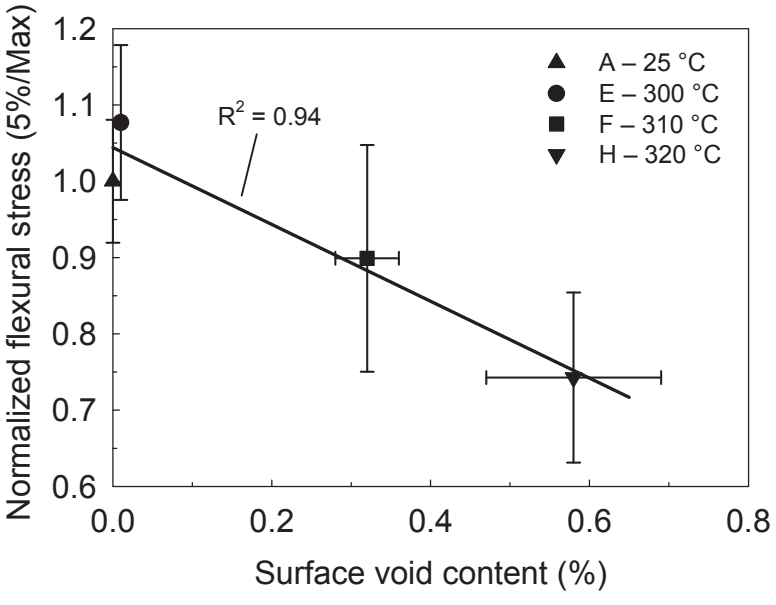

(b)

Figure 5.24 – Normalized (a) ultimate flexural strength and (b) 5%/Max flexural stress vs. surface void content measured on DLF composite panels. The legend refers to the cases and corresponding pressure release temperatures. Error bars show one standard deviation. Data point for case E was offset for clarity.

To investigate if there is a correlation between the stress when the first audible crack occurs and the ultimate stress of the specimens, the ultimate flexural strength was plotted vs. the first failure stress, as shown in Fig. 5.25. Each axis was normalized with respect to highest measured value. Despite the low coefficient of determination measured between the two entities, a trend can clearly be observed. Apart from a few outliers, especially from the data obtained with case H, a lower first failure stress will likely result in a lower specimen ultimate strength. This finding is also supported by the fact that in 74% of the specimens tested, the ultimate failure was located where the first failure was observed. This is contrary to the result found by Boursier and Lopez [41] on coupons manufactured from carbon/epoxy HexMC® DLF composites, where no correlation was found ($R^2 = 0.07$) between the ultimate tensile strength and the first failure stress.

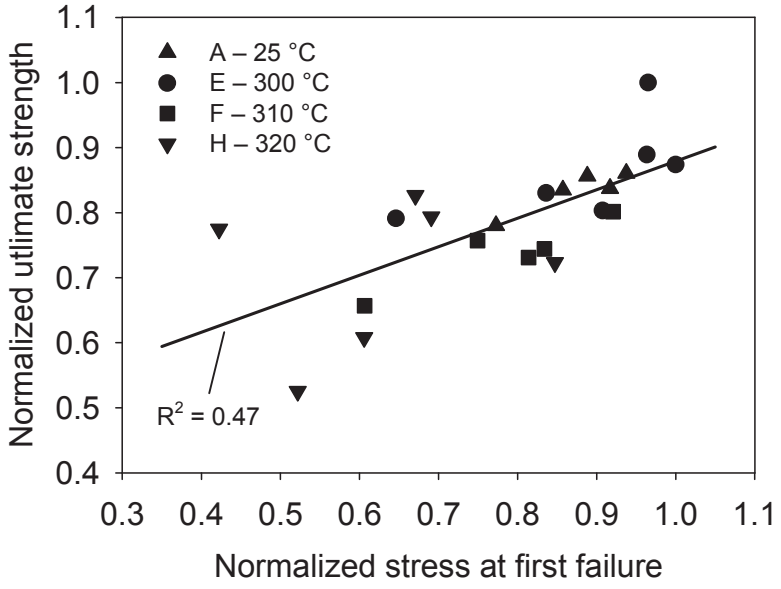

Figure 5.25 – Correlation between the ultimate flexural strength and the first failure stress of DLF composites. The legend refers to the cases and corresponding pressure release temperatures.

5.2.7 Summary

An investigation of defect formation during the cooling stage of DLF composite processing was presented. The high out-of-plane coefficient of thermal expansion of the material at the onset of crystallization was deemed responsible for this behaviour, as it leads to non-uniform shrinkage when a part is cooled unevenly. Loss of contact between the material and the tooling surfaces due to thermal shrinkage was observed with the help of dynamic mechanical analysis, where tensile load was measured on the specimen before disbond.

Flat DLF composite panels with void content ranging from 0% to 1.4% were moulded using an instrumented hot press by releasing the compaction pressure at temperatures ranging from 300–320 °C during cooling. Void content analysis showed a clear correlation between visible surface defect and porosity. Defects such as voids at the surface, in resin-rich regions and between strands were identified. The compressive strength of the specimens with moulding defects was reduced significantly, on the order of 15–25% for total void content of 0.65–1.3%. The flexural properties were reduced by 10-25% for the same range of void content. It was also found that the surface porosity was more detrimental to the mechanical properties than internal porosity. The sensitivity of the compressive and flexural properties to voids observed in this study was much larger than what is commonly reported for conventional continuous fibre composites, which indicates that design allowables normally considered for the latter might not be applicable to DLF composites. On the other hand, it was found that high moulding pressure was not required below 300 °C in order to obtain a defect-free panel having pristine mechanical properties. This demonstrates that parts could possibly be ejected at high temperature, greatly reducing the processing time of DLF composites.

The results from this chapter will be employed in conjunction with a thermomechanical model capable of predicting the pressure distribution on the part during processing. Using the material's thermomechanical properties (Chapter 4) and the critical temperature below which no manufacturing defects are formed, problematic areas where potential defect formation might occur will be predicted. The model is presented in Chapter 7.

Chapter 6

Case Studies

6.1 High pressure moulding of a complex-shaped DLF composite part

During cooling of a flat panel, most of the applied load will be taken by the region which has experienced the least amount of shrinkage (see Fig. 1.4). This will generally be the hotter region of the part, which also has the lowest modulus. An increase of the moulding pressure should result in higher strain in that section, directly reducing the amount of defects formed in the cold region of the part. This will be further discussed in Chapter 7. In a complex region, another key parameter comes into play: the order in which each component is solidified during cooling. For example, in a simple T-shape configuration comprised of a rib and a flange, it is important that the rib is cooled first, which ensures that the soft flange can properly transfer the moulding pressure on the rib component. In the event where the flange would cool faster than the rib, the rapid increase of the out-of-plane modulus of the flange during solidification (Fig. 4.10) will suppress all compaction on the rib, which will lead to defect formation. This suggests that higher moulding pressure might not directly relate to defect reduction in complex-shaped components. The objective of this case study is to investigate the role of the moulding pressure and cooling strategy on

the reduction of defects formed in a complex-shape DLF composite part. The chosen geometry is one the most difficult part to form by compression moulding: an L-bracket with a rib feature (Fig. 3.9).

6.1.1 Methodology

Following the procedure described in Section 3.3.3, L-brackets were manufactured using 13 mm × 3.2 mm DLF strands. Two moulding parameters were investigated following a two-factor, two-level design of experiments. First, the moulding pressure was varied between 100 and 200 bar. They correspond to moulding forces of 133 kN and 266 kN, respectively, based on the projected area of the mould, 0.013 m^2. Second, the mould was cooled using two different methods. The first method consists of applying the compressed air in all cooling channels simultaneously. Since the cooling channels on the bottom section of the tool are much closer to the part than the ones situated in the punch (see Fig. 3.7), this method will lead to a solidification of the flange before the rib. The second cooling method was performed by first cooling the top section of the mould to 345 °C before applying cooling to the bottom, thus solidifying the rib first. The nominal moulding cycles of each method is presented in Fig. 6.1. Two other L-brackets were moulded to investigate the effect of the debulk cycle (see section 3.3.3). The test matrix is summarized in Table 6.1. One L-bracket per condition was moulded.

The rib component of the DLF composite L-brackets moulded with cases I–L were cut into five sections, as shown schematically in Fig. 6.2. A micro-CT scan was performed on the middle section, while micrographs were taken on the four remaining sections. Void content was measured via the two methods.

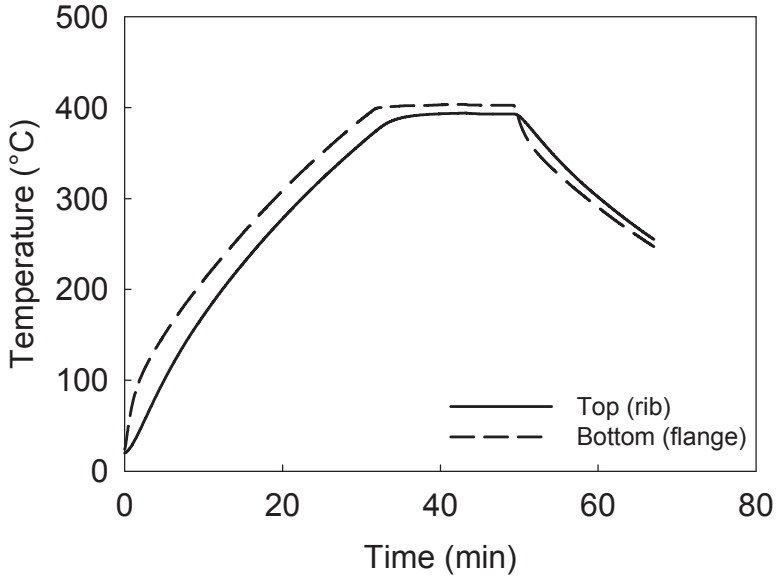

(a)

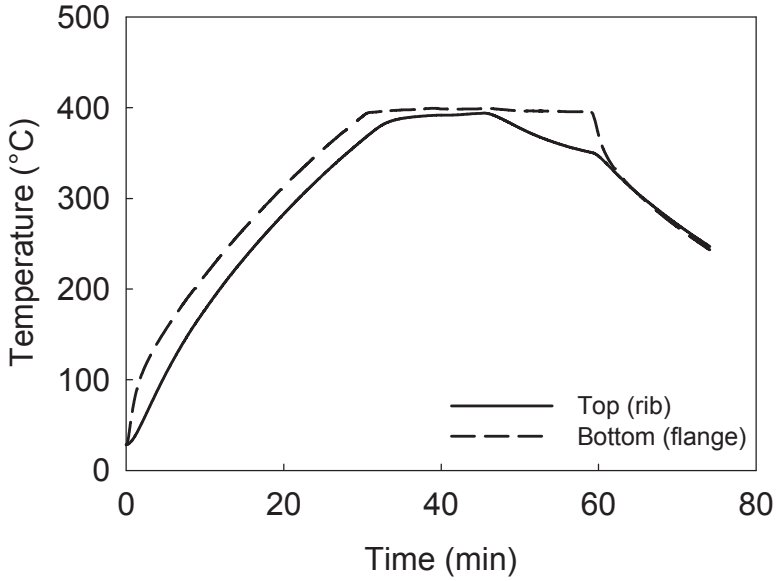

(b)

Figure 6.1 – Nominal moulding cycle of DLF composite L-brackets. (a) Cooling method 1 – Flange cooled first. (b) Cooling method 2 – Rib cooled first.

Table 6.1 – Test matrix employed for the moulding of DLF composite L-brackets.

Case	Pressure (bar)	Cooling method	Debulk cycle?
I	100	1	Yes
J	100	2	Yes
K	200	1	Yes
L	200	2	Yes
M	100	1	No
N	200	1	No

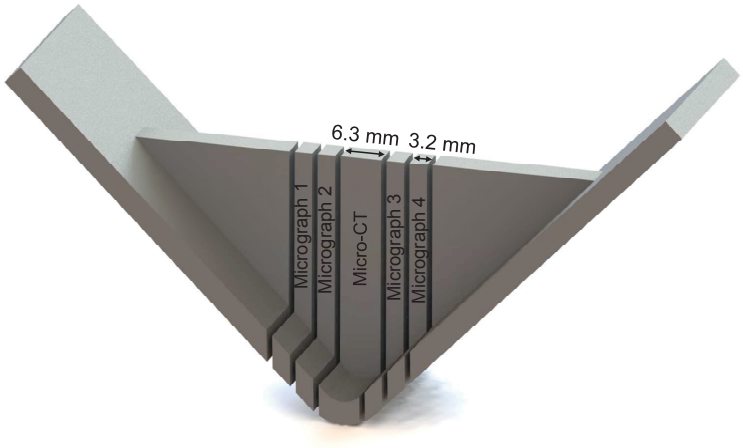

Figure 6.2 – The rib section of the DLF composite L-bracket part cut into five samples. The dimensions of the flange are not representative of the real part.

6.1.2 DLF composite rib surface quality

The surface quality of the rib component moulded with cases I–L are shown in Fig. 6.3. The bracket moulded at low pressure and cooled with method 1 (case I) had the larger amount of surface defects. Both the increase of moulding pressure and change in the cooling strategy are shown to decrease the amount of surface defects. However, a direct comparison between cases I, J, and K shows that the cooling strategy (method 2) had a larger impact than the increase of

the moulding pressure from 100 bar to 200 bar. Moreover, both improvements were required to obtain a defect-free surface, as depicted in Fig. 6.3d (case L). Lastly, it should also be pointed that for all four cases, the L-shape flange was free of surface defects.

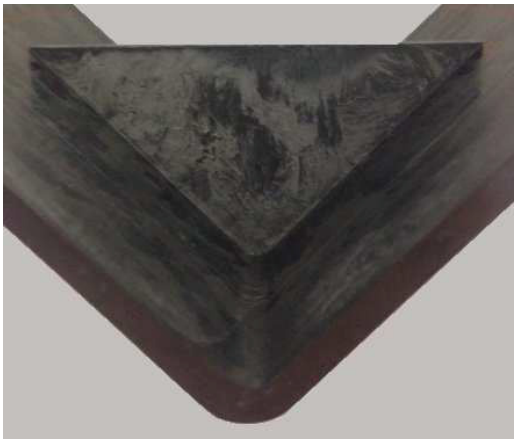

(a) Case I – 100 bar, method 1.

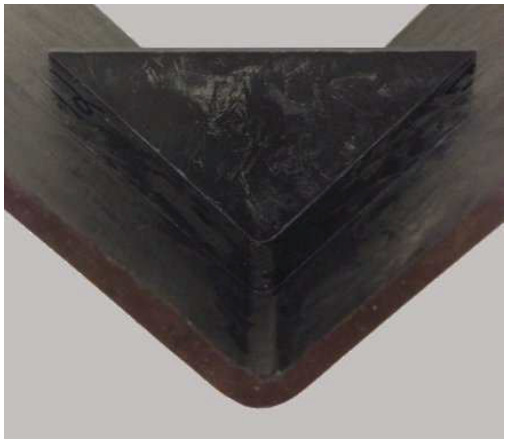

(b) Case J – 100 bar, method 2.

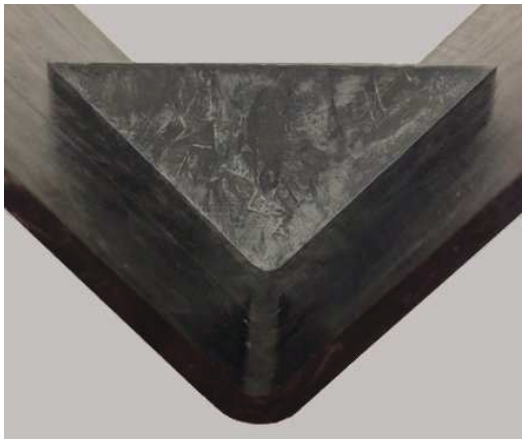

(c) Case K – 200 bar, method 1.

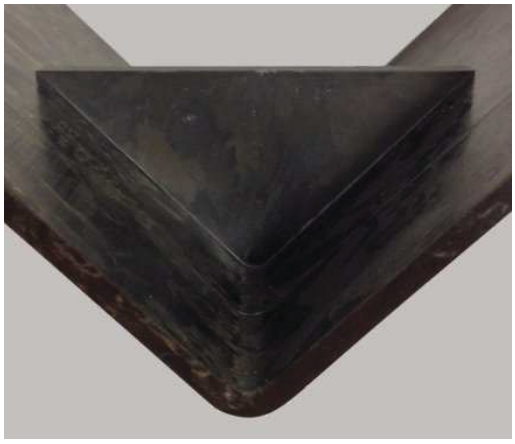

(d) Case L – 200 bar, method 2.

Figure 6.3 – Surface quality of L-bracket rib sections. The caption refers to the cases, corresponding moulding pressures and cooling methods.

6.1.3 Optical microscopy of L-bracket rib sections

The four rib section per case were polished using the methodology described in Section 5.1.2. Two sections of the rib were considered, the base and the tip, as shown in Fig. 6.4. The base section corresponds to the region of the rib were the micro-CT scan was performed. It will be used to directly compare the void content measured by the two methods.

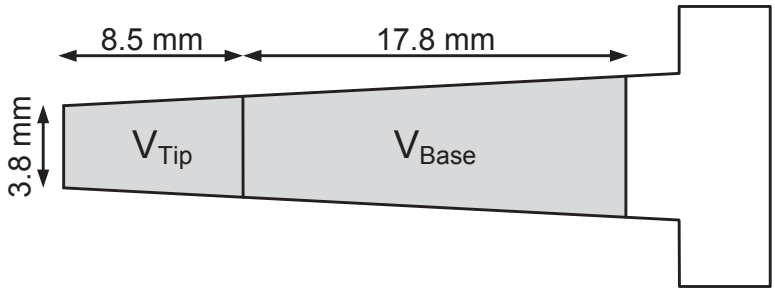

Figure 6.4 – Definition of the areas corresponding to the tip and the base of the rib section.

Representative cross-sectional micrographs of the tip of the rib sections are presented in Fig. 6.5. Very high porosity was measured in the sample processed with case I (2.1%). Detailed micrographs of sections near the tip and at the surface of the sample are shown in Fig. 6.6. All four main types of defects found in flat panels (see section 5.2.4) were present, with a large number of them located near the surface. The apparent disparity between the results obtained with moulding cases I and J (Fig. 6.5a,b) give some additional information on the void formation mechanism during processing of DLF composites. Since both part were processed at the same moulding pressure, it can be assumed that had identical morphology after the processing dwell. The cooling strategy alone is thus responsible for the void content difference of 1.5% (–73%) observed between

the two cases. A different void morphology was also observed in case J, where they were mainly located in interply regions, away from the surfaces. Case K showed that higher moulding pressure lead to a 61% reduction in void content. The type of voids observed were similar to those found in case I. Finally, very little porosity was observed in the sample moulded with case L; small voids were found between plies, and no porosity was observed near the surface, which is in accordance with the defect-free surface visually observed on the part (Fig. 6.3d). The void content measured at the tip of the rib sections are summarized in Fig. 6.7. The two lowest average void contents were obtained with cases J and L, both cooled with method 2. Similar void content was measured in case K, although the standard deviation was almost double that of case L (values varied from 0.33% to 1.57%).

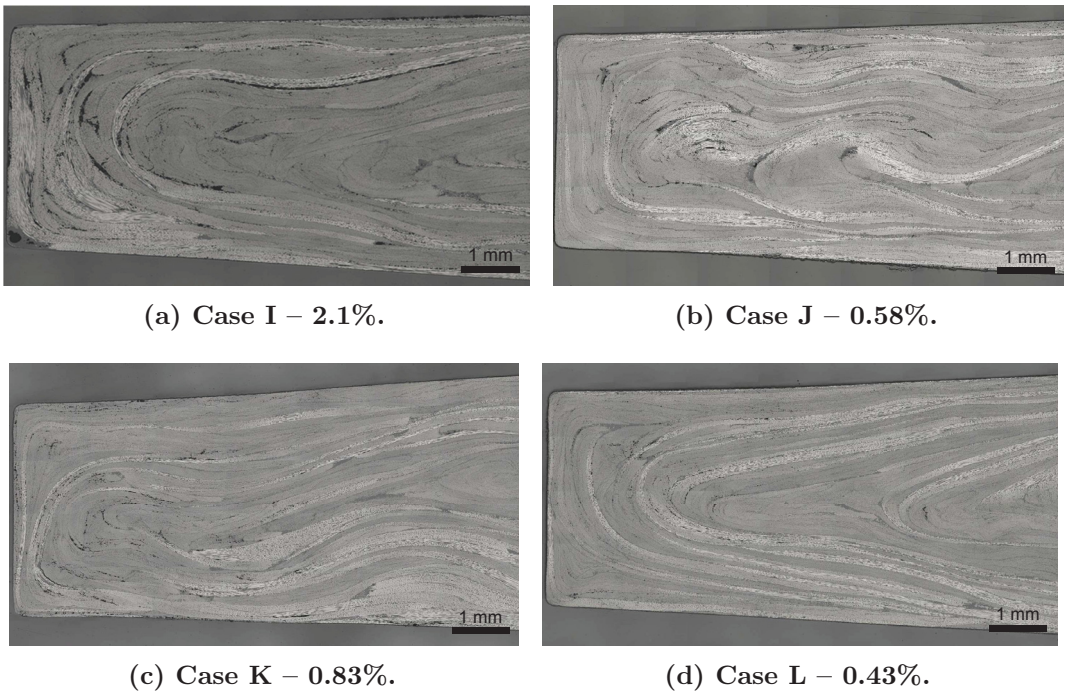

(a) Case I – 2.1%. **(b) Case J – 0.58%.**

(c) Case K – 0.83%. **(d) Case L – 0.43%.**

Figure 6.5 – Representative cross-sectional micrographs of the tip of L-bracket rib sections. The caption refers to the cases and corresponding average void contents, V_{Tip}.

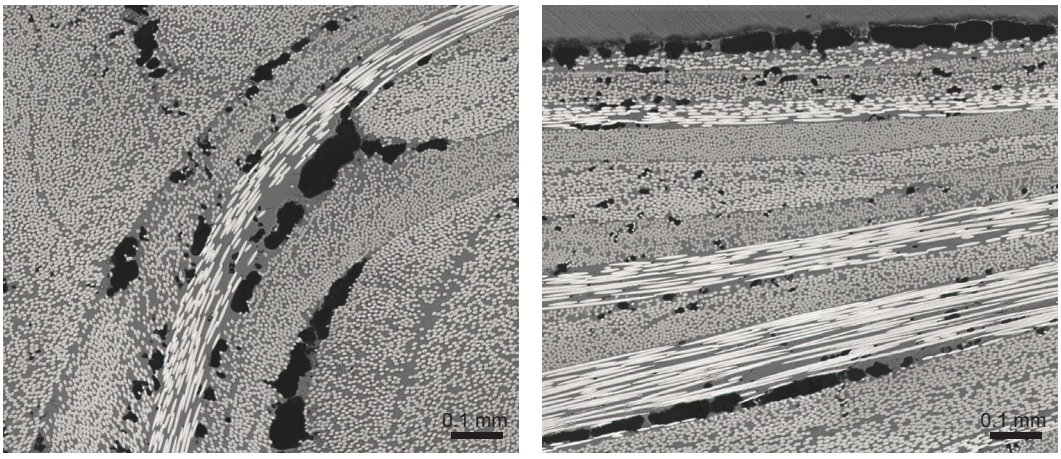

(a) **(b)**

Figure 6.6 – Type of voids found in different regions of the DLF composite L-bracket processed with case I. (a) Near the tip. (b) At the surface.

6.1.4 Micro-CT imaging of L-bracket rib sections

A Skyscan (Kontich, Belgium) 1172 High-Resolution micro-CT system was used to scan one rib sample per moulding condition. The samples were 28 mm $\times$ 6.3 mm $\times$ 6.0 mm. The scan resolution, i.e. the size of the smallest detectable detail, was 8.6 μm/pixel. The scan was performed using an acceleration tension of 63 kV and a current of 157 μA. The volumetric void content of the rib sections was measured using the 3–D analysis feature of Skyscan's CTAn software. The scan volume corresponds to the V_{Base} section shown in Fig. 6.4. Following a methodology similar to that employed in Section 5.2.4, two different void content results were measured: the surface void content and the total void content. The surface void content is defined as

$$V_s = \frac{V_{\text{Void}}^{\text{Top}} + V_{\text{Void}}^{\text{Bottom}}}{V_{\text{Rib}}} \tag{6.1}$$

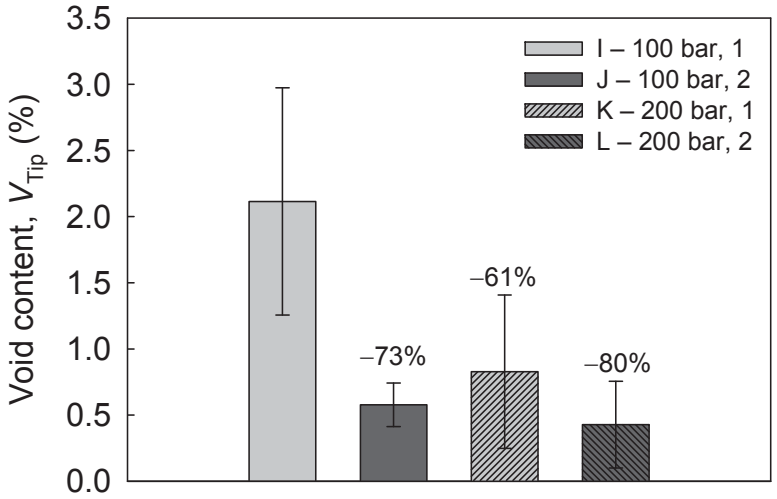

Figure 6.7 – Areal void content of DLF composite L-brackets measured at the tip of rib sections. The legend refers to the cases, corresponding moulding pressures, and cooling methods. The values on top of the columns show the percent reduction with respect to case I. Error bars show one standard deviation.

where $V_{\text{Void}}^{\text{Top}}$ and $V_{\text{Void}}^{\text{Bottom}}$ are the void volume measured 0.55 mm from the top and bottom surfaces of the rib section, respectively, and V_{Rib} is the total volume of the scanned sample. The internal void content was defined as the difference between the total and surface void content.

Three micro-CT slices of a rib section processed with case I are shown in Fig. 6.8. The scans show the composite in pale grey and voids in black. The images show large agglomerations of porosity near the surfaces and the center of the sample. In general, large internal porosity as shown in Fig. 6.8b was much less common than surface porosity, and was mainly observed in case I.

The volumetric void content results for cases I–L are presented in Fig. 6.9. The results show the same trend observed with the areal void content (Fig. 6.7) where case I had much higher void content than the three other cases. The figure also shows that 73% of the voids of case I were located at the surface. The total and surface void content were greatly reduced by employing an appropriate

the cooling strategy (case J) or increasing the moulding pressure (case K), but neither had a significant effect on the internal void content, as very similar values were measured for cases I–K. By combining the higher moulding pressure and cooling strategy (case L), surface porosity was completely eliminated, while internal porosity was 42% lower than case I. This suggests that even higher pressure or a more appropriate air evacuation strategy is required to obtain a completely void-free part. This will be further discussed in the next section.

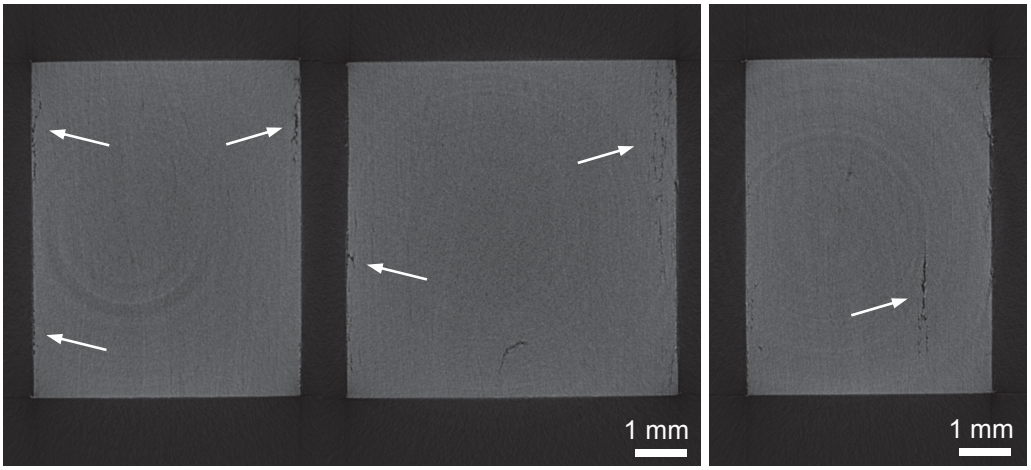

(a) **(b)**

Figure 6.8 – Micro-CT slices of a DLF composite L-bracket rib section at 8.6 μm/pixel showing porosity (a) near the surfaces and (b) inside a rib section processed with case I.

A comparison between the areal and volumetric void content measured in the base section of the rib is shown in Fig. 6.10. The areal void content of each case is the average of the four micrographs (see Fig. 6.2). It can first be observed that the areal void content obtained with micrographs are much higher than the volumetric void content measured via micro-CT. The former was on average 17 times higher. Several factors are responsible for this difference. First,

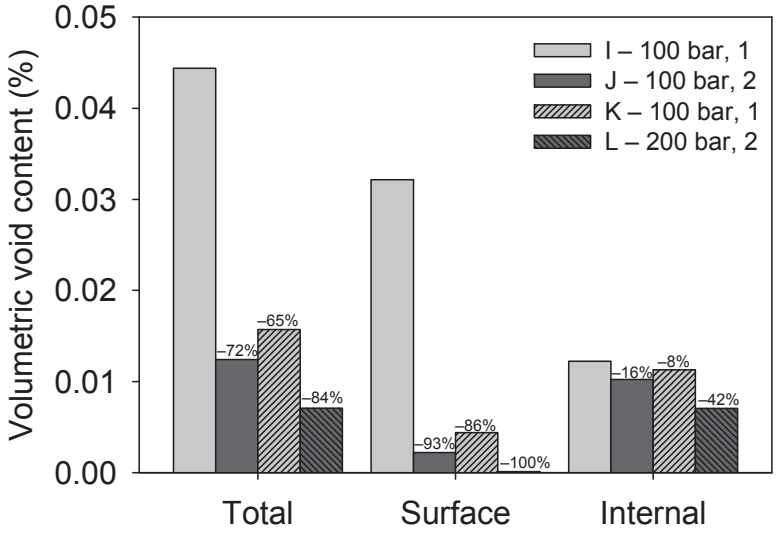

Figure 6.9 – Volumetric void content of DLF composite L-bracket rib sections measured by micro-CT. The legend refers to the cases, corresponding moulding pressures, and cooling methods. The values on top of the columns show the percent reduction with respect to case I.

the resolution of the micrographs was around 0.8 μm/pixel, i.e. 11 times higher than that of the micro-CT. Due to the low resolution of the micro-CT scans, only agglomerated porosity can be detected, mainly because voids smaller than the size of a pixel (8.6 μm) are impossible to differentiate from noise during the thresholding operation. Second, due to thresholding limitations, porosity located directly at the surface of the sample cannot be measured by micro-CT. Lastly, using a small number of samples to quantify the areal void content can lead to large error since porosity is often non-evenly distributed.

6.1.5 Debulk cycle and air entrapment during processing

The importance of the debulk cycle to evacuate the air entrapped in the part before the final high pressure consolidation is depicted in Fig. 6.11. When the debulk cycle was not applied, small unfilled regions were found near the middle of the rib component. The length of the regions were approximately 2.5 mm

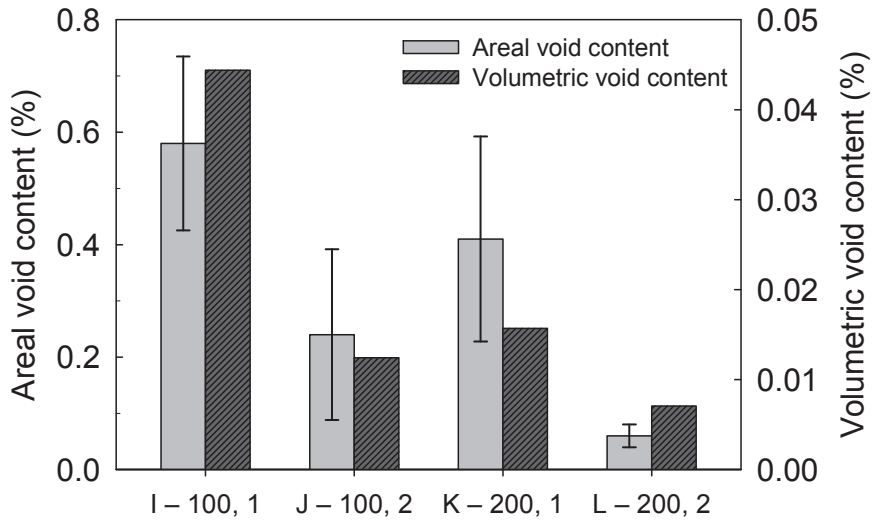

Figure 6.10 – Comparison between areal (micrographs) and volumetric (micro-CT) void content of DLF composite L-brackets measured in the base of the rib sections. Error bars show one standard deviation.

and 0.5 mm for the L-brackets moulded at 100 bar and 200 bar, respectively. An explanation for this behaviour is explained in the following. Since the bulk factor of the DLF strands is around 4–8 to 1, the mould cavity after material placement is filled with around 75% to 90% of air. During moulding of a complex-shaped parts, there is a strong possibility that the geometry will prevent proper air evacuation, leading to entrapped air in certain regions. In the case of the L-bracket, the air initially in the rib cavity is difficult to extract, mainly because it is situated in the middle of the part, away from all shear edges (see Fig. 3.7). This hypothesis is backed up by the facts that unfilled regions were only present when the debulk cycle was not applied and that much higher void content were observed near the tip of the rib sections.

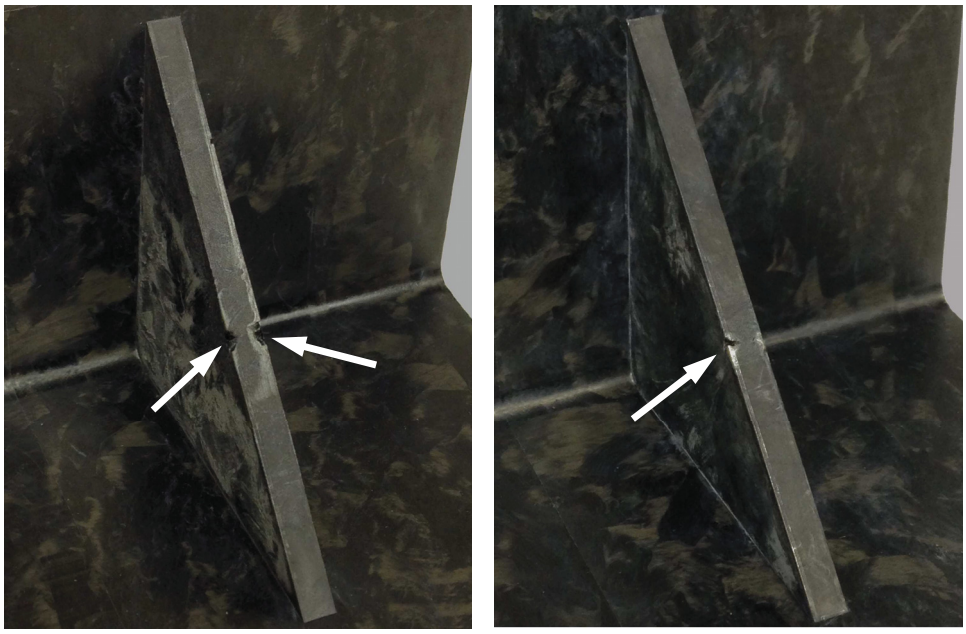

(a) Case M – 100 bar. **(b) Case N – 200 bar.**

Figure 6.11 – Insufficient filling of DLF composite L-bracket rib component when no debulk cycle was applied before the final consolidation of the part. The caption refers to the cases and corresponding moulding pressures.

6.1.6 Summary

A two-factor, two-level design of experiments was performed to evaluate the quality of the rib feature of a DLF composite L-bracket. Optical microscopy and micro-CT were utilized to measure void content. It was found that much smaller defects can be defected with micrographs, while also properly capturing any roughness or porosity located directly at the surface of the part. In contrast, micro-CT was only able to detect large voids, which was due to the poor resolution employed. The void content analysis revealed non-evenly distributed porosity throughout the rib sections, with the most critical region always located near its tip. This was attributed to air entrapment during the filling of the rib cavity. Both the increase in moulding pressure from 100 bar to 200 bar and the

cooling strategy (solidifying the rib feature before the flange) had a positive effect on the void content reduction of the rib. The latter was shown to be more effective, reducing the areal void content by 73% and the volumetric void content by 72% when compared to the baseline. Nonetheless, both factors were required to completely eliminate visible defects and porosity near the surface of the part.

6.2 Influence of moulding defects on the impact properties of DLF composites

To further understand the relationship between processing and mechanical properties, this case study presents an investigation of the effects of moulding defects on the impact properties of DLF composites. The compaction quality of panels manufactured at high and low pressure was assessed by means of cross-sectional micrographs and ultrasonic C-scan analysis. The impact properties were measured via drop-weight impact tests. Impact properties and damage characteristics were compared between the two processing conditions. All impact properties were also benchmarked against a quasi-isotropic continuous fibre composite panel.

6.2.1 Methodology

Three 356 mm × 305 mm panels were manufactured following the moulding procedure described in Section 3.3.2. The first and second panels were moulded using 25 mm × 6.4 mm DLF strands under 35 bar and 10 bar of pressure, respectively. The third panel was a 32-layer quasi-isotropic continuous fibre panel moulded at a pressure of 30 bar. The characteristics of the three panels are presented in Table 1. In the following, the low- and high-pressure processed

DLF composite panels will be referred to as LP-D and HP-D, respectively. The continuous fibre panel will be identified as HP-C.

Table 6.2 – Characteristics of the three large panels manufactured to measure the impact properties of DLF composites.

Panel	Configuration	Pressure (bar)	Thickness (mm)
HP-D	DLF	35	4.52
LP-D	DLF	10	4.57
HP-C	$[45/-45/0/90]_{4S}$	30	4.34

Multiple 25 mm wide samples were taken from each panel in order to inspect their microstructure and measure their void content. The samples were polished using the methodology described in Section 5.1.2 and observed under an optical microscope. Further inspection was performed on the low-pressure processed panel via through-thickness ultrasonic C-scan. The scan was performed on a TecScan (Boucherville, QC) automated 7 axis ultrasonic immersion system equipped with a Utex UT340 Pulser/Receiver and a Panametrics 2.25 MHz 1.3 mm diameter transducer.

Drop-weight impact tests were performed following the ASTM D7136 standard [89]. An advantage of impact testing with regards to DLF composites is the large specimen size, which ensures that the impacted area is always away from the edges of the specimen, where strands are shorter due to the machining operation. Each DLF composite panel was cut into five 150 mm $\times$ 100 mm specimens. Four panels were extracted from the continuous fibre panel. All impact tests were performed on an Instron (Norwood, MA) drop-weight impact tower, model 8200. The impactor was hemispherical and 16 mm in diameter. The impact energy was 30 J, based on the ASTM standard's recommendation

of 6.7 J/mm. An indication of the degree of damage induced by impact loading was obtained by measuring the contact force and the total energy absorbed versus time during the test. All impact data were obtained directly from the data acquisition system. The dent depth was measured on each specimen immediately after impact using a depth gage micrometer equipped with a spherical tip.

6.2.2 Visual observations and defect analysis

A considerable difference can be observed between the two DLF composite panels, as shown in Fig. 6.12. A white triangle-shaped region can be observed on the LP-D panel (Fig. 6.12a), which is generally observed when defects are formed on a part during cooling (see Section 5.2.4). A small number of surface defects can also be observed on the right side of the HP-D panel (Fig. 6.12b). An explanation for the defect formation is described in the following. The cooling system of the press platens was such that the coolant flowed (with reference to Fig. 6.12) from right to left in a main conduit, and from the center to the top and bottom in secondary conduits. This created an in-plane temperature gradient on the panel during cooling, where the temperatures measured by the three thermocouples showed in Fig. 6.12 were such that TC2 $<$ TC1 $<$ TC3. This lead to defect formation on the cold side of the panel. The maximum temperature gradient during cooling was 71 °C, recorded at 110 min into the moulding cycle presented in Fig. 3.5.

The results of the C-scan performed on panel LP–D before impact testing are presented in Fig. 6.13. The panel is represented in five specimens, B1–B5, which are directly comparable with the specimens in Fig. 6.12b. In the image, the peak amplitude is directly related to the density of the material: High amplitude (red) represents defect-free material, while low amplitude (blue) indicates that

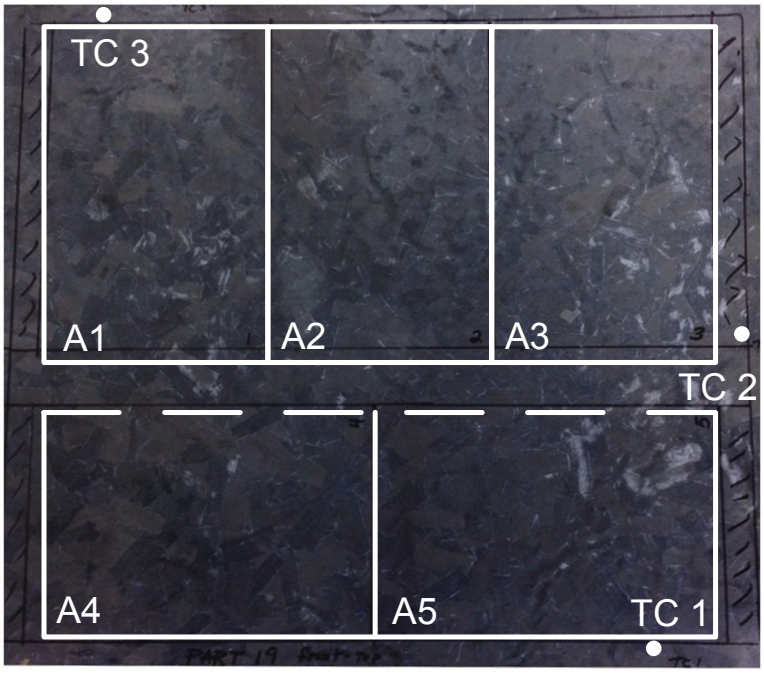

(a)

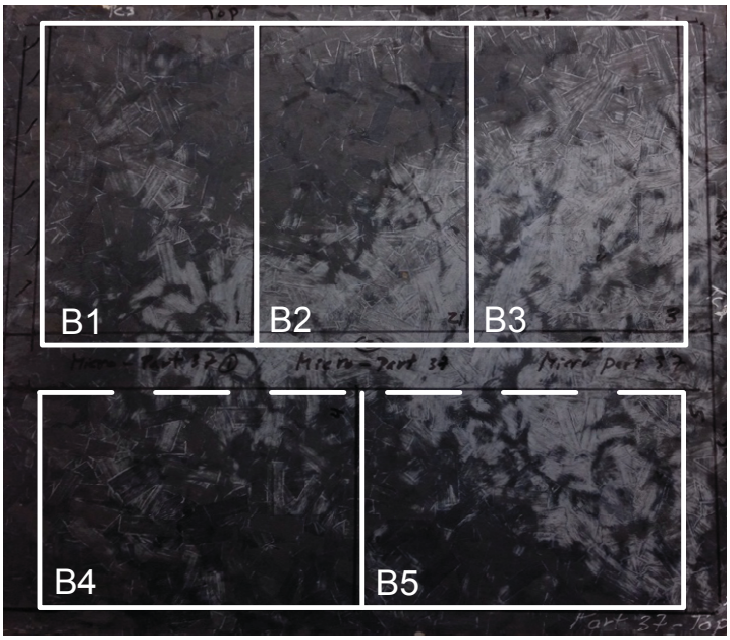

(b)

Figure 6.12 – Large DLF composite panels processed at (a) 35 bar and (b) 10 bar. The press platen's coolant flowed from right to left during cooling. Dots indicate thermocouple location, dashed line indicate area where micrographs were taken.

defects are present. Clear correlation can be observed between the white regions on the surface of the panel and the regions of signal attenuation of the C-scan. This further confirms the hypothesis that there is a direct link between visible surface defects and internal porosity (see Section 5.2.4).

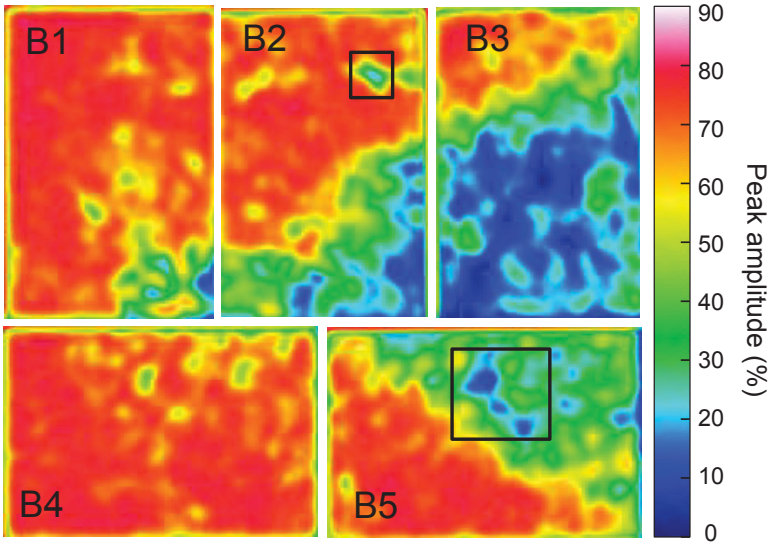

Figure 6.13 – Through-thickness ultrasonic C-scan of the LP-D panel. Signal attenuation can be observed on the right side of the panel.

Apart from the large blue region observed on the right side of the C-scan image of panel LP–D, a few small regions where the signal attenuation was greater than the surrounding material were detected. Micrographs of two hot spots indicated by black rectangles in Fig. 6.13 are shown in Fig. 6.14. The surface of the first hot spot, taken from specimen B2, was a darker shade of black, and appeared to be more compacted than the surrounding material. The micrograph (Fig. 6.14a) revealed that this was due to fibre swirls in the material. The surface of the second hot spot, taken from specimen B5, had a series of small surface voids (i.e. uncompacted regions). A high concentration of porosity was observed in a micrograph (Fig. 6.14b) taken on one of the surface voids.

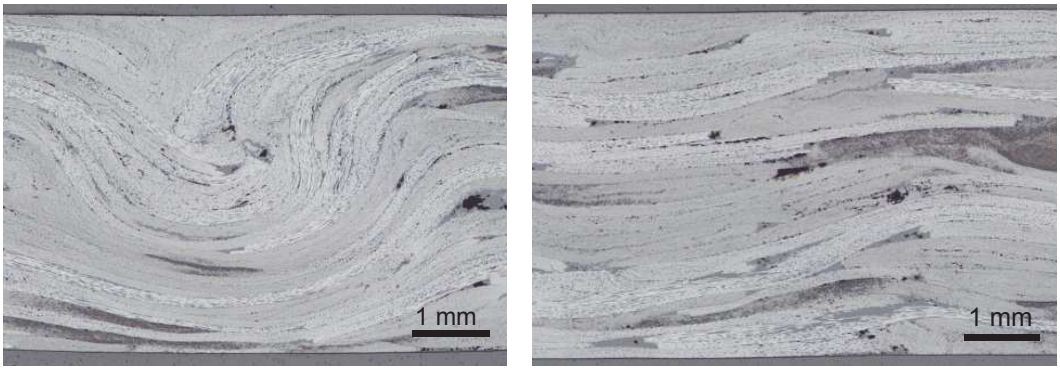

(a) Fibre swirls **(b) Surface void**

Figure 6.14 – Cross-sectional micrographs of two hot spots observed in the LP–D panel.

Void content analysis was performed on all panels. Samples were taken along the dashed lines shown in Fig. 6.12. Two micrographs of the LP–D panel are presented in Fig. 6.15. The sample in Fig. 6.15a was taken on the left side of the panel, while the sample in Fig. 6.15b was taken on its right side, exposing the difference between black and white surface regions of the panel. The micrographs are showing much higher surface void content in the sample taken from the right side of the panel. On average, the void content measured in the LP–D samples was 0.39%. This is slightly lower than the average porosity of 0.63% observed with a PRT of 310 °C (Section 5.2.4). The average void content in the HP–D was 0.09%. Finally, very few voids ($< 0.05\%$) were observed in the HP–C panel.

6.2.3 Impact test results

The damage resistance of all three panels was compared based on three characteristic parameters [90]. First, the incipient damage load F_1, and its corresponding energy E_1, recorded at the first discontinuity of the force vs.

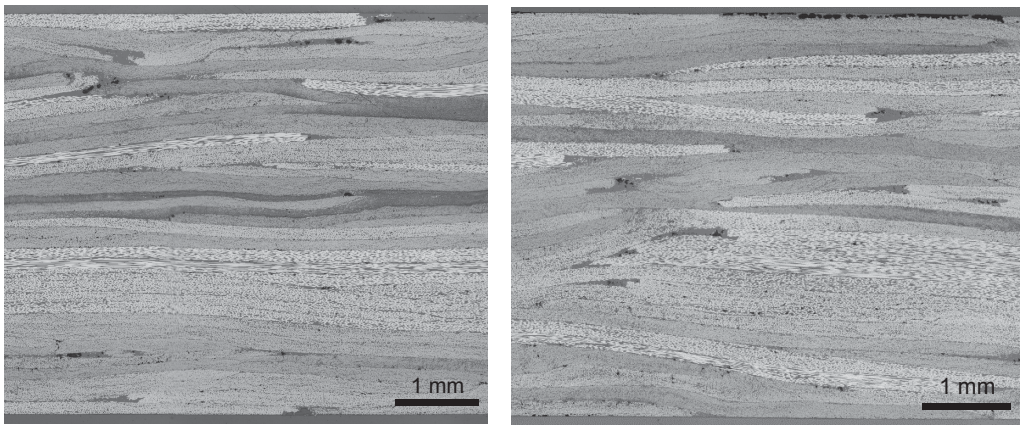

(a) (b)

Figure 6.15 – Cross-sectional micrographs of the LP–D panel taken on the (a) left side (black surface) and (b) right (white surface) of the panel.

time curve, below which the material experiences no impact damage. Second, the maximum recorded contact force $F_{\max}$, an indication the maximum load that the composite can withstand without undergoing major damage. Lastly, the total energy absorbed by the specimen during the impact E_a, which is the difference between the applied impact energy and the elastic energy released by the specimen, calculated based on the rebound acceleration, force, and displacement of the impactor. It is an indication of the degree of damage induced by impact loading, where a perfectly elastic impact event would have $E_a = 0$.

Average results of all impact parameters are presented in Table 6.3. Representative impact load vs. time and energy vs. time curves are presented in Figs. 6.16 and 6.17. All load curves show two to three discontinuities at the beginning of the impact event, which were neglected in the F_1 measurements as they were attributed to harmonic resonance of the impactor and/or specimen [89]. Fig. 6.16 shows clear evidence that the continuous fibre panel had better

impact resistance than the DLF composite panels. On average, F_1 and $F_{\max}$ in both discontinuous fibre panels were 19% and 23% lower than that measured in the continuous fibre panel. These two values were very similar between the two DLF composite panels, with differences of 1.3% and 0.4% for F_1 and $F_{\max}$, respectively. The total absorbed energy E_a, was the impact parameter most affected by the fibre architecture, where it was on average 42% higher in the DLF composite panels. Differences in E_1 and E_a between the LP–D and HP–D panels were only 2.4% and 5.3%, respectively.

Table 6.3 – Impact testing results.

Panel	F_1 (kN)	E_1 (J)	$F_{\max}$ (kN)	E_a (J)
HP–D	6.71 ± 0.92	8.37 ± 2.52	9.45 ± 0.48	14.4 ± 1.92
LP–D	6.80 ± 0.86	8.17 ± 2.10	9.41 ± 0.67	13.6 ± 1.20
HP–C	8.31 ± 0.28	11.0 ± 0.85	12.2 ± 0.21	9.83 ± 0.62

Student's t-tests ($\alpha = 0.05$) were performed in order to determine if the processing pressure and fibre architecture had a significant influence on the impact behaviour of the three panel tested. The analyses were performed on parameters F_1, E_1, $F_{\max}$, and E_a. Results showed that for both DLF composite panels, the pressure had no influence on any of the impact parameters tested. Furthermore, no correlation was found between the amount of surface discolouration and the impact performance of all specimens taken from the LP–D panel. A reasonable explanation would be that the impact damage did not initiate on the surface of the specimen where the highest concentration of voids is generally located. This would suggest that the damage mainly propagated inside the specimens, and that the 0.3% difference in total void content between the two DLF composite panels was too small to significantly affect the impact performance. While

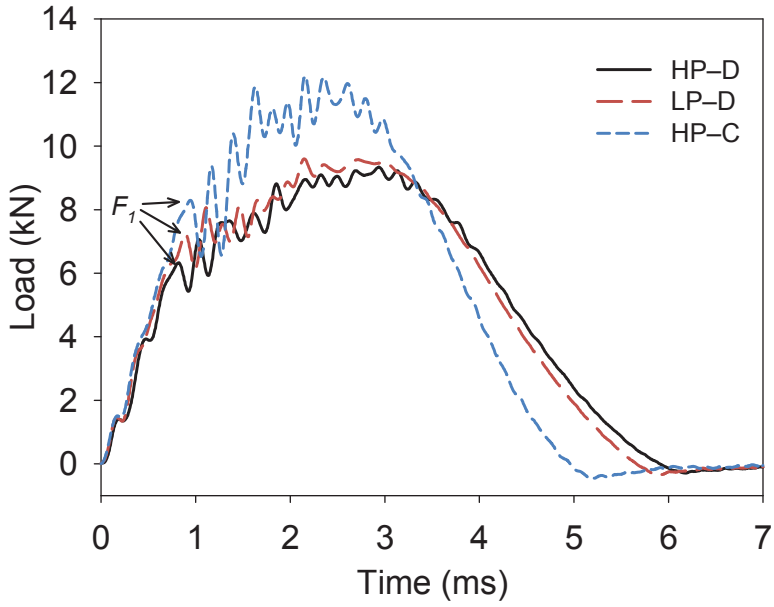

Figure 6.16 – Typical impact load vs. time curves showing incipient damage load F_1 for the three panels tested.

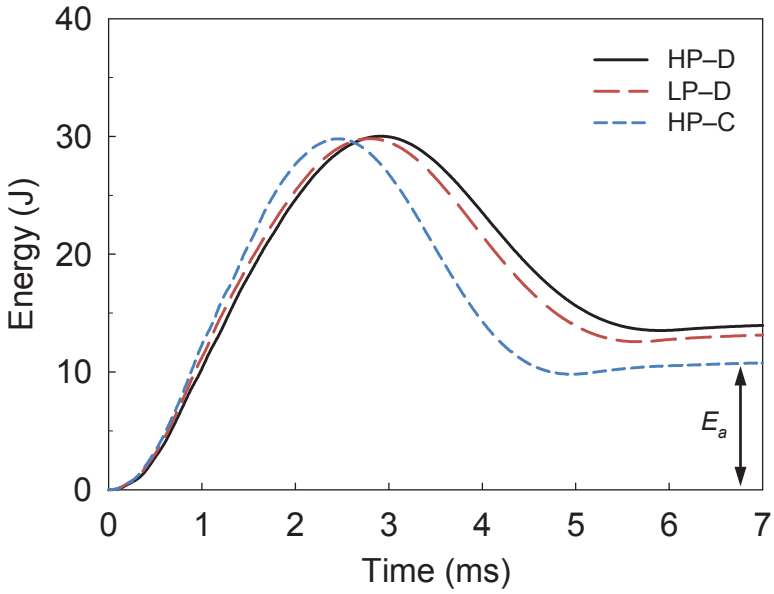

Figure 6.17 – Typical impact energy vs. time curves for the three panels tested. The total absorbed energy E_a is shown for the HP–C panel.

the impact properties were very similar between DLF composite panels, it was found that the fibre architecture, continuous vs. discontinuous, had a significant influence on all impact parameters. This will be further discussed in the following section.

6.2.4 Post-impact damage evaluation

Visible impact damage on the underside of representative test specimens are shown in Fig. 6.18. The damage on both discontinuous fibre panels was mainly composed of delamination around the strands, cracks, and small amount of fibre failure (Fig. 6.18a,b). Small cracks were also observed near the dent on the impacted side of the specimens. Nonetheless, no clear differences in the failure modes were observed between the LP–D and HP–D panels. The surface damage on the underside of all four HP–C specimens (Fig. 6.18c) was comprised of long cracks in the 45° surface ply. Apart from the impact dent, no visible damage was observed on the impacted side of the specimens.

Post-impact damage evaluation was performed via ultrasonic C-scan. A representative specimen from each panel is presented in Fig. 6.19. The average impact damage area and dent depth are listed in Table 6.4. The results show that the smallest dent depth and largest impact damage area were measured on the HP–C panel. The straight paths between layers are thus prone to large delamination, leading to a larger surface area of damage. In contrast, a smaller damage area and a larger impact dent depth was observed in the DLF composites panels. This suggests that it was more difficult for cracks to propagate in the random mesostructure of the DLF composites, which lead to a more localized impact damage.

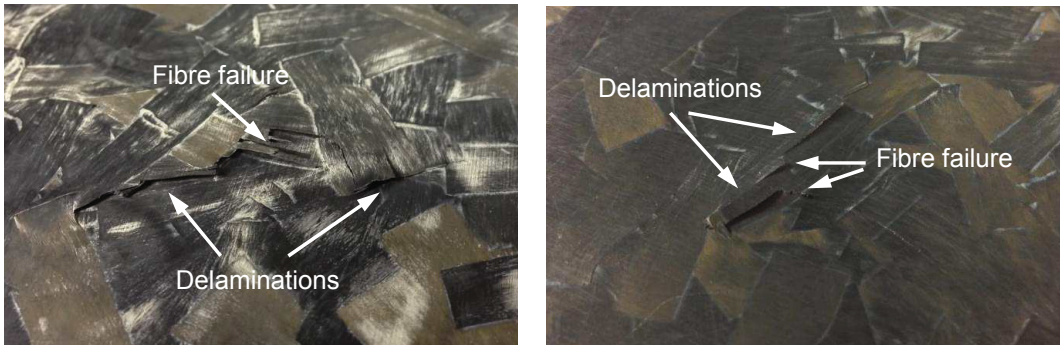

(a) LP–D (b) HP–D

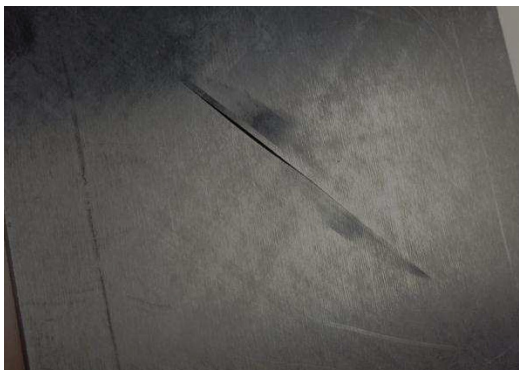

(c) HP–C

Figure 6.18 – Visible damage observed on the underside impact-induced specimens.

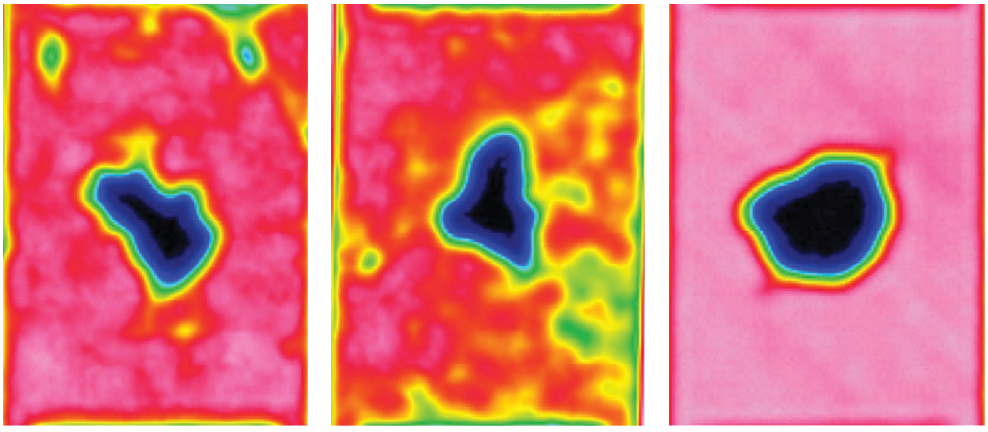

(a) HP–D (b) LP–D (c) HP–C

Figure 6.19 – Post-impact damage evaluation via ultrasonic C-scan. The impact damage area is located at the center of each specimen.

Table 6.4 – Post-impact damage evaluation results.

Panel	Impact damage area (mm^2)	Dent depth (mm)
HP–D	1475 ± 278	0.90 ± 0.14
LP–D	1268 ± 293	0.76 ± 0.07
HP–C	2323 ± 646	0.50 ± 0.02

6.2.5 Summary

The effect of the processing pressure on compaction quality and impact properties of DLF composites was investigated. Two large DLF composite panels were moulded at high (35 bar) and low (10 bar) pressure. A large amount of surface defects were observed on the low-pressure processed panel. The surface defects were clearly detected via ultrasonic C-scan. All impact parameters measured on both DLF composite panels were insensitive to the processing pressure and void content. The damage modes were also similar for both panels. However, the fibre architecture had a significant influence on the impact properties; in comparison with DLF composite panels, the maximum contact force was 29% higher, the total absorbed energy was 30% lower, and impact damage area was 70% higher in the quasi-isotropic continuous fibre laminate. The fibre architecture also greatly influenced the impact damage modes observed at the surface of the panels.

Chapter 7

Pressure Distribution Model

The results from previous chapters have shown that the loss of contact during processing of DLF composites can results in defect formation which can affect the mechanical properties of the material. In Section 6.1, defects on a real DLF composite part were observed on the surface of its complex region, even under moulding pressure as high as 100–200 bar. It was also demonstrated that an appropriate cooling strategy is required to obtain a defect-free surface. It is thus safe to assume that defect formation in a very complex DLF composite part is almost impossible to predict without the help of process modelling. Without the latter, part and tooling design would be developed at a great expense by trial and error.

In this chapter, a finite element model is developed to predict the influence of thermal gradient and moulding pressure on the pressure distribution of compression moulded DLF carbon/PEEK composites. The model employs the material's temperature dependant thermomechanical properties measured in Chapter 4, i.e. transverse modulus and thermal shrinkage. An analytical model is developed to evaluate the variation of thermomechanical properties as a function of temperature, cooling rate, and degree of crystallinity. The model output is the pressure distribution on the part during cooling. Critical areas where pressure is lost during and the corresponding material temperature

are identified. The model was validated on simple flat DLF composite panels moulded at different moulding pressures. The model is then employed in two parametric studies, where the influence of the process parameters are investigated. Finally, recommendations are made in order to minimize the risk of defect formation when manufacturing complex-shaped DLF composite parts.

7.1 Model development, schematic and assumptions

The moulding of flat DLF composite panels in a hot press was modelled. The experimental setup and moulding procedures were presented in Section 3.3.1. A schematic of the 3–D model is shown in Fig. 7.1. Due to symmetry in the platen temperature about the y-axis during cooling, half of the mould was modelled.

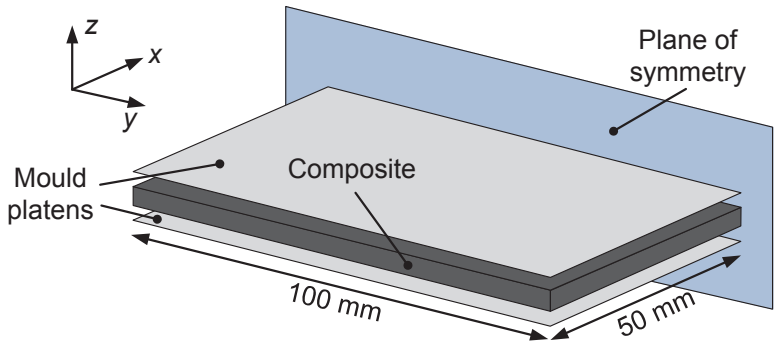

Figure 7.1 – Schematic of the 3–D compaction model. Half of the mould/material assembly was modelled.

A flowchart of the compaction model showing its inputs and outputs is presented in Fig. 7.2. Starting with the temperature distribution of the part during cooling obtained via heat transfer analysis or in-situ measurements, the temperature dependant thermomechanical properties are evaluated using the analytical models developed in Section 7.2. The latter is employed to evaluate

the instantaneous variation in modulus and thermal shrinkage at each time step as a function of temperature, cooling rate, and degree of crystallinity. After applying the desired moulding pressure to the mould platens, the pressure distribution on the part is solved at each time step, from the start of the cooling process, until the entire part has gone through the crystallization temperature range of PEEK matrix (260–320 °C). From the solution obtained at each time step, regions where the pressure has dropped to zero are identified. Knowing the material's temperature at the point where localized pressure was lost, the amount of defects can be predicted with the results obtained in Section 5.2.4.

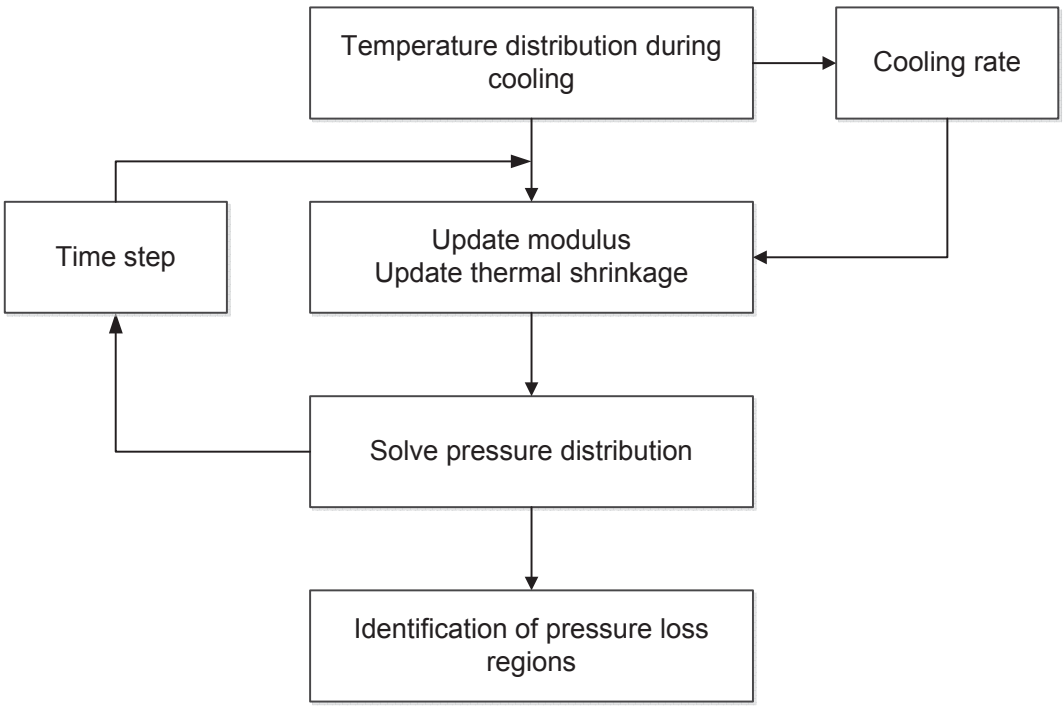

Figure 7.2 – Flowchart of the compaction model showing its inputs and outputs.

The following major assumptions were made in the present model:

- The mould platens are perfectly parallel,
- DLF composite strands have no out-of-plane orientation,
- Thermal expansion of the mould platens (steel) is negligible,
- Thermal shrinkage of the composite in the fibre direction is negligible (see Fig. 4.8),
- The material behaviour in the temperature range considered is purely elastic. Material flow is neglected (see Section 4.3).

7.2 Modelling thermomechanical properties of carbon/PEEK composite

The evolution of the thermomechanical properties of carbon/PEEK tape during cooling from melt was characterized using thermal analyses in Chapter 4. The thermal shrinkage was measured using TMA, while the thermoelastic properties were characterized with DMA. Due to relatively large sample size and heat transfer limitations of both instruments, the heating and cooling rates were 1 °C/min. Since crystallization kinetics are influenced by cooling rates (Fig. 4.2), the measured properties are thus not valid for cooling rates of 5–20 °C/min typical found during compression moulding of DLF composites. Therefore, to obtain a precise evolution of the thermal shrinkage and modulus for cooling rates up to 20 °C/min, an analytical model is proposed where the properties measured at slow cooling rate are calibrated with the crystallization kinetics measured by DSC. The procedure is explained in the following. First, it is assumed that the crystallization data measured by DSC for different cooling rates are accurate, since the mass of material used for the test is very small, i.e. in the range of 5–15 mg. This is much smaller than the weight of TMA

and DMA samples, typically around 0.3 g and 1.9 g, respectively. Second, for both thermal shrinkage and out-of-plane modulus, the measured property during cooling was separated in two phases, amorphous and crystalline. Finally, the properties of the crystalline phase were adjusted to take into account the change in the crystallization kinetics at higher cooling rates. This procedure is summarized in Fig. 7.3. The models are presented in the following sections.

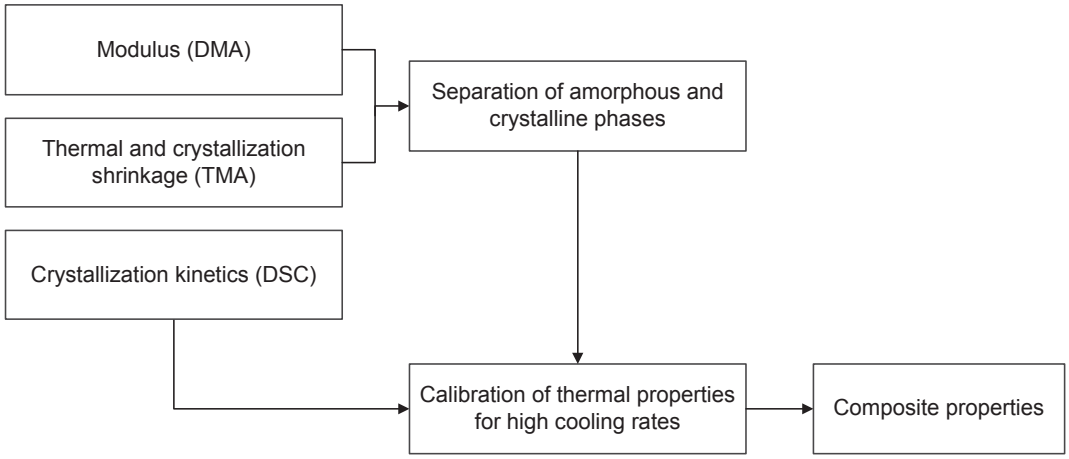

Figure 7.3 – Procedure employed to obtained thermomechanical properties of carbon/PEEK composites at high cooling rates.

7.2.1 Thermal shrinkage modelling

The transverse thermal and crystallization shrinkage of carbon/PEEK composite measured at 1 °C/min (Section 4.2) is reproduced in Fig. 7.4. Since the slope of the curve is very similar before (∼325 °C) and after (∼295 °C) crystallization, it was separated in two components; the amorphous and crystalline phases. The two components are represented by the two dashed lines in Fig. 7.4.

The thermal expansion was represented by:

$$\varepsilon_{33}(T) = (1 - V_f)(1 + \varepsilon_a(T) + \varepsilon_c(T)) \tag{7.1}$$

where ε_a is the transverse shrinkage of the amorphous phase, ε_c is the transverse shrinkage of the crystalline phase, both as a function of temperature. Assuming a linear relationship between volume fraction crystallinity and crystallization shrinkage, the thermal expansions of the two phases were obtained by curve fitting and are given by:

$$\begin{aligned}
&\varepsilon_a(T) = aT^3 + bT^2 + cT + d, \qquad 200^\circ\mathrm{C} < T < 297^\circ\mathrm{C} \\
&\varepsilon_a(T) = e(T - 297) + 0.0761, \qquad T \geq 297^\circ\mathrm{C} \\
&\varepsilon_c(T) = 0.0689 X_{vc}(T) \\
&a = 5.32 \times 10^{-9}\ ^\circ\mathrm{C}^{-3} \quad b = -2.16 \times 10^{-6}\ ^\circ\mathrm{C}^{-2} \\
&c = 5.49 \times 10^{-4}\ ^\circ\mathrm{C}^{-1} \quad d = -0.0354 \quad e = 6.71 \times 10^{-4}\ ^\circ\mathrm{C}^{-1}
\end{aligned} \tag{7.2}$$

where $X_{vc}(T)$ is the evolution of the volume fraction crystallinity with temperature. It should be noted that the thermal strains in Eq. (7.1) are expressed in absolute values. A precise estimation of the transverse thermal strain at different cooling rates was then calculated by combining the crystallization kinetics results of Fig. 4.2 with Eqs. (7.1) and (7.2). The results are shown in Fig. 7.5 for cooling rates between 1 °C/min and 20 °C/min.

7.2.2 Transverse modulus modelling

The transverse modulus of the composite as a function of temperature was modelled using the inverse rule of mixtures:

$$E_{33}(T) = \left(\frac{V_f}{E_f} + \frac{1 - V_f}{E_m(T)} \right)^{-1} \tag{7.3}$$

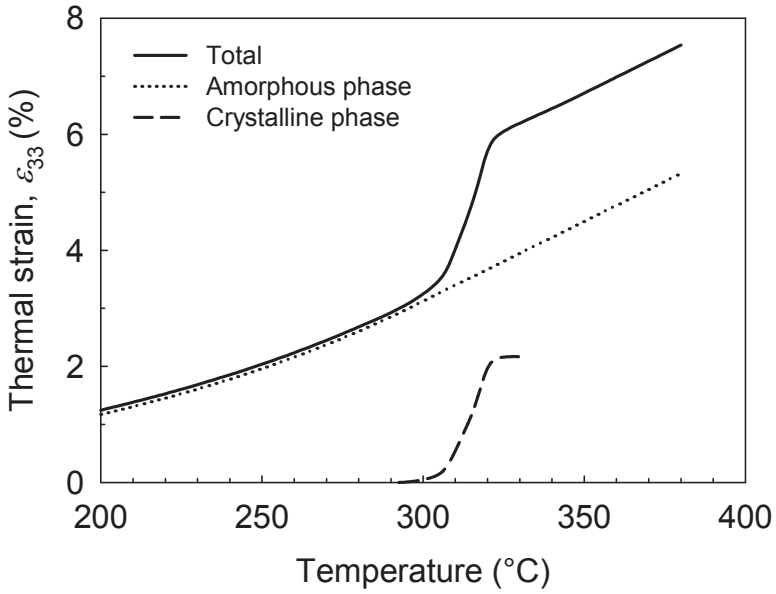

Figure 7.4 – Measured transverse thermal strain of carbon/PEEK composite separated into two components: the amorphous and crystalline phases. The amorphous phase component was offset for clarity.

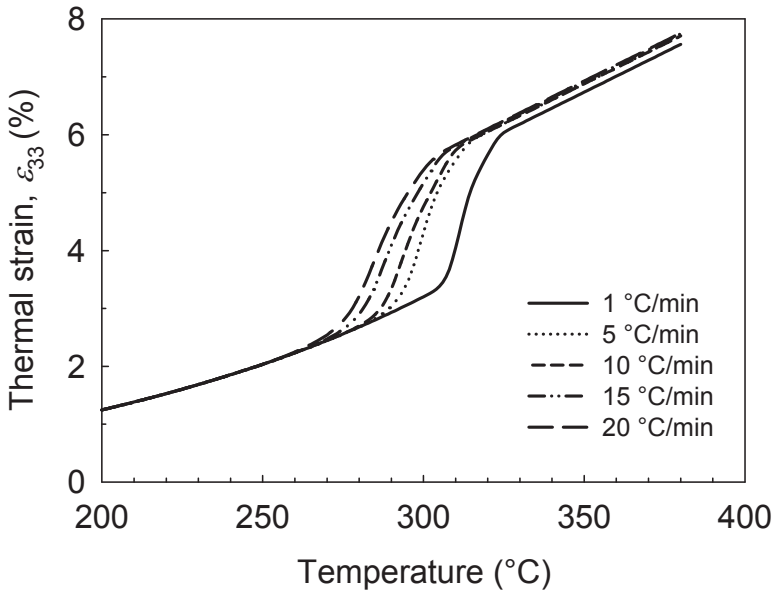

Figure 7.5 – Modelled transverse thermal strain of carbon/PEEK composite vs. temperature for different cooling rates.

where E_f is the transverse modulus of the fibres and E_m is the modulus of the matrix as a function of temperature. The modulus of the matrix was in turn expressed using the rule of mixtures [65]:

$$E_m(T) = X_{vc}(T)E_c + (1 - X_{vc}(T))E_a \tag{7.4}$$

where E_c and E_a are the modulus of the crystalline and amorphous phases, respectively. Their values were obtained using curve fitting and are given by:

$$\begin{aligned}
&E_c(T) = 1.76 \text{ GPa} \\
&E_a(T) = aT^2 + bT + c \text{ GPa} \qquad 200^\circ\text{C} < T < 304^\circ\text{C} \\
&E_a(T) = d(T - 304) + 0.05 \text{ GPa} \qquad T \geq 304^\circ\text{C} \\
&a = -4.34 \times 10^{-5} \text{ GPa}^\circ\text{C}^{-2} \quad b = 5.90 \times 10^{-3} \text{ GPa}^\circ\text{C}^{-1} \\
&c = 2.23 \text{ GPa} \quad d = -2.89 \times 10^{-4} \text{ GPa}^\circ\text{C}^{-1}
\end{aligned} \tag{7.5}$$

The value for E_f in Eq. (7.3) was fixed to 21 GPa for carbon fibre [65]. It should be pointed out that the modulus of the crystalline phase used in this study doesn't reflect its real modulus of 30 GPa reported in [91]. The evolution of the transverse modulus of the composite at different cooling rates was then estimated by calibrating the modulus of the PEEK matrix in Eq. (7.4) with the crystallization kinetics results of Fig. 4.2. The results are shown in Fig. 7.6.

7.3 In-situ temperature measurements

To simplify the model and eliminate the need to perform a heat transfer analysis, the temperature distribution of the material in the instrumented hot press during cooling was measured experimentally using 1 mm thick braided fibreglass thermocouples embedded at the midplane of a 24-layer continuous

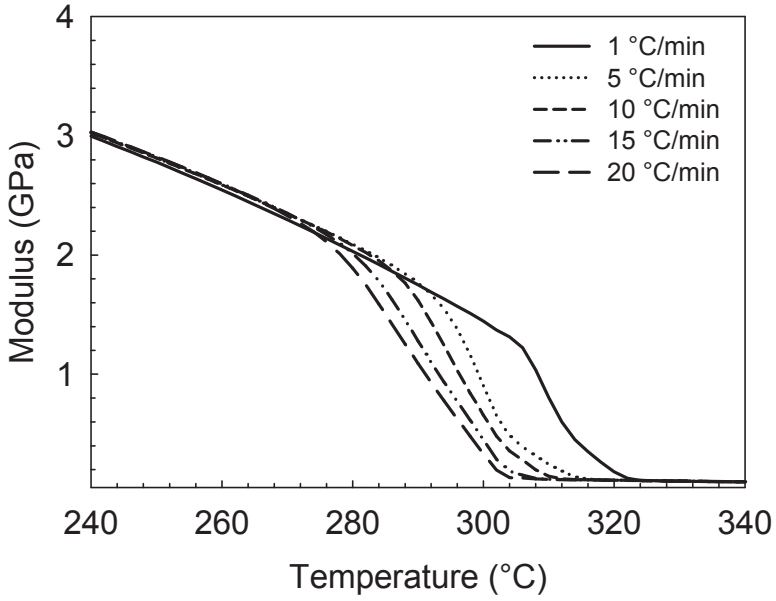

Figure 7.6 – Modelled transverse modulus of carbon/PEEK composite vs. temperature for different cooling rates.

fibre panel with a stacking sequence of $[0/90]_{6S}$. The cooling rate of the panel was 10 °C/min and the temperature data was recorded at 1 Hz. A schematic of the temperature measurement locations and a contour plot of the temperature distribution at a given time during cooling are presented in Fig. 7.7.

7.4 Elements and boundary conditions

All numerical simulations were performed with ANSYS® Mechanical Parametric Design Language. The composite panel was modelled with 3–D 20-node coupled-field solid element. The mould platens were modelled as rigid bodies, using rigid-deformable contact surfaces between them and the composite. The list of elements used in the model is presented in Table 7.1. The boundary conditions applied to the model are depicted in Fig. 7.8. The pressure was applied on the top platen, while sliding conditions were applied to all other

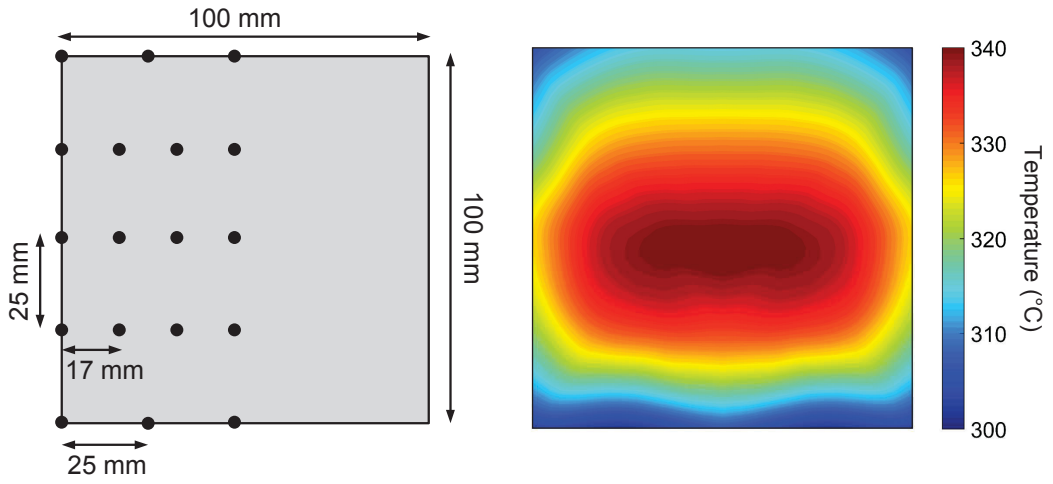

Figure 7.7 – In-situ temperature measurement of a composite panel in the instrumented hot press. (a) Thermocouple locations with respect to the mould platen. (b) Contour plot of the measured material temperature distribution at a given time during cooling. Air flows from top to bottom during cooling.

sides. The parallelism of the mould platens was obtained by restricting the rigid contact elements to only one degree of freedom (z direction). This ensures that the mould platens are always parallel to each other.

Table 7.1 – Elements used in the 3–D compaction model.

Component	Elements	Degrees of freedom
Composite	SOLID226 (20 nodes)	UX, UY, UZ, TEMP
Mould platens	CONTA174 (8 nodes) TARGE170 (8 nodes)	UZ

The composite was modelled as in-plane isotropic. The in-plane properties were assumed to have the same temperature dependence as the transverse modulus $E_{33}(T)$ defined in Eq. (7.3). They were calibrated with the properties

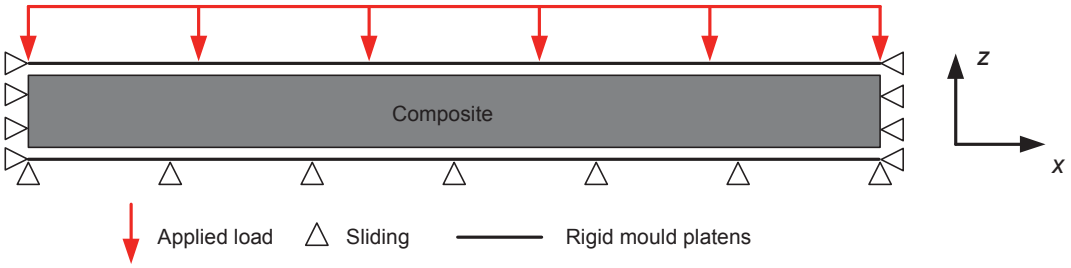

Figure 7.8 – Boundary conditions applied to the model (2–D cross-section shown).

measured at room temperature in [46], and are presented in Table 7.2. The simulation was performed as follows. For every five second step in the temperature measurement data (Section 7.3), the corresponding temperature was applied to each node of the finite element model. The load that corresponds to the desired moulding pressure was applied to the top platen and a solution was obtained. After each step, the position and temperature of the nodes where the pressure was zero were recorded. Once the simulation was completed, a contour plot was generated, showing the temperature at the moment when the pressure was lost on the panel.

Table 7.2 – Temperature dependent material properties of carbon/PEEK composite employed in the compaction model. $E_{33}(T)$ is defined in Eq. (7.3).

$E_x = E_y$ (GPa)	E_z (GPa)	$\nu_x = \nu_y = \nu_z$	G_{xy} (GPa)	$G_{yz} = G_{xz}$ (GPa)
$3.9E_{33}(T)$	$E_{33}(T)$	0.31	$\dfrac{E_x}{2(1+\nu)}$	$7.1\dfrac{E_{33}(T)}{E_{33}(T)_{\mathrm{RT}}}$

RT = Room temperature

7.5 Comparison of modelled pressure distribution with experiments

The numerical model was validated by comparing the predicted defect areas against the ones found on flat 100 mm × 100 mm DLF composite panels moulded at five different cooling pressures: 10, 30, 50, 90, and 110 bar. The panels were moulding following the procedure described Section 3.3.1, using heating and dwelling pressures of 10 bar and 70 bar, respectively.

The results of the validation test are presented in Figs. 7.9 and 7.10. In the figures, the contour plots on the right show the predicted pressure loss temperature (PLT), i.e. the temperature at the moment when pressure was reduced to zero at any point on the panel. This parameter is related to the pressure release temperature (PRT) employed in Chapter 5, where pressure was intentionally released at predetermined temperatures during cooling. As previously shown in Table 5.4, the higher the PRT (or PLT), the higher the void content in the part. Regions where the consolidation pressure was maintained during the entire cooling process are shown in grey. On the moulded panels (left side of the figure), regions where pressure was lost during cooling have a white discoloration at the surface, as previously discussed in Sections 5.2.4 and 6.2.2. The outline of the defect-free region (in grey) predicted by the model were overlaid on the moulded panels. Overall, a good correlation was found between the model and the experiments.

As expected, the numerical results show a reduction of the defect area with increasing pressure. The same trend was observed experimentally. It is also increasingly more difficult to reduce the defect area as the pressure is increased. This is because the applied load is distributed on a progressively larger area as the defect region is reduced. The predicted PLTs were also reduced with

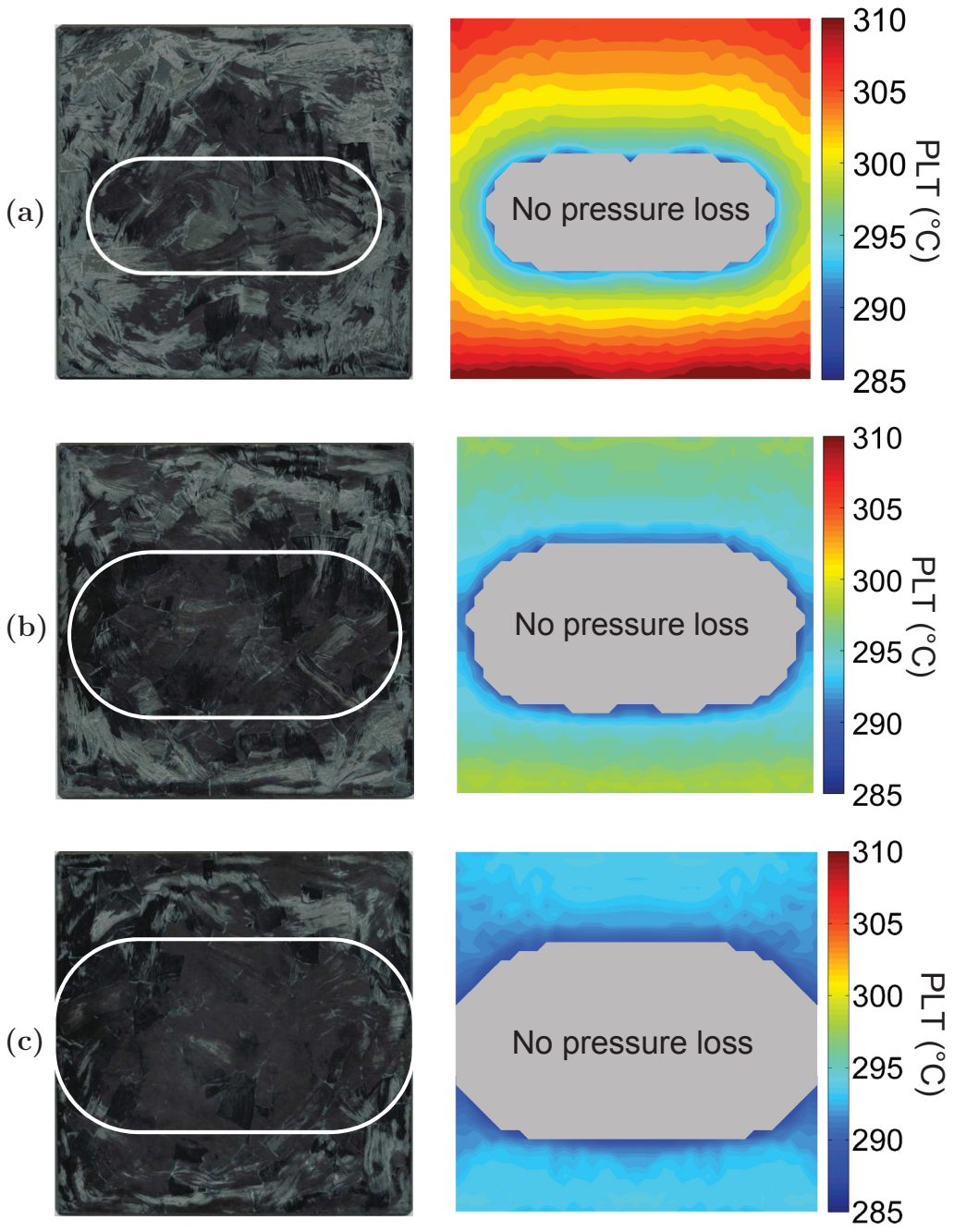

Figure 7.9 – Comparison between model and experiments for processing pressure of (a) 10 bar, (b) 30 bar and (c) 50 bar. Left: Experimental panels showing surface defects and the outline of the defect-free region predicted by the model. Right: Model showing the pressure loss temperature (PLT) during cooling. Air flows from top to bottom during cooling.

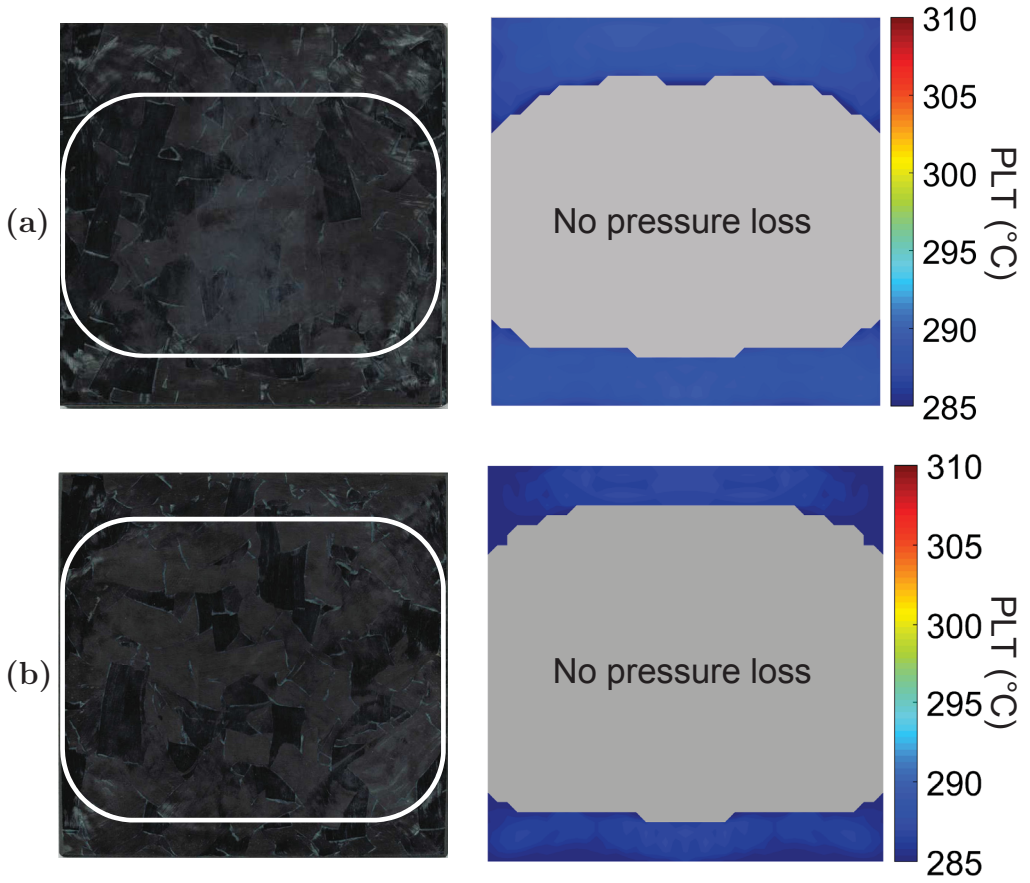

Figure 7.10 – Comparison between model and experiments for processing pressure of (a) 90 bar and (b) 110 bar. Left: Experimental panels showing surface defects and the outline of the defect-free region predicted by the model. Right: Model showing the pressure loss temperature (PLT) during cooling. Air flows from top to bottom during cooling.

Table 7.3 – Maximum and average pressure loss temperatures (PLT) obtained numerically with moulding pressure ranging from 10 bar to 110 bar.

Pressure (bar)	Maximum PLT (°C)	Average PLT (°C)
10	311.7	301.8
30	298.6	295.1
50	294.2	292.2
90	289.6	288.1
110	287.5	286.0

increasing pressure. Experimentally, this reduction translated to an increasingly smoother surface in the defect regions. Table 7.3 summarizes the maximum and average PLTs obtained numerically. According to the experimental results from Chapter 5, defects should only form when the pressure is lost above 300 °C. Therefore, except for a moulding pressure of 10 bar, the results from Figs. 7.9 and Fig. 7.10 are underpredicting the PLTs. For example, maximum PLTs at 30 bar (298.6 °C) and 50 bar (294.2 °C) are both under 300 °C, while defects are clearly visible on the moulded panels. The difference is explained by the fact that the out-of-plane modulus is modelled as linear elastic. In reality, the compaction curve should be non-linear, especially at high load, due to the influence of the highly non-compressible fibre bed [92]. The addition of such curve to the model would have the effect of reducing the overall compaction on the panels, thus increasing the defect areas, as well as the PLTs.

7.6 Parametric Studies

7.6.1 Effect of part temperature variation on defect formation

The temperature measurement performed on a 100 mm × 100 mm panel in Section 7.3 revealed a maximum part temperature variation of 37 °C during cooling. This variation was observed between the center of the panel and its corners. This parametric study aims at quantifying the effect of this part temperature variation on pressure loss temperature. Using the temperature data obtained in Section 7.3, the temperature distribution in the panel was changed using the following equation:

$$T = T_{\text{original}} - \left(\frac{T_{\text{max}} - T_{\text{original}}}{R} \right) \tag{7.6}$$

where T is the temperature at any point on the panel at a given time t, T_{original} is the temperature measured at that point, $T_{\max}$ is the maximum temperature measured on the panel at the time t, and R is a reduction parameter. Two cases were studied in addition to the original results obtained in the previous section. They were obtained with $R = 2$ and $R = 4$, corresponding to half (18.5 °C) and a quarter (9.3 °C) of the original temperature variation. The model was employed for the three cases, under moulding pressures ranging from 10 bar to 130 bar. The maximum PLT was obtained for each case and the data was represented on a contour plot, as shown in Fig. 7.11. The results are showing that the PLTs are greatly influenced by the moulding pressure and the part temperature variation. Interestingly, reducing the part temperature variation can have a significant effect on reducing the PLT. For example, by comparing the results obtained at points (37 °C, 85 bar), (37 °C, 130 bar), and (27 °C, 85 bar), it can be observed that reducing the temperature variation from 37 °C to 27 °C has the same effect on the PLT as increasing the moulding pressure from 85 bar to 130 bar.

The results from this case study thus showed the importance of minimizing the part temperature variation during cooling. Although reducing the part temperature variation to zero would be ideal when moulding a relatively flat component, it will be shown in the next section that is not necessarily the case for complex-shaped components.

7.6.2 Effect of cooling strategy on defect formation

The goal of this parametric study is to quantify the effect of the cooling strategy (which component is cooled first) on the PLT of a rib feature moulded at different pressures. This is based on the strategies employed in Section 6.1 in order to mould a defect-free L-bracket. A schematic of the 2–D model of the rib

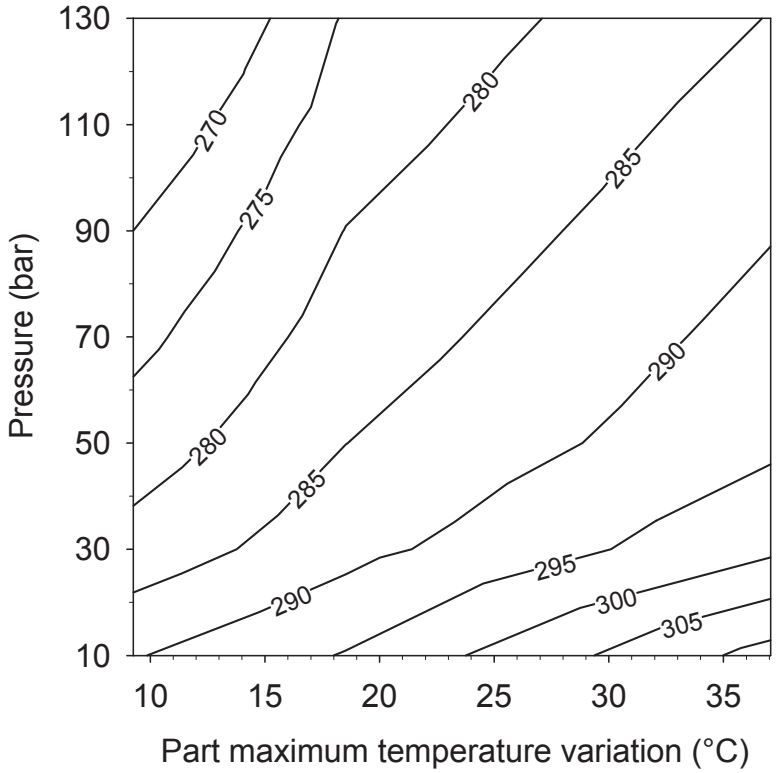

Figure 7.11 – Influence of the part temperature variation and moulding pressure on the maximum PLT of small 100 mm × 100 mm DLF composite panels.

and flange sections of the L-bracket (see Section 3.3.3) is presented in Fig. 7.12. The coordinate systems in the figure show the local fibre orientation, where x and y are the in-plane and out-of-plane orientations, respectively. A smooth transition was applied to the local fibre orientation at the intersection between the rib and the flange. The two tooling components (base and punch) were modelled as rigid bodies using rigid-deformable contact surfaces. The list of elements used in the 2–D model is presented in Table 7.4. The thermomechanical properties from Table 7.2 were utilized in the 2–D simulations, while assuming a cooling rate of 10 °C/min. The boundary conditions were similar to those applied in the 3–D model (Fig. 7.8).

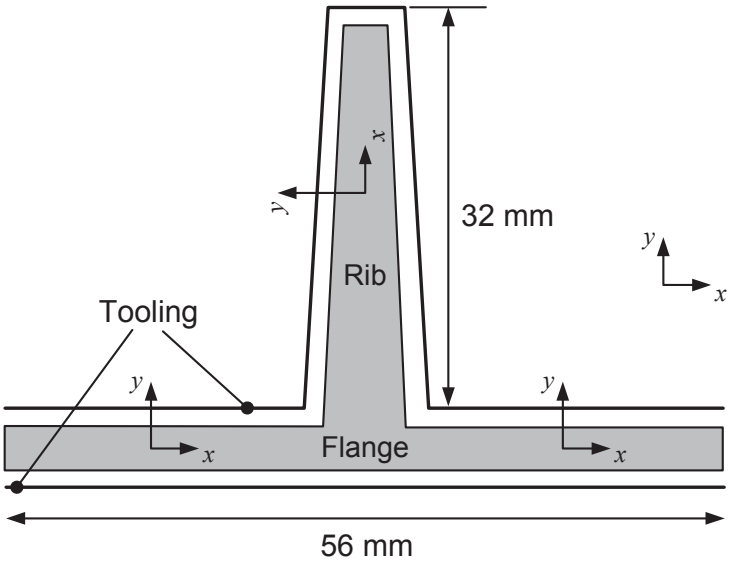

Figure 7.12 – Two-dimensional model of the rib and flange sections of the L-bracket. The coordinate systems on the part show the local fibre orientation, where x and y are the in-plane and out-of-plane orientations, respectively.

Table 7.4 – Elements employed in the 2–D rib compaction model.

Component	Elements	Degrees of freedom
Composite	PLANE223 (8 nodes)	UX, UY, TEMP
Tooling	CONTA172 (3 nodes) TARGE169 (3 nodes)	UY

Two cases were studied. First, the flange was cooled before the rib, with a 30 °C difference between the two components. The rib temperature for case 1 was:

$$T_{\text{rib}}^{\text{Case 1}} = T_{\text{flange}} + 30\,^{\circ}\text{C} \tag{7.7}$$

In the second case, the rib was cooled before the flange, with the same temperature difference between the two components. Therefore, for case 2:

$$T_{\text{rib}}^{\text{Case 2}} = T_{\text{flange}} - 30\,^{\circ}\text{C} \tag{7.8}$$

Four different moulding pressures were simulated for each case: 50 bar, 100 bar, 150 bar and 200 bar. For each case, the average rib pressure was measured as a function of the rib temperature during cooling. The rib pressure was measured on its surface, on a 20 mm long section located at its center. The results are presented in Fig. 7.13. In case 1, where the flange cooled before the rib (Fig. 7.13a), the average rib pressure is much lower than the moulding pressure. Overall, the influence of the moulding pressure was negligible and the pressure was lost at around 310 °C for the four cases. This behaviour is explained in the following. Since the flange was cooled first and the difference was 30 °C, the latter was around 85% crystallized when the rib was at 320 °C. The out-of-plane modulus of the flange at that point was 1.5 GPa. The high modulus of the flange was thus preventing proper compaction of the rib. Since the modulus kept increasing as the part was cooled, the average rib pressure kept decreasing until it reached zero at 310 °C.

In case 2, where the rib was cooled before the flange (Fig. 7.13b), the average rib pressure at 320 °C was around 15-20% of the moulding pressure. At that point, the flange was at 350 °C, and its modulus was very close to zero, which allows proper compaction of the rib. The average rib pressure then started dropping at around 310 °C, which coincides with the start of crystallization at 10 °C/min. Increasing the pressure from 50 bar to 200 bar resulted in higher average rib pressures, and lower PLTs. The latter was reduced from 307 °C to 301 °C for range of moulding pressure simulated. This reduction is a significant improvement considering the narrow crystallization temperature range of PEEK.

The results from this parametric study showed the importance of cooling complex features before other components during moulding of DLF composite parts. When this is achieved, the moulding pressure can be increased if necessary to reduce and hopefully completely eliminate defect formation on complex features. The same result explains why the enhanced cooling strategy was more effective than the increase in moulding pressure at reducing defect formation on an L-bracket rib feature (Section 6.1). The results obtained in both parametric studies are summarized in the design flowchart shown in Fig. 7.14, where the processing variables are evaluated in order to improve DLF composite part quality.

7.7 Summary

A finite element model capable of predicting pressure distribution during cooling of DLF composites was presented. The proposed model has the capability of identifying regions where localized compaction pressure is lost during processing. An analytical model was developed in order to evaluate the transverse modulus and thermal shrinkage of carbon/PEEK DLF composites as a function of degree of crystallinity, temperature, and cooling rate. The temperature distribution of the composite panel during cooling was measured experimentally and imported in the model. The latter was solve using ANSYS® Mechanical APDL. Validation was carried out by comparing the predicted defect areas against those found on DLF composite flat panels moulded at pressures ranging from 10 bar to 110 bar. A good agreement was found between the experimental and numerically predicted defect regions. Two case studies were presented. The first one showed the importance of reducing part temperature variation during cooling of relatively flat components. The second case study demonstrated the

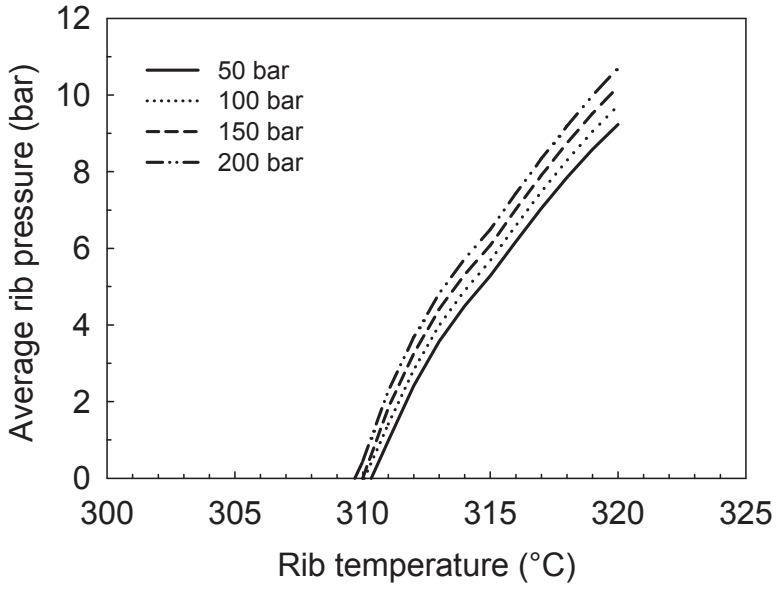

(a)

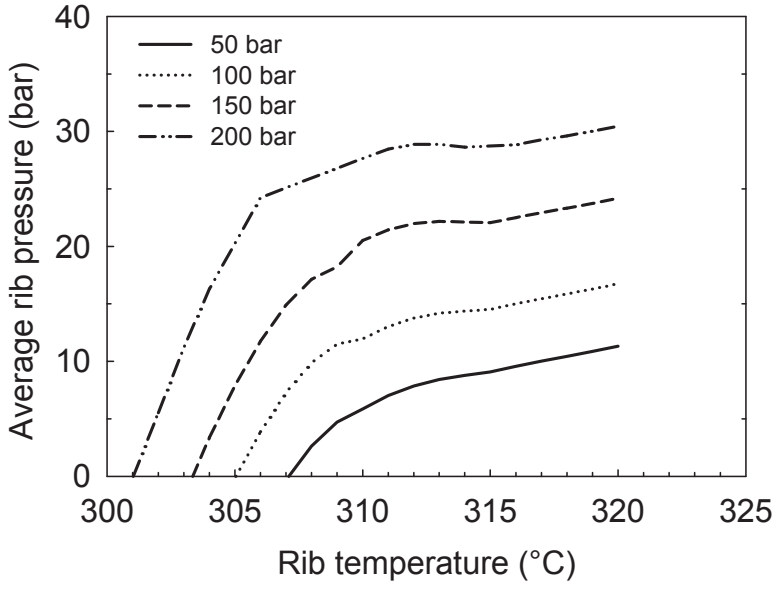

(b)

Figure 7.13 – Average rib pressure vs. rib temperature during cooling. (a) Case 1: flange cooled before the rib. (b) Case 2: rib cooled before the flange. The temperature difference between the rib and the flange was 30 °C for both cases.

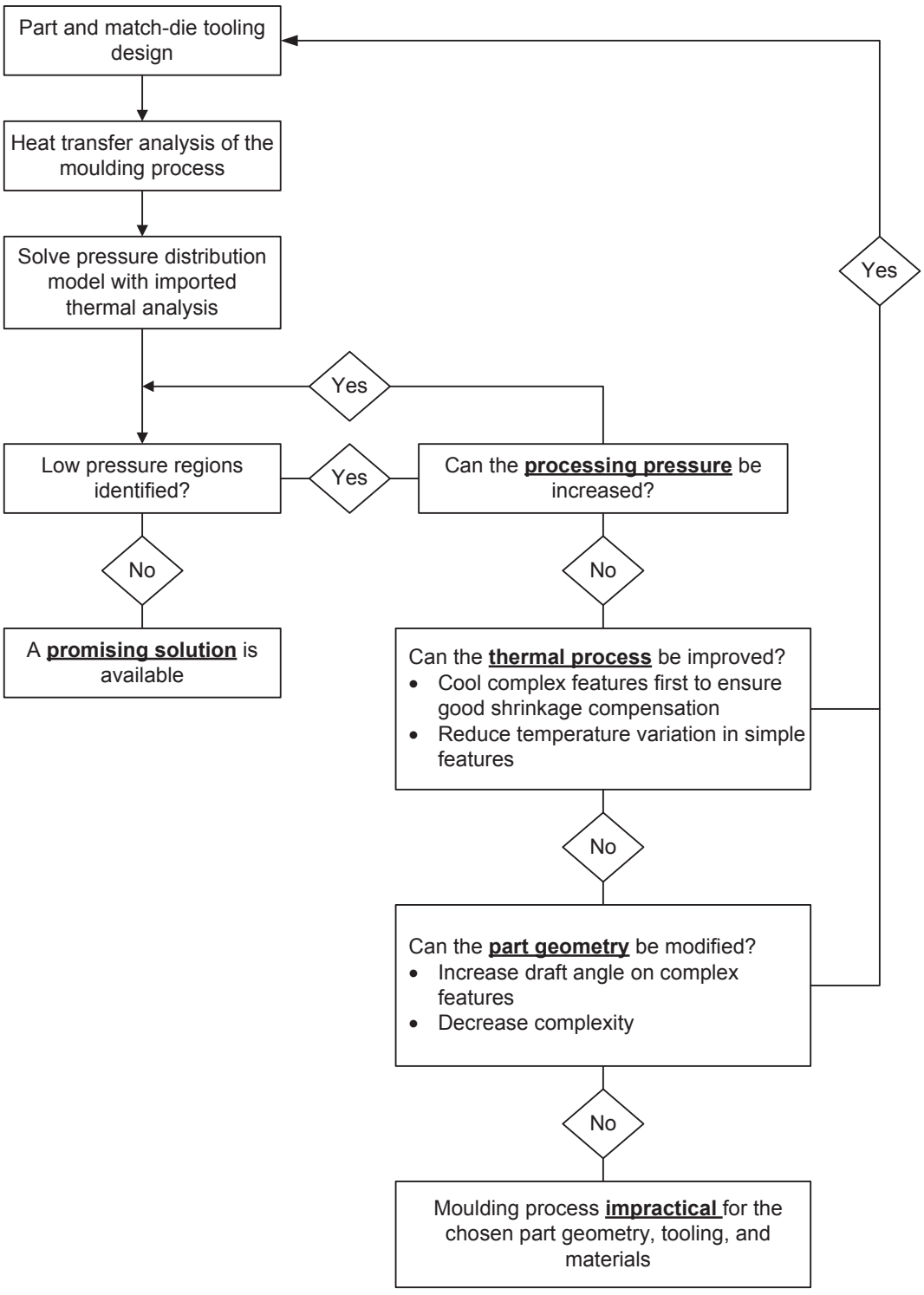

Figure 7.14 – Flowchart to evaluate processing variables to improve DLF composite part quality.

need for complex components such as a rib feature to be cooled before the rest of the part to ensure proper load transfer during crystallization of the latter.

In summary, the model developed in this chapter can be used to predict defect formation in complex-shaped DLF composite parts. If such model would be employed during the tooling design step, problematic areas could be identified. Adjustments could then be made to the part, tooling, and/or cooling strategy, which would greatly reduce the risk of defect formation during moulding.

Chapter 8

Conclusions, Contributions, and Future Outlook

Composite materials are increasingly used in lightweight and high-performance aerospace applications, and the search for fast, low-cost composite alternatives to complex-shaped metallic components is underway. Compression moulding of discontinuous long fibre (DLF) composites is a promising solution, although the manufacturing presents some unique challenges. The main objective of this work was to study defect formation during compression moulding of DLF composites. To achieve this objective, material characterization was coupled with focused experiments and processing modelling. The following conclusions and contributions can be drawn from this work:

1. **The rapid changes in the thermomechanical properties of carbon/PEEK composites due to crystallization can create localized loss of pressure.**

   Moulding pressure can be lost during cooling of thermoplastic DLF composites, through a combination of temperature variation, rapid out-of-plane shrinkage and fast modulus development during crystallization.

   Original contributions: 1) A technique was developed to measure thermal and crystallization shrinkage, as well as modulus development of car-

bon/PEEK composites during crystallization from the melt temperature. 2) An analytical model was proposed to evaluate the thermomechanical properties at high cooling rates.

2. **Defects can form during cooling of thermoplastic DLF composites when the moulding pressure is lost during crystallization.**

   An instrumented hot press was successfully employed to characterize defect formation. Optical microscopy and micro-CT approaches were employed to identity the types of defects caused by the loss of pressure during cooling. The results were used to validate a pressure distribution model.

   Original contributions: 1) A technique was developed to reproduce the moulding defects, from which the critical temperature range of defect formation was identified. 2) Loss of contact between the material and the mould platen was demonstrated via a custom dynamic mechanical analysis test. 3) The effect on mechanical properties was measured by considering the surface void content and internal void content separately.

3. **Proper cooling strategy is required to mould defect-free DLF composite parts.**

   The importance of cooling complex features before other components during moulding of DLF composite parts was demonstrated using experiments and process modelling. When this is achieved, the moulding pressure can be increased if necessary to reduce and hopefully completely eliminate defect formation on complex features.

   Original contribution: A process model was developed to measure the part pressure distribution during DLF composite fabrication. The model was used to study the effect of process parameters and offer guidelines to mitigate process-induced defects.

8.1 Future outlook

Additional aspects of DLF composite processing that could be studied in follow-on projects include:

1. **Generate a more accurate compaction curve.**

   The high fibre volume fraction of high-performance composites greatly reduces its maximum compaction strain. A technique could be developed to measure the non-linear compaction of the material during cooling from melt.

2. **Study the effect of fibre discontinuity and out-of-plane orientation on thermomechanical properties.**

   The thermomechanical properties in this work were characterized on continuous fibre composites, thus neglecting the influence of fibre discontinuity and out-of-plane fibre orientations on thermal shrinkage and modulus development.

3. **Embed pressure sensors to capture non-uniform compaction pressure.**

   A technique could be developed to monitored pressure distribution with the help of pressure sensors embedded in the tooling. They could be employed to further validate the experimental and modelling work presented in this thesis.

4. **Evaluate the effect of process-induced defect on fatigue properties.**

   The high sensitivity of the mechanical properties to porosity demonstrates the need to quantify their effect on fatigue properties. Temperature cycling could also be considered.

5. **Develop a complete process model that would include the prediction of residual stresses.**

   The pressure distribution model could be adapted to take into account residual stresses development due to non-uniform cooling. This would help minimize dimensional instabilities, leading to better geometric precision and better repeatability among moulded parts.

References

[1] The Boeing Company. Boeing 787 from the Ground Up. In: Aeromagazine, QTR 4, 2006.

[2] Campbell FC. Structural Composite Materials. ASM International, 2010.

[3] Greene TL. Discontinuous long fiber composites for complex shape metal replacement. In: CAMX – The Composites and Advanced Materials Expo, Orlando, FL, USA, 2014.

[4] Halpin JC. Stiffness and expansion estimates for oriented short fiber composites. Journal of Composite Materials 1969;3:732–734.

[5] Halpin JC. The laminate approx. for randomly oriented short fiber composites. Journal of Composite Materials 1969;3:720–724.

[6] Feraboli P, Peitso E, Deleo F, Cleveland T, Stickler PB. Characterization of prepreg-based discontinuous carbon fiber/epoxy systems. Journal of Reinforced Plastics and Composites 2009;28(10):1191–1214.

[7] Howell D, Fukumoto S. Compression molding of long chopped fiber thermoplastic composites. In: CAMX – The Composites and Advanced Materials Expo, Orlando, FL, USA, 2014.

[8] Feraboli P, Gasco F, Wade B, Maier S, Kwan R, Salmon W, Masini A, DeOto L, Reggiani M. Lamborghini "Forged Composite®" technology for the suspension arms of the Sesto Elemento. In: 2nd Joint US-Canada Conference on Composites – American Society for Composites, 26th Annual Technical Conference: Canadian Association for Composite Structures and Materials, Montreal, QC, Canada, 2011.

[9] LeBlanc D, Landry B, Levy A, Hubert P, Roy S, Yousefpour A. Compression moulding of complex parts using randomly-oriented strands thermoplastic composites. In: International SAMPE Symposium and Exhibition, Seattle, WA, USA, 2014.

[10] Eguémann N, Giger L, Roux M, Dransfeld C, Thiébaud F, Perreux D. Compression moulding of complex parts for the aerospace with discontinuous novel and recycled thermoplastic composite materials. In: 19th International Conference on Composite Materials, Montreal, QC, Canada, 2013.

[11] LeBlanc D. Compression moulding of complex parts with randomly-oriented strand thermoplastic composites. Master's Thesis: McGill University, 2014.

[12] da Costa AP, Botelho EC, Costa ML, Narita NE, Tarpani JR. A review of welding technologies for thermoplastic composites in aerospace applications. Journal of Aerospace Technology and Management 2012;4(3):255–265.

[13] Gardiner G. Overmolding expands PEEK's range in composites. Journal of Aerospace Technology and Management 2015;1(7):19–21.

[14] Schinner G, Brandt J, Richter H. Recycling carbon-fiber-reinforced thermoplastic composites. Journal of Thermoplastic Composite Materials 1996; 9(3):239–245.

[15] Vaidya UK, Chawla KK. Processing of fibre reinforced thermoplastic composites. International Materials Reviews 2008;53(4):185–218.

[16] Quantum Composites Inc, AMC® 8593, Engineered Structural Composite® (ESC®) Molding Compound, Technical Datasheet, 2013.

[17] Chang IY, Pratte JF. LDF thermoplastic composite technology. Journal of Thermoplastic Composite Materials 1991;4(3):227–252.

[18] Sun CT, Chung I, Chang IY. Modeling of elastic-plastic behavior of LDFTM and continuous fiber reinforced AS-4/PEKK composites. Composites Science and Technology 1992;43(4):339–345.

[19] Schuster J, Friedrich K. Fatigue testing of thermoformed bidirectional LDFTM-composites. Applied Composite Materials 1994;1(1):55–68.

[20] Schuster J, Friedrich K. Modeling of the mechanical properties of discontinuous-aligned-fiber composites after thermoforming. Composites Science and Technology 1996;57(4):405–413.

[21] Harper LT, Turner TA, Warrior NA, Rudd C. Characterisation of random carbon fibre composites from a directed fibre preforming process: The effect of fibre length. Composites Part A: Applied Science and Manufacturing 2006;37(11):1863–1878.

[22] Harper LT, Turner TA, Warrior NA, Dahl JS, Rudd C. Characterisation of random carbon fibre composites from a directed fibre preforming process: Analysis of microstructural parameters. Composites Part A: Applied Science and Manufacturing 2006;37(11):2136–2147.

[23] Johanson K, Harper LT, Johnson MS, Warrior NA. Heterogeneity of discontinuous carbon fibre composites: Damage initiation captured by Digital Image Correlation. Composites Part A: Applied Science and Manufacturing 2015;68:304–312.

[24] Taketa I, Okabe T, Kitano A. A new compression-molding approach using unidirectionally arrayed chopped strands. Composites Part A: Applied Science and Manufacturing 2008;39(12):1884–90.

[25] Taketa I, Okabe T, Kitano A. Strength improvement in unidirectional arrayed chopped strands with interlaminar toughening. Composites Part A: Applied Science and Manufacturing 2009;40(8):1174–1178.

[26] Taketa I, Satoa N, Kitanoa A, Nishikawab M, Okabec T. Enhancement of strength and uniformity in unidirectionally arrayed chopped strands with angled slits. Composites Part A: Applied Science and Manufacturing 2010; 41(11):1639–1646.

[27] Taketa I, Okabe T, Matsutani H, Kitano A. Flowability of unidirectionally arrayed chopped strands in compression molding. Composites Part B: Engineering 2011;42(6):1764–9.

[28] Feraboli P, Peitso E, Cleveland T, Stickler PB, Halpin JC. Notched behavior of prepreg-based discontinuous carbon fiber/epoxy systems. Composites Part A: Applied Science and Manufacturing 2009;40(3):289–299.

[29] Feraboli P, Peitso E, Cleveland T, Stickler PB. Modulus measurement for prepreg-based discontinuous carbon fiber/epoxy systems. Journal of Composite Materials 2009;43(19):1947–65.

[30] Feraboli P, Cleveland T, Ciccu M, Stickler P, DeOto L. Defect and damage analysis of advanced discontinuous carbon/epoxy composite materials. Composites Part A: Applied Science and Manufacturing 2010;41(7):888–901.

[31] Feraboli P, Cleveland T, Stickler P, Halpin J. Stochastic laminate analogy for simulating the variability in modulus of discontinuous composite materials. Composites Part A: Applied Science and Manufacturing 2010; 41(4):557–570.

[32] Boeing 787 features composite window frames. Reinforced plastics, Application News 2007;51(3):4–58.

[33] Tuttle M, Shifman T, Boursier B. Simplifying certification of discontinuous composite material forms for primary aircraft structures. In: International SAMPE Symposium and Exhibition, Seattle, WA, USA, 2010.

[34] van Wijngaarden M, Jongbloed A, de Vries J. Thermoplastic compound compression molding. In: International SAMPE Symposium and Exhibition, Seattle, WA, USA, 2010.

[35] Picher-Martel GP, Levy A, Hubert P. Compression molding of carbon/polyether ether ketone composites: Squeeze flow behavior of unidirectional and randomly oriented strands. Polymer Composites 2015;Article in Press.

[36] Picher-Martel GP. Compression moulding of randomly-oriented strand thermoplastic composites: A study of the flow and deformation mechanisms. PhD Thesis: McGill University, 2015.

[37] Han JH, Alexander WB, Torres F, Mushinski L, Greene T. Effect of fabric reinforcement on failure response of discontinuous long fiber composite bolted joints. In: International SAMPE Technical Conference, Long Beach, CA, USA, 2011.

[38] TenCate Advanced Composites USA, TenCate Cetex® MC1200 PEEK Thermoplastic BMC, Technical Datasheet, 2012.

[39] Johanson K, Harper LT, Johnson M, Kennedy A, Warrior NA. Studying the heterogeneity of discontinuous fiber composites using a new full-field strain measurement system. In: 19th International Conference on Composite Materials, Montreal, QC, Canada, 2013.

[40] Department of Defence, United States of America. Composite materials handbook MIL-HDBK-17, Vol. 3 – Polymer matrix composites materials usage, design and analysis. 2002.

[41] Boursier B, Lopez A. Failure initiation and effect of defects in structural discontinuous fiber composites. In: 42nd International SAMPE Technical Conference, Salt Lake City, UT, 2010.

[42] Eguémann N, Giger L, Masania K, Dransfeld C, Thiebaud F, Perreux D. Processing of characterization of carbon fibre reinforced PEEK with discontinuous architecture. In: 16th European Conference on Composite Materials, Seville, Spain, 2014.

[43] Han JH, Mushinski L, Patel P, Godwin AW. Discontinuous long fiber vs. continuous fiber reinforced composites in impact resistance and residual strength after impact. In: CAMX – The Composites and Advanced Materials Expo, Orlando, FL, USA, 2014.

[44] Selezneva M. Experimental and theoretical investigations of mechanical properties of Randomly-Oriented Strand (ROS) composites. PhD Thesis: McGill University, 2015.

[45] Selezneva M, Picher-Martel GP, Landry B, Trudel-Boucher D, Roy S, Khoun L, Hojjati M, Lessard L, Hubert P. Discontinuous-fibre carbon/PEEK Composites: Study of Mechanical Properties. In: International SAMPE Symposium and Exhibition, Baltimore, MD, 2012.

[46] Selezneva M, Kouwonou K, Lessard L, Hubert P. Mechanical properties of randomly oriented strands thermoplastic composites. In: 19th International Conference on Composite Materials, Montreal, QC, Canada, 2013.

[47] Roux M, Dransfeld C, Eguémann N, Giger L. Recycling of high performance thermoplastic composites with high voltage fragmentation. In: 19th International Conference on Composite Materials, Montreal, QC, Canada, 2013.

[48] Roux M, Eguémann N, Dransfeld C, Thiébaud F, Perreux D. Thermoplastic carbon fibre-reinforced polymer recycling with electrodynamical fragmentation: From cradle to cradle. Journal of Thermoplastic Composite Materials 2015;1(23):1–23.

[49] Eguémann N, Giger L, Dransfeld C, Thiébaud F, Perreux D. Manufacturing and recycling of complex composite thermoplastic parts for aerospace applications. In: SAMPE Europe 7th SETEC 12 International Technical Conference, Lucerne, Switzerland, 2012.

[50] Leblanc D, Landry B, Jancik M, Hubert P. Recyclability of randomly-oriented strand thermoplastic composites. In: 20th International Conference on Composite Materials, Copenhagen, Denmark, 2015.

[51] Ghiorse S. Effect of void content on the mechanical properties of carbon/epoxy laminate. SAMPE Quarterly 1993;24(2):54–59.

[52] Hancox NL. The compression strength of unidirectional carbon fibre reinforced plastic. Journal of Materials Science 1975;10:234–242.

[53] Bowles KJ, Frimpong S. Void Effects on the Interlaminar Shear Strength of Unidirectional Graphite-Fiber-Reinforced Composites. Journal of Composite Materials 1992;26(10):1487–1509.

[54] Olivier P, Cottu JP, Ferret B. Effects of cure cycle pressure and voids on some mechanical properties of carbon/epoxy laminates. Composites 1995; 26(7):509–515.

[55] Costa ML, de Almeida SFM, Rezende MC. The influence of porosity on the interlaminar shear strength of carbon/epoxy and carbon/bismaleimide fabric laminates. Composites Science and Technology 2001;61(14):2101–2108.

[56] Harper BD, Staab GH, Chen RS. A Note on the Effects of Voids Upon the Hygral and Mechanical Properties of AS4/3502 Graphite/Epoxy. Journal of Composite Materials 1987;21(3):280–289.

[57] Hagstrand P, Bonjour F, Månson JAE. The influence of void content on the structural flexural performance of unidirectional glass fibre reinforced polypropylene composites. Composites Part A: Applied Science and Manufacturing 2005;36(5):705–714.

[58] Barnes JA, Byerly GE. The formation of residual stresses in laminated thermoplastic composites. Composites Science and Technology 1994;51(4):479–94.

[59] Lu SX, Cebe P, Capel M. Thermal stability and thermal expansion studies of PEEK and related polyimides. Polymer 1996;37(14):2999–3009.

[60] Unger WJ, Hansen JS. Effect of thermal processing on residual strain development in unidirectional graphite fibre reinforced PEEK. Journal of Composite Materials 1993;27(1):59–82.

[61] Jeronimidis G, Parkyn AT. Residual stresses in carbon fibre-thermoplastic matrix laminates. Journal of Composite Materials 1988;22(5):401–15.

[62] Lawrence WE, Seferis JC, Gillespie JW. Material response of a semicrystalline thermoplastic polymer and composite in relation to process cooling history. Polymer Composites 1992;13(2):86–96.

[63] Unger WJ, Hansen JS. The effect of cooling rate and annealing on residual stress development in graphite fibre reinforced peek laminates. Journal of Composite Materials 1993;27(2):108–137.

[64] Parlevliet PP, Bersee HEN, Beukers A. Residual stresses in thermoplastic composites-A study of the literature-Part II: Experimental techniques. Composites Part A: Applied Science and Manufacturing 2007;38(3):651–665.

[65] Chapman TJ, Gillespie JW, Pipes RB, Manson JAE, Seferis JC. Prediction of process-induced residual stresses in thermoplastic composites. Journal of Composite Materials 1990;24(6):616–643.

[66] Zoller P. Solidification processes in thermoplastics and their role in the development of internal stresses in composites. In: American Society for Composites – Third technical conference, Seattle, WA, USA, 1988.

[67] Bas C, Grillet AC, Thimon F, Albérola ND. Crystallization kinetics of poly(aryl ether ether ketone): Time-temperature-transformation and continuous-cooling-transformation diagrams. European Polymer Journal 1995;31(10):911–921.

[68] Velisaris CN, Seferis JC. Crystallization Kinetics of Polyetheretherketone (PEEK) Matrices. Polymer Engineering and Science 1986;26(22):1574–1581.

[69] Xiao XR, Hoa SV. Effect of melting history on the crystalline characteristics of poly(etheretherketone) aromatic polymer composite. Theoretical and Applied Fracture Mechanics 1990;14(1):49–56.

[70] Davies P, Cantwell WJ, Jar PY, Richard H, Neville DJ, Kausch HH. Cooling rate effects in carbon fibre/PEEK composites. In: O'Brien TK, editor, Composite Materials: Fatigue and Fracture, ASTM STP 1110. American Society for Testing and Materials; 1991. p. 70–88.

[71] Khoun L, Penet C, Demaria C, Trudel-Boucher D, Hubert P. Effect of autoclave process parameters on quality and performances of PEEK/carbon composite panels. In: 2nd Joint US-Canada Conference on Composites – American Society for Composites, 26th Annual Technical Conference: Canadian Association for Composite Structures and Materials, Montreal, QC, Canada, 2011.

[72] Taylor RE. Thermal Expansion of Solids. ASM International, 1998.

[73] Kratz J. Transport phenomena in vacuum bag only prepreg processing of honeycomb sandwich panels. PhD Thesis: McGill University, 2013.

[74] ASTM D3039-00. Standard Test Method for Tensile Properties of Polymer Matrix Composite Materials. Annual Book of ASTM Standards, Volume 15.03, 2000.

[75] ASTM D6484-03. Standard Test Method for Compressive Properties of Polymer Matrix Composite Materials with Unsupported Gage Section by Shear Loading. Annual Book of ASTM Standards, Volume 15.03, 2009.

[76] ASTM D2344-06. Standard test method for short-beam strength of polymer matrix composite materials and their laminates. Annual Book of ASTM Standards, Volume 15.03, 2006.

[77] ASTM D5528-01. Standard test method for mode I interlaminar fracture toughness of unidirectional fiber-reinforced polymer matrix composites. Annual Book of ASTM Standards, Volume 15.03, 2001.

[78] Davies P, Cantwell W, Moulin C, Kausch HH. Study of the delamination resistance of IM6/PEEK composites. Composites Science and Technology 1989;36(2):153–166.

[79] Vautey P. Cooling rate effects on the mechanical properties of a semi-crystalline thermoplastic composite. SAMPE Quarterly 1990;21(2):23–28.

[80] Lustiger A, Uralil F, Newaz G. Processing and structural optimization of PEEK composites. Polymer Composites 1990;11(1):65–75.

[81] Vu-Khanh T, Frikha S. Influence of processing on morphology, interface, and delamination in PEEK/carbon composites. Journal of Thermoplastic Composite Materials 1999;12(2):84–95.

[82] Gao SL, Kim JK. Cooling rate influences in carbon fibre/PEEK composites. Part II: Interlaminar fracture toughness. Composites Part A: Applied Science and Manufacturing 2001;32(6):763–774.

[83] Drzal LT. Fibre-matrix adhesion and its relationship to composite mechanical properties. Journal of Materials Science 1993;28(3):569–610.

[84] Lee WI, Springer GS. A Model of the Manufacturing Process of Thermoplastic Matrix Composites. Journal of Composite Materials 1987;21(11):1017–55.

[85] Levy A, Corre SL, Chevaugeon N, Poitou A. A level set based approach for the finite element simulation of a forming process involving multiphysics coupling: Ultrasonic welding of thermoplastic composites. European Journal of Mechanics - A/Solids 2011;30(4):501–509.

[86] Carslaw HS, Jaeger JC. Conduction of heat in solids. Oxford, UK: Clarendon Press, 1959.

[87] ASTM D7264-07. Standard Test Method for Flexural Properties of Polymer Matrix Composite Materials. Annual Book of ASTM Standards, Volume 15.03, 2007.

[88] Wisnom MR, Reynolds T, Gwilliam N. Reduction in interlaminar shear strength by discrete and distributed voids. Composites Science and Technology 1996;56(1):93–101.

[89] ASTM D7136-07. Standard test method for measuring the damage resistance of a fiber-reinforced polymer matrix composite to a dynamic impact event. Annual Book of ASTM Standards, Volume 15.03, 2007.

[90] Gao SL, Kim JK. Cooling rate influences in carbon fibre/PEEK composites. Part III: Impact damage performance. Composites Part A: Applied Science and Manufacturing 2001;32(6):775–785.

[91] Ogale AA, McCullough RL. Influence of microstructure on elastic and viscoelastic properties of polyether ether ketone. Composites Science and Technology 1987;30(3):185–201.

[92] Hubert P, Poursartip A. A method for the direct measurement of the fibre bed compaction curve of composite prepregs. Composites Part A: Applied Science and Manufacturing 2001;32(2):179–187.